DYNAMIC SCALE MODELING OF BED CONFIGURATIONS

by

LAWRENCE ALLEN BOGUCHWAL

B.A., Harvard College
(1972)

SUBMITTED IN PARTIAL FULFILLMENT
OF THE REQUIREMENTS FOR THE
DEGREE OF

DOCTOR OF PHILOSOPHY

at the

MASSACHUSETTS INSTITUTE OF TECHNOLOGY

OCTOBER, 1977

Lie. February 1978

Signature of Author .....
Department of Earth and Planetary Sciences, October 14, 1977

Certified by .....
Thesis Supervisor

Accepted by .....
Chairman, Department Committee

WITHDRAWN
DEC 1977
FROM
MIT LIBRARIES

DYNAMIC SCALE MODELING OF BED CONFIGURATIONS

by Lawrence Allen Boguchwal

Submitted to the Department of Earth and Planetary Sciences on October 14, 1977 in partial fulfillment of the requirements for the Degree of Doctor of Philosophy.

ABSTRACT

A test was conducted proving that dynamic scale modeling of bed configurations is possible and that the following set of seven independent variables must fully characterize bed configurations: gravitational acceleration g, mean flow velocity U, mean flow depth d, fluid density ρ, fluid viscosity μ, sediment density ρ_s, and median sediment size D. For the test, conditions for two flume runs, one a hot-water model, the other a cold-water prototype, were adjusted according to a scale ratio of 1.66. Coincidence of cumulative frequency curves for the prototype and scaled-up model for each dependent variable, ripple height, ripple spacing and ripple migration time showed that the two runs were dynamically similar. Equations specifying dynamic similitude are $l_r = (\mu/\rho)^{2/3}$ and $(\rho_s/\rho)_r = 1$, where l_r is the length scale and subscript r represents a ratio between prototype and model.

Verification that the above set of seven variables fully characterizes bed configurations validates a three-dimensional diagram proposed by Southard (1971) based on a dimensional analysis of these variables in which mean flow depth, mean flow velocity, and median sediment size are correlated one-to-one with bed phase for constant water temperature and quartz-density sand. Existing flume data measured at different water temperatures were compared in this diagram by identifying the bed form hierarchy observed and by using the dynamic similitude equations to derive the dynamic equivalent for every flume run to one made at a standard temperature of 10°C. Boundaries separating bed phases were fully delineated in five velocity-size diagrams for 8.5 to 50 cm flow depth, eight depth-velocity diagrams for 0.13 to 1.60 mm sand size, and one depth-size diagram for 60 cm/sec flow velocity, by interpolation in three dimensions between orthogonal and parallel projections of the diagram.

Some of the most interesting relations among bed-phase stability fields were pinch-outs of fields, observed in the following projections: in velocity-size diagrams, the ripple field with increasing sediment size and bar, dune, and lower flat bed fields with decreasing sediment size; in depth-velocity diagrams for medium to coarse sediment sizes, the lower flat-bed field with increasing depth and the ripple and upper flat-bed fields with decreasing depth; in depth-size diagram, the bar, dune, and upper flat-bed fields with increasing depth, giving way to ripples or no movement at great depths.

Based on the depth-velocity-size diagram, the effect of a change in temperature on the observed configuration can be determined. Given the initial conditions and the temperature change, the standard temperature equivalent to each end state is located in the depth-velocity-size diagram and the bed phase and contour each plots on are identified. Contour values are then scaled to their equivalents at the observed temperatures.

A pilot study was carried out to determine the practicality of dynamic scale modeling using hot water with a flume and scale ratio larger than were used for the modeling test. Using hot-water modeling for scale ratios up to about 2.5 on a very large flume, natural depths can be simulated. Using hot-water modeling on a small flume, a larger flume can be simulated, representing many cost-effective savings and making existing flumes more flexible tools for research. While a procedure for hot-water modeling with a covered, insulated flume was being developed, experiments were made in which certain of the relations observed in the depth-velocity-size diagram were confirmed.

For sand sizes between about 0.1 mm and 0.3 mm, the sequence of bed states with increasing flow velocity is: ripples, continuous-crested bars comparable to ripples in height but with significantly greater spacings comparable to dunes, discontinuous-crested bars with somewhat deeper troughs, continuous-crested dunes whose spacings and trough lengths steadily increase with velocity while heights increase but then decrease, and upper flat bed. With decreasing sand size the interval of velocity over which bars and dunes are stable steadily decreases and disappears at about 0.13 mm for 50 cm flow depth. Near the "point" of pinch-out distinction of bed forms is somewhat blurred as bed forms appear to possess attributes of adjacent stability fields. In addition to these results, data for bed-form height from this and other studies were summarized in qualitatively contoured depth-velocity and velocity-size diagrams.

These results confirm the extension of the bar stability field into fine sand sizes, the pinch-out of bar and dune stability fields with decreasing sand size, the subdivision of the bar field according to bed-form hierarchy, and the subdivision of the dune field into dunes and flattened dunes. A plot of data onto the velocity-size plane agreed with boundaries of a velocity-size diagram (for 50 cm flow depth) constructed by three-dimensional interpolation of boundaries in the depth-velocity-size diagram. Thus, placement of boundaries in the depth-velocity-size diagram must be generally correct. Given the practicality of hot-water modeling and the consolidation of existing flume data, a velocity-size diagram for 2.5 m flow depth was constructed as a rough guide for the next generation of deep-water flume experiments.

Advisor: Dr. John B. Southard, Associate Professor of Geology

To my parents,
who taught me perspective.

TABLE OF CONTENTS

	Page No.
TITLE PAGE	1
ABSTRACT	2
DEDICATION	4
TABLE OF CONTENTS	5
LIST OF SYMBOLS	8
LIST OF FIGURES	9
LIST OF TABLES	12
ACKNOWLEDGMENTS	13
PART I: SCALE MODELING OF BED CONFIGURATIONS	14
INTRODUCTION	14
Motivation for this study.	14
Overview of dissertation.	15
PRINCIPLES OF SCALE MODELING	16
Dynamic similitude.	16
The fundamental set of variables.	20
Determination of dynamic similitude for bed configurations.	23
Laboratory implementation of scale modeling.	26
PART II: TEST OF DYNAMIC SCALE MODELING	29
CRITERIA FOR TEST	29
PROCEDURE	30
Apparatus and determination of independent variables.	30
Measurement of dependent variables.	35
General operating procedure.	37

	Page No.
RESULTS AND DISCUSSION	38
PART III: SYNTHESIS OF EXISTING DATA	49
INTRODUCTION	49
Correlation of fundamental variables with bed phases.	49
Depth-velocity-size diagram.	52
Objectives.	54
CONSTRUCTION OF DIAGRAM	56
Temperature normalization of data.	56
Plotting the data.	58
Three-dimensional interpolation of boundaries.	62
DISCUSSION	79
Relations of bed-phase stability fields.	79
Temperature effects.	85
PART IV: PILOT STUDY OF HOT-WATER MODELING	91
OBJECTIVES	91
PROCEDURE	93
Flume.	93
Temperature control.	97
Measurement and error of depth and velocity.	100
Selection of sand.	101
General operating procedure.	102
RESULTS	105
Presentation and description of data.	105
Contouring the depth-velocity-size diagram.	121
DISCUSSION	126

	Page No.
PART V: SUMMARY OF CONCLUSIONS	132
BIBLIOGRAPHY	138
APPENDIX	143
BIOGRAPHY	149

LIST OF SYMBOLS AND THEIR DIMENSIONS

m	Dimension of mass or number of fundamental dimensions
l	Dimension of length
t	Dimension of time
A	Average, equilibrium height of bed forms (l); Area (l^2)
b	Width of flow (l)
D	Median grain diameter (l)
d	Mean flow depth (l)
F	Froude number = $U/(gd)^{1/2}$ (*1*)
g	Gravitational acceleration (l/t^2)
l_r	Length scale ratio, prototype to model (relative to one)
n	Number of independent variables in the fundamental set
Q	Flow discharge (l^3/t)
q	Flow discharge per unit width (l^2/t)
R	Depth Reynolds number = Ud/ν (*1*)
S	Regional slope (*1*)
T	Temperature, °Celsius
t_m	Mean, equilibrium ripple migration time (t)
U	Mean flow velocity (l/t)
λ	Mean, equilibrium spacing of bed forms (l)
μ	Dynamic viscosity (m/lt)
ν	Kinematic viscosity (l^2/t)
ρ	Fluid density (m/l^3)
ρ_s	Sediment density (m/l^3)
σ	Sediment sorting (*1*)
τ_o	Mean bed shear stress (m/lt^2)
$\tau_o U$	Flow power (m/t^3)

LIST OF FIGURES

		Page No.
Fig. 1.1	Flow conditions for flume and field studies.	17
Fig. 1.2	Scale ratios at different water temperatures.	28
Fig. 2.1	Schematic diagram of 8 m flume.	32
Fig. 2.2	Photograph of 8 m flume.	33
Fig. 2.3	Photograph of typical ripple configuration, model.	39
Fig. 2.4	Cumulative frequency curves for ripple spacing.	42
Fig. 2.5	Cumulative frequency curves for ripple heights.	43
Fig. 2.6	Cumulative frequency curves for ripple migration times.	44
Fig. 3.1	Velocity-size diagram for 8.5 cm flow depth.	65
Fig. 3.2	Velocity-size diagram for 20 cm flow depth.	66
Fig. 3.3	Velocity-size diagram for 30 cm flow depth.	67
Fig. 3.4	Velocity-size diagram for 40 cm flow depth.	68
Fig. 3.5	Depth-velocity diagram for 0.13 mm sand size.	69
Fig. 3.6	Depth-velocity diagram for 0.22 mm sand size.	70
Fig. 3.7	Depth-velocity diagram for 0.31 mm sand size.	71
Fig. 3.8	Depth-velocity diagram for 0.55 mm sand size.	72
Fig. 3.9	Depth-velocity diagram for 0.62 mm sand size.	73

		Page No.
Fig. 3.10	Depth-velocity diagram for 1.07 mm sand size.	74
Fig. 3.11	Depth-velocity diagram for 1.60 mm sand size.	75
Fig. 3.12	Depth-velocity diagram for 0.90 mm sand size.	76
Fig. 3.13	Depth-size diagram for 60 cm/sec flow velocity.	77
Fig. 3.14	Legend for Figs. 3.1-3.12 and 4.5.	78
Fig. 4.1	Schematic diagram of 11.5 m flume.	94
Fig. 4.2	Photograph of 11.5 m flume.	95
Fig. 4.3	Cumulative frequency curves of sands.	103
Fig. 4.4	Velocity error bars for flume runs.	109
Fig. 4.5	Plot of data onto velocity-size diagram for 50 cm flow depth.	110
Fig. 4.6	Photograph of run IV-27. Linguoid ripples.	115
Fig. 4.7	Photograph of run IV-26. Bars plus ripples.	115
Fig. 4.8	Photograph of run IV-25. Bars plus ripples.	116
Fig. 4.9	Photograph of run IV-24. Bars plus ripples.	116
Fig. 4.10	Photograph of run IV-23. Bars plus dunes.	117
Fig. 4.11	Photograph of run IV-22. Bars plus dunes.	117
Fig. 4.12	Photograph of run IV-8. Dunes plus ripples.	118
Fig. 4.13	Photograph of run IV-7. Dunes plus ripples.	118
Fig. 4.14	Photograph of run IV-13. Dunes.	119

		Page No.
Fig. 4.15	Photograph of run IV-15. Dunes.	119
Fig. 4.16	Photograph of run IV-17. Flattened dunes.	120
Fig. 4.17	Photograph of run IV-19. Flattened dunes.	120
Fig. 4.18	Velocity-size diagram (50 cm flow depth) qualitatively contoured for bed-form height.	124
Fig. 4.19	Depth-velocity diagram (0.30 mm sand size) qualitatively contoured for bed-form height.	125
Fig. 4.20	Velocity-size diagram for 2.5 m flow depth.	131
Fig. A.1	Plot by source of data for Fig. 3.1.	144
Fig. A.2	Plot by source of data for Fig. 3.2.	145
Fig. A.3	Plot by source of data for Fig. 3.3.	146
Fig. A.4	Plot by source of data for Fig. 3.4.	147
Fig. A.5	Legend for Figs. A.1-A.4.	148

LIST OF TABLES

		Page No.
Table 2.1	Experimental conditions for flume runs of the modeling test.	41
Table 2.2	Mean and standard deviation of frequency distributions of experimental characteristics.	46
Table 3.1	Sources used for diagram and the range of normalized sediment sizes for each.	57
Table 3.2	Interval of control variable for each projection.	61
Table 4.1	Summary of observations from pilot study.	107
Table 4.2	Generalized contour patterns.	123

ACKNOWLEDGMENTS

It has been my privilege to work with Professor John B. Southard, without whose perceptive criticism and guidance in the scientific method this work would not have been possible. I wish to thank Professors Jon C. Boothroyd, Ole S. Madsen, David C. Roy, and Raymond Siever for their helpful comments on the final draft. I also wish to thank Professor Raymond Siever for the use of the 8 m flume at Harvard University.

For their cooperation and competence, I wish to acknowledge Sondra Hirsch, who typed this manuscript, Lohit Konwar, who drafted the figures, and Leroy Lindquist, who developed and mounted the photographs.

Those who offered a kind hand or bent ear when most needed are not forgotten. Among their number were fellow graduate students W. Russell Costello, William Corea, and Lohit Konwar, and my undergraduate assistants at various times.

Finally, to the person who shared my aspirations and frustrations, my wife Freda, I express my deepest appreciation for her concern and promethean patience.

PART I: SCALE MODELING OF BED CONFIGURATIONS

INTRODUCTION

Motivation for this study.

To better understand sediment transport one must rely heavily on empirical studies. Laboratory simulations of sediment transport are valuable because conditions can be controlled, thus permitting constancy of conditions, isolation of particular variables, and ease of observation--all largely unattainable in field studies of variable environments. Models have been constructed on the scale of: a whole environment (for example, the fluvial simulations of Friedkin, 1945; Schumm and Kahn, 1972), bed forms (such as the flume studies by Guy et al., 1966), sand grains (such as studies of forces on a grain by Chepil, 1961; Coleman, 1967). This study focuses on sediment transport on the scale of bed forms.

The usefulness of a model is limited by the extent to which it simulates its natural prototype. Observations of bed configurations in the field (for example, Boothroyd and Hubbard, 1975; Jackson, 1975) indicate that bed forms in natural environments are much larger, by factors of ten or more, than bed forms produced in laboratory settings. This disparity can be attributed to flow depth and width, the primary differences between conditions in the field and the flume. Nonerodible flume walls tend to restrict formation

of large, broad bed forms and impose unnatural shear forces on the configuration, apparent in relatively narrow channels with width-to-depth ratios less than about 5:1 (Williams, 1970). Furthermore, even with acceptable width-to-depth ratios, the flow depth in flume experiments is much less than depths observed in natural environments of greatest sedimentological interest (see Fig. 1.1). Although some studies (for example, Yalin, 1977) suggest a linear correlation between bed-form size and mean flow depth, there is no clear evidence that the effect of a depth change is a scale change from one configuration to another geometrically similar, as implied by these correlations. Nor is there evidence that these correlations can be applied across the gap between those depths in flumes and field environments, even if they are valid over the particular range of depths for which they were documented. Therefore, bed geometries and dynamics in flumes cannot be simply extrapolated to geometries and dynamics occurring in deeper natural settings; consequently, such simulations are only approximate.

Overview of dissertation.

To combine the strengths of the two approaches, the natural scale of field studies with the control of laboratory simulations, one would either have to build a very large model or devise a true, nondistorting method of scale modeling (or both).

Criteria for such modeling are developed in Part I and

tested in Part II of this work. In addition to successfully demonstrating dynamic scale modeling for bed configurations, results of the test verify that the variables upon which the model is based fully characterize bed configurations. Accordingly, in Part III a plot is constructed in which these variables are correlated with bed phases, making use of the previously developed scaling relationships so that data measured at different temperatures can be compared. In Part IV a pilot study is discussed, which was carried out to develop procedures for modeling at scale ratios larger than those in the test and to experimentally confirm interpretations of the above plot. The chief conclusions of this study are summarized and evaluated together in Part V.

PRINCIPLES OF SCALE MODELING

Dynamic similitude.

When all significant corresponding forces--and therefore all dependent effects of these forces--in two systems scale consistently according to a specific relationship, the two systems are said to be dynamically similar. Thus, the non-distorting simulation proposed in the Introduction is a model that is dynamically similar to its prototype.

An equivalent way of expressing dynamic similitude between two systems is that corresponding ratios of forces acting within each system are equal, where scale factors cancel out in each ratio. If an important force is left out

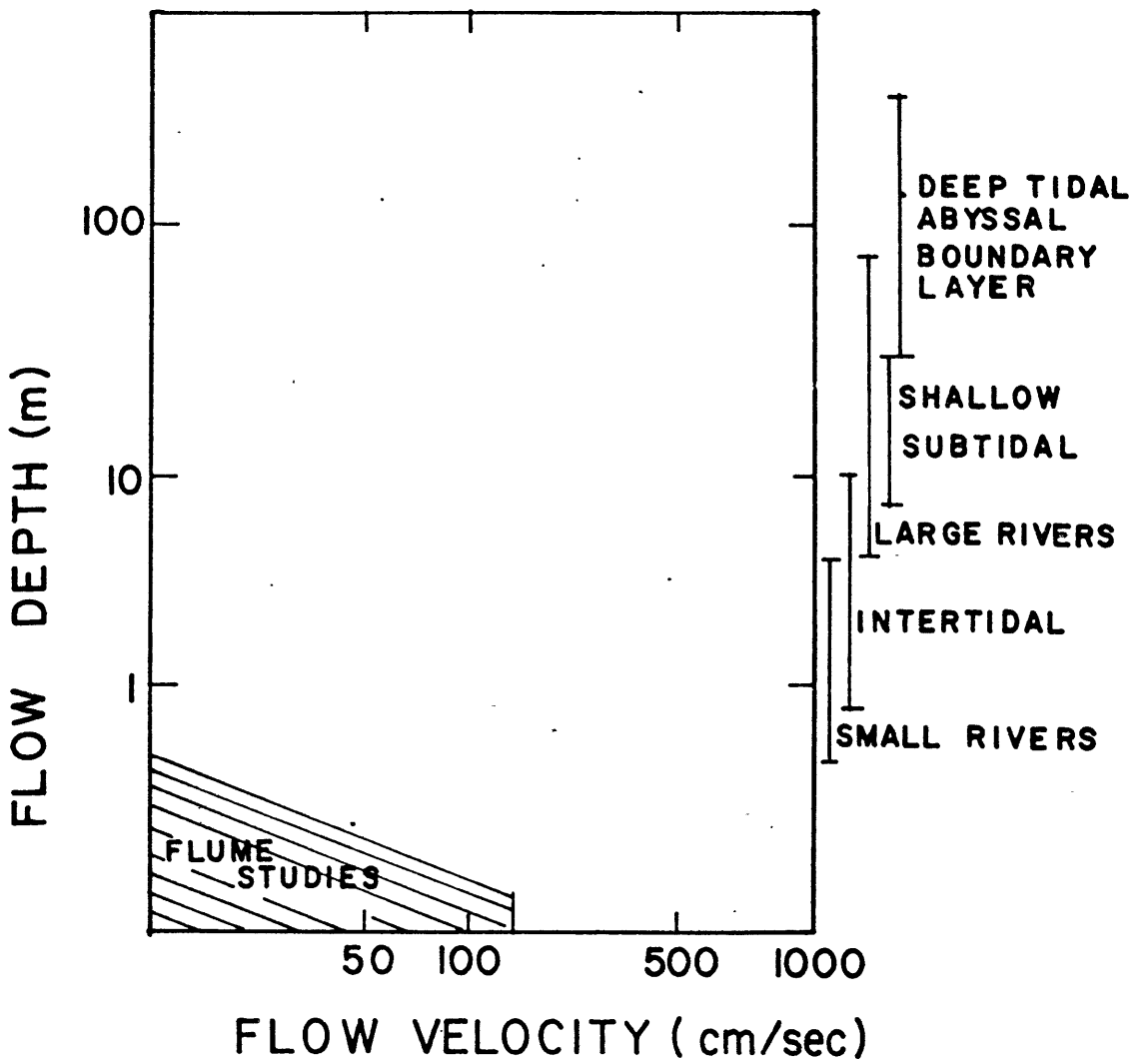

Fig. 1.1. Approximate flow conditions for flume studies, bottom left. At right, approximate depth ranges for natural flows (after Middleton and Southard, 1977, p. 7.38).

in the modeling procedure, effects related to that force do not scale appropriately in the model.

One way of assuring that all important forces are considered for a dynamic scale model is to work from the governing equations of a system. If two systems are dynamically similar to one another, their dimensionless governing equations will be identical since the scale ratios cancel out. For example, the governing equations that completely specify a one-component flow system are the Navier-Stokes equations. Dynamic scale modeling of one-component flow systems is achieved by the numerical equality between two systems of the following set of dimensionless parameters: a Mach number, a Reynolds number, and a Froude number (each is essentially a force ratio). For incompressible fluids like water, dynamic similitude is specified by Eq (1.1), derived by equating corresponding Reynolds and Froude numbers of two systems:

$$l_r = \nu_r^{2/3} \tag{1.1}$$

Few studies of free-surface systems based on Eq (1.1) have been made because of the demanding restrictions imposed on the model. Many studies have been made of dynamically similar systems possessing no free surface because there are less stringent restrictions on the model components as only Reynolds number similarity is required. Froude number similarity is an example of approximate, nondynamic modeling used for simulations of large-scale free-surface flows where viscous effects, characterized by the Reynolds number, are

relatively small. In Froude models there is large-scale geometric similarity, but distortions of the forces require such adjustments as railroad spikes on the bed of a fluvial model in order to simulate certain characteristics (in this case, roughness) of the prototype. In fact, the "art" of modeling has been to minimize distortions and judiciously interpret results from nondynamic models like these Froude models.

For this study complete similarity of forces is desired, not just superficial geometric similarity or similarity by artificially induced adjustments in the model. Also, unlike Reynolds similarity models, prototype systems of sediment transport have a free surface; unlike those one-component systems with a free surface to which Eq (1.1) applies, sediment-transporting systems involve two components, fluid and sediment. Consequently, additional modeling criteria are required.

Buckingham (1914) proved that the minimum number of dimensionless force ratios necessary to specify a system is n-m; m is the number of fundamental dimensions used and n is the number of independent, fundamental variables that fully characterize the conditions of a system, from which the force ratios are derived. In most physical problems, m equals three: mass, length, and time. If a variable is overlooked, then some dynamic aspect in the model is left unspecified. On the other hand, an extraneous variable unnecessarily and redundantly overspecifies forces acting in the system. Thus, the set of n fundamental variables and the set of n-3 derived

force ratios must be both necessary and sufficient in specifying the system studied.

Buckingham (1914) showed further that, in terms of uniquely and completely specifying a system, a set of n-3 force ratios is equivalent to any set of n-3 dimensionless parameters derived from a dimensional analysis of the same fundamental set of n independent variables. This is because a set of n-3 parameters could explicitly represent any one of the many sets of force ratios, each of these latter sets being a particular group of force pairings. In addition, there are an infinite number of sets of n-3 dimensionless parameters that could implicitly represent any of those sets of force ratios, since each parameter could theoretically be multiplied by any other dimensionless parameter to recover a particular force ratio (permitted as long as parameters are not eliminated, leaving some aspect of the system unspecified). Thus, for dynamic similitude, the numerical values of corresponding dimensionless parameters between model and prototype must be identical, just as numerical values of corresponding force ratios must be identical. A set of dimensionless parameters characterizing bed configurations is presented after the following discussion in which the fundamental variables are identified.

The fundamental set of variables.

The many sets of variables used to characterize sediment transport on the scale of bed configurations can be roughly

separated into four groups, originating or typically used by: Simons and Richardson (1963), Vanoni (1974), Southard (1971), and Maddock (1970). Common to all four groups is specification of the gravitational acceleration g acting on the system and the fluid by its density ρ and dynamic viscosity μ. Authors using slope as a variable, typical of the fourth group, do so generally because they study sediment transport on a larger scale, where regional slope is significant; this group will therefore not be considered further in this discussion. (At least on the smaller scale of bed configurations, slope is observed to be a dependent variable.) The sediment and flow are specified by the remaining three groups in various ways outlined below.

Sediment is specified by its density ρ_s and by either the mean or median grain diameter D. Since the median grain diameter is easier to measure than mean grain diameter, it will be used in this study. Vanoni (1974) and others also use a sediment sorting or standard deviation factor σ. However, since sorting has an effect essentially secondary to median grain diameter, effects of only median grain diameter will be focused on in this study. Hence, only relatively well-sorted sands are considered in this study.

The three groups differ most widely on the manner in which the flow is specified: the Simons group by flow power $\tau_o U$ and mean bed shear stress τ_o, Vanoni by mean bed shear stress τ_o and mean flow depth d, and Southard by mean flow velocity U and mean flow depth d. From the equations of mo-

tion it is evident that two variables are required to specify the flow, equivalent to a depth and a velocity. Because mean bed shear stress is proportional to the velocity gradient, it can be used to characterize either velocity or depth. Similarly, flow discharge Q and flow discharge per unit width q are proportional to the product of velocity and depth, so that they too could characterize either velocity or depth. Therefore, one different variable from each of the two following groups would characterize the flow: U, τ_o, $\tau_o U$, Q, q and d, τ_o, $\tau_o U$, Q, q.

Brooks (1958) showed that mean bed shear stress can be double-valued, where certain values specify two configurations rather than one. Although this does not invalidate sets using bed shear stress as a variable for scaling purposes, it does mean that such a set could possibly characterize the wrong configuration during a scaling procedure. If the same set of fundamental variables used for scaling are to be later correlated with different bed configurations (see Part III), then variables of that set should be single-valued for explicit one-to-one correlation. Mean bed shear stress and flow power, therefore, are not used here as fundamental variables.

Furthermore, because a bed configuration could be thought of as forming in a sheet flow of infinitely wide extent, width is not considered a fundamental variable. Therefore, flow discharge per unit width is preferable to flow discharge as fundamental variables are selected. That leaves two of the three following variables for specifying the flow: d, U, q.

From the above considerations, the following set of $n = 7$ fundamental variables is seen to characterize bed configurations: gravitational acceleration of the surrounding force field, density and dynamic viscosity of the fluid, density and median grain diameter of the sediment, and mean flow depth and mean flow velocity of the flow. This set characterizes the entire range of variability of bed configurations since the entire range of variability of the force field, the fluid, the sediment, and the flow are fully specified. One might be prompted to eliminate some variable from the set because its effect over some range of its variability is small. However, the full set of seven variables is the fundamental set over all conditions since the concept of dynamic similitude is not restricted to a single narrow range of variation.

That these seven variables comprise the fundamental set is both corroborated by dimensionless plots of these variables versus bed phase (see Part III), which lack the scatter and overlap of points indicating omission of a variable and parallelism of points to an axis indicating an extraneous variable, and verified by the modeling test reported in Part II.

Determination of dynamic similitude for bed configurations.

For $n = 7$, four dimensionless parameters are necessary and sufficient to characterize bed configurations. One set that explicitly represents dimensionless force ratios is:

the Froude number $U/(gd)^{1/2}$, the ratio of gravity forces to total inertial forces; a depth Reynolds number Ud/ν, the ratio of viscous forces to inertial forces; ρ_s/ρ, the relative density of the components; and d/D, an index of system geometry. These parameters are cast in a dimensional analysis based on quotients of U, d, and ρ.

Dynamic similitude for bed configurations between a prototype and model is expressed by the following set of equivalencies between corresponding dimensionless parameters:

$$\left(\frac{U}{(gd)^{1/2}}\right)_r = 1 \tag{1.2}$$

$$\left(\frac{Ud}{\nu}\right)_r = 1 \tag{1.3}$$

$$\left(\frac{d}{D}\right)_r = 1 \tag{1.4}$$

$$\left(\frac{\rho_s}{\rho}\right)_r = 1 \tag{1.5}$$

After realizing that mean-flow-depth ratio and median-grain-diameter ratio are equivalent dimensionally to any length scale, an arithmetic manipulation of the above equations leads to the equations governing dynamic similitude for bed configurations:

$$1_r = \left(\frac{\nu_r^2}{g_r}\right)^{1/3} \tag{1.6}$$

$$\left(\frac{\rho_s}{\rho}\right)_r = 1 \tag{1.7}$$

For a prototype of quartz sand and water, there are two degrees of freedom for model construction. Selection of any two of the following quantities fixes the scale value of all other independent variables in a dynamically similar model: gravitational acceleration scale, a length scale, a fluid, or a sediment.

For practical purposes, the gravitational acceleration scale will equal one for almost all laboratory models. The determining equations then reduce to:

$$1_r = \nu_r^{2/3} \tag{1.8}$$

$$\left(\frac{\rho_s}{\rho}\right)_r = 1 \tag{1.9}$$

In Eqs (1.8) and (1.9) there is only one degree of freedom, where selection of only one of the following fixes the value of all other variables in a dynamically similar model: a length scale, a fluid, or a sediment.

That one of the above equations is identical to Eq (1.1) for one-component flow systems comes as no surprise: although the complete equations of motion for one-component and two-component flows must be dissimilar, they are both based on a set of variables specifying the flow. According to a theory of similarity, equivalencies of force ratios as expressed in Eqs (1.8) and (1.9) are a necessary condition for dynamic scale modeling. However, in the absence of governing equations for two-component systems, only a comprehensive test as reported in Part II of this study can verify whether these

equations are sufficient for dynamic scale modeling of bed configurations.

Laboratory implementation of scale modeling.

The limiting factor in Eqs (1.8) and (1.9) has to be selection of the model fluid. Even modest scale ratios require kinematic viscosities for the modeling fluid that are substantially lower than water. Of the few fluids that do allow even a modest scale ratio, up to about 4, all are either flammable, toxic, volatile, prohibitively expensive, or unavailable. Those compressed or cooled gases that appeared to have potential as modeling fluids usually share one or more of these shortcomings and, more importantly, would not have a free surface, which the natural prototypes have. Required pressures up to about 70 atmospheres or temperatures down to -15°C would also have to be dealt with.

Large scale ratios (greater than 15 to 20) are not feasible, primarily because proper modeling fluids do not exist; however, if one did exist, there would probably still be the presence of nonsimilar cohesive effects in the very fine sediment of the model. For these reasons, dynamic scale modeling of sediment transport has been largely ignored by engineers and geologists. However, if one focuses on sediment transport at the scale of bed configurations, even scale ratios as modest as 2.5 would prove worthwhile since the range of flow depths of such a model--up to 2.5 m--would definitely overlap that range of depths of greatest sedimentological

interest (see Fig. 1.1).

A fluid that is safe, inexpensive, readily obtainable, and properly wets its model sediment is water. At a temperature of 80°C the scale ratio relative to a standard temperature of 10°C (selection discussed in Part III) is about 2.33. For scale ratios for lesser temperatures in the model see Fig. 1.2; for scale ratios relative to different prototype temperatures divide the old scale ratio for $\frac{T_{10}}{T_m}$ by the scale ratio for $\frac{T_{10}}{T_{new}}$ (maximum scale ratio about 2.75). Because the quotient (ρ_s/ρ) for water changes by only 3% with a temperature change from 0°C to 80°C, quartz sand or quartz-density sand can be used as the model sediment.

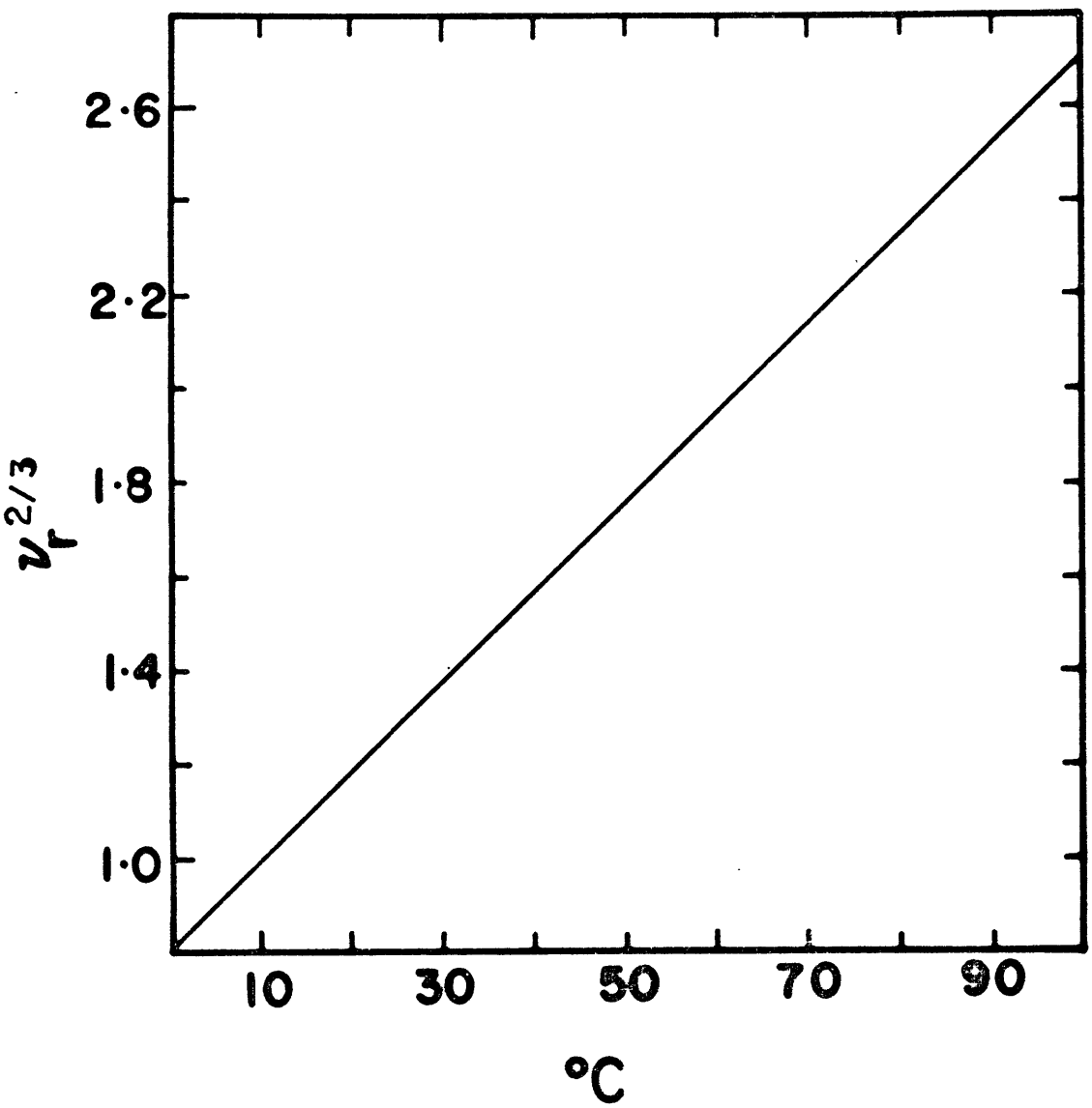

Fig. 1.2. Scale ratios at different water temperatures, relative to $\nu = 1.31\ cm^2/sec$, at 10°C. (After Handbook of Chemistry and Physics, 1976.)

PART II: TEST OF DYNAMIC SCALE MODELING

CRITERIA FOR TEST

A test was conducted in which dependent measures for two flume runs, a cold-water prototype and a hot-water model, were compared to verify that Eqs (1.8) and (1.9) determine the conditions for dynamic scale modeling of bed configurations. The success of this test depended upon three factors: 1) the completeness of the set of fundamental variables (discussed in Part I), 2) the adequacy of the test criteria, 3) the quality of the measurements. Yalin (1965) actually made a test of dynamic scale modeling, but his results were limited to a suggestive photograph of two geometrically similar bed configurations.

Since a fundamental set of variables implicitly specifies the forces acting in the system, the geometry and kinematics of that system are also specified. If forces cannot be measured directly, measures of both the geometry and kinematics of each system should be compared. In this test the geometry for each run was characterized by individual cumulative frequency curves for height and spacing of the observed bed forms, which were ripples. Ripple spacing was defined by the distance between brinkpoints of successive ripples, and ripple height was defined by the vertical distance between the brinkpoint and the lowest point of the trough immediately downstream. Kinematics for each run was characterized by a cumulative frequency curve of ripple migration times (time

rates are motion-related and so are kinematic), defined by the elapsed time between passage of successive ripple crests past a reference section.

The dynamical aspects of each variable are most apparent when each is considered dimensionlessly as quotients involving mass, gravitational and viscous forces: $\lambda\left(\frac{g}{\nu^2}\right)^{1/3}$, $A\left(\frac{g}{\nu^2}\right)^{1/3}$, $t_m\left(\frac{g^2}{\nu}\right)^{1/3}$. Corresponding curves for each variable should coincide if the two flume runs are dynamically similar. However, results are plotted dimensionally with one curve of each pair scaled to overlap the other, in order to illustrate the difference in results between scaled and unscaled data.

PROCEDURE

Apparatus and determination of independent variables.

Both runs were made in the same tilting, closed-circuit flume, with 15.6 cm maximum width and 8 m length, which recirculated both sediment and water (see Figs. 2.1 and 2.2). The channel itself was constructed of Plexiglas. The flow was pumped by a centrifugal pump, powered by a 1 1/2 hp motor, through a single 2" I.D. copper return pipe back to the headbox. Ambient inlet turbulence was damped by a baffle at the juncture of the headbox and channel and by straws placed just downstream. Surface waves at the inlet were damped by a board resting on the water surface, placed downstream of the straws. Discharge was controlled by a gate valve mounted in the return pipe and was measured by a precalibrated orifice

meter (diameter = 1.6") upstream of the gate valve. Discharge readings were made from a U-tube manometer filled with s-tetrabromoethane for the low-discharge model run and mercury for the higher-discharge prototype run and connected to pressure taps off the orifice meter.

The nature of the experiment required that conditions be set and monitored with a precision unusual in flume experiments. Mean flow depth was defined as the time-averaged depth at the wall of a reference section, denoted by a vertical line on the flume wall. A 16-mm motion picture camera connected to a timing device photographed the flume wall at constant time intervals. Flow depth was measured from the movie film frame by frame. Measurements of nearly 1500 frames from a trial run showed statistically that measurement of 200 consecutive frames was sufficient to determine the mean flow depth to within 1 mm accuracy. Since the values of depth and velocity were specified for the model by measurements of depth and discharge in the prototype (velocity was calculated from measurements of discharge, depth, and channel width), flow depth in the model had to be first determined and then adjusted by adding or subtracting water from the channel. Flow discharge was also adjusted accordingly, in order to set the mean flow velocity for the model run; this procedure yielded a velocity accurate to within about 0.2 cm/sec.

During a run, flow depth was monitored constantly using a ruler taped to the flume wall. From these readings an approximate rate of water loss was calculated. Water was re-

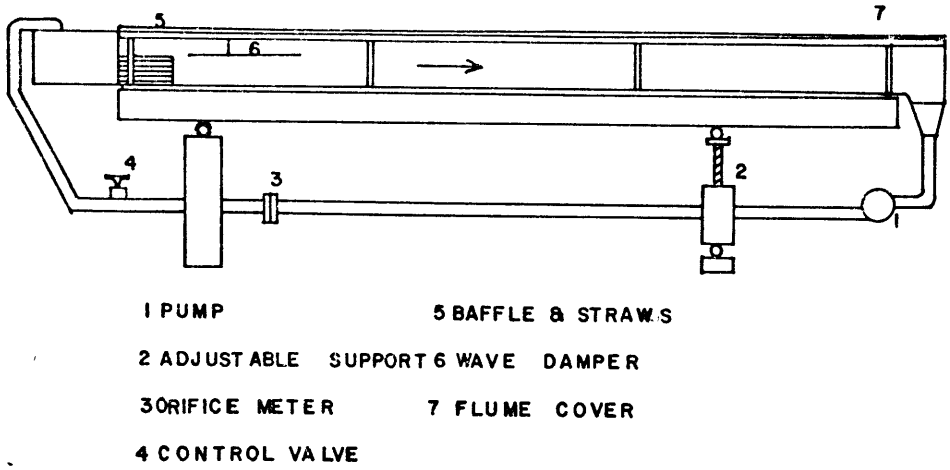

Fig. 2.1. Schematic diagram of 8 m flume.

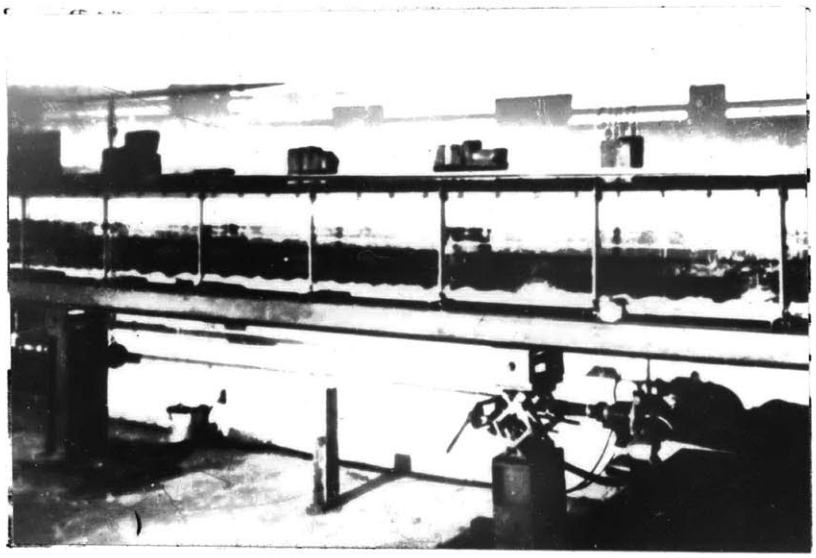

Fig. 2.2. Photograph of 8 m flume. Flow from left to right.

placed at that approximate rate by means of a valve-controlled, slowly dripping spout. The channel was covered to minimize water loss from evaporation.

Temperature for both runs also had to be carefully controlled and monitored. For the cold-water prototype, water was drawn from the tailbox, circulated through a cold-water reservoir cooled by a thermostat-equipped refrigeration coil, and returned to the tailbox at a point lower than from where it was drawn. Temperature for the hot-water model was controlled by a thermostat-equipped L-shaped immersion heater placed in the channel well downstream of the reference section. Channel covers used during both runs minimized temperature variations, which were about ±1°C, as monitored by a thermometer in the channel.

For the purposes of this test, data measured at the sidewall were just as valid as data measured down the centerline of the channel, provided that the manner of measurement was the same in both runs. Thus, the narrowness of the flume did not affect the outcome of the test. However, because measurements of depth and also of the dependent variable were made from photographs of the sidewall, it was important that wall effects scaled from one run to the other. This was done by scaling the width, using the full channel width in the prototype and a false wall in the model. The false wall was constructed of smooth-surfaced bricks, 25 cm high and exactly wide enough (6.2 cm) to fill the unused portion of the channel.

Because the return system of the flume was not scaled

from one run to the other, ambient inlet turbulence and inlet shear stress did not scale. Therefore, the reference section was positioned for both runs so that crossing ripples were fully developed, based on observations at equilibrium; it was not positioned in the model according to a scaled length downstream from the inlet because entrance effects were unscaled.

Very well sorted sands were used, each having been sieved into 1/4-ϕ fractions: 0.23±.02 mm for the model and 0.38±.03 mm for the prototype. Although sorting was not a variable, the very small standard deviation of each size did coincidentally scale.

Measurement of dependent variables.

Two methods for recording measurements of dependent variables were tried. The first amounted to a streamwise profile of the bed made at intervals of about three hours. (Three hours assured independence of the successive profiles, as determined by visual observation.) The second was time-lapse cinematography of about a one-meter reach. The second method was chosen over the first for the following reasons.

Migration time turned out to be the variable most sensitive to changes in the independent conditions, so it could be considered the most critical criterion of the test. Cumulative frequency curves of migration time did not match when using the first method, probably because the interdependence of adjacent ripple-migration rates statistically biased the

data. For the second method, migration times were recorded from individual ripples over a period of time sufficient to minimize interdependence of successive bed forms. Also, measurements at intervals of a few minutes instead of a few hours was far more likely to capture those transient variations, such as the occurrence of short-lived, fast-moving ripples, that were an integral part of the statistical characterization of each run. Thus, a sequence of 100 ripples on film provided a more varied and therefore a more representative sample than a sample of ten profiles of ten ripples apiece.

Time-lapse cinematography provided a permanent record from which many dependent variables could be determined. The time interval was adjusted to capture a particular ripple about six times in the field of view. This adjustment was an economical use of film and a time-telescoping feature. The field of view spanned about three to four ripples. Both the time interval and field of view were scaled from prototype to model to avoid any implicit bias in the data. A clock and a horizontal/vertical scale were kept in the field of view for references.

The easiest way to read the film was to mount it on a 35 mm downward-projecting microfilm reader. Thousands of frames were tediously scrutinized in dark corners of the library. In the future, if the same film were to be analyzed for more than one purpose, digitizing would be highly recommended.

According to the definition for ripple migration rate, the number of constant time intervals between frames was counted between successive crests crossing the reference section. Since the instant of crossing was generally not recorded on film, that time was interpolated by assuming a constant migration rate between two successive frames, one taken before and one after crossing the reference section. The crest position was recorded for each frame by laying a calibrated grid on the film projection, lining up reference marks on the grid with the reference section, and making a reading. About 100 ripples for each run were so measured.

Measurements of ripple spacing and ripple height made more efficient use of the film than measurements of migration times. Measurements were made every five frames, recording the position of every crest/trough pair in the field of view on a sheet of graph paper lying on the projection, and taking measurements later. Ripples generally maintained their identity over this interval, but their form changed sufficiently that alternate configurations (every ten frames) were independent of one another. About 200 ripples were measured for geometry for each run.

General operating procedure.

Once the initial conditions of a run were set, a period of about four days elapsed before filming commenced. During that time, the bed came to a dynamic equilibrium, achieved when a characterization of the bed configuration was the same

in successive observations. Depth was measured from the film and experimental conditions adjusted accordingly. After another period of about four days, during which the bed was again observed to come to equilibrium, the final time-lapse film was shot. A typical configuration is shown in Fig. 2.3.

A length scale of 1.66 between the two runs was based on the limitations of temperature control in the cold-water prototype. Experimental conditions for model and prototype are described in Table 2.; note that time and velocity dimensions scale as the square root of the length scale.

RESULTS AND DISCUSSION

Corresponding pairs of cumulative frequency curves for each of the three dependent variables appear in heavy line in Figs. 2.4, 2.5, and 2.6. The scale ratio of 1.66, though small, was sufficient to produce a distinct separation between each pair of curves. In each of the three figures, the curve to the far left is for the hot-water model and the curve to the far right is for the cold-water prototype. The dashed curve is the scaled-up curve of the model, where data were multiplied by 1.66 for height and spacing and $(1.66)^{1/2}$ = 1.29 for migration times.

Because of the small samples used for each curve (100-200 measurements), wide rather than narrow cumulative intervals were plotted in order to smooth out the curve. Also, curve tails were not plotted because of the very small samples represented in those intervals.

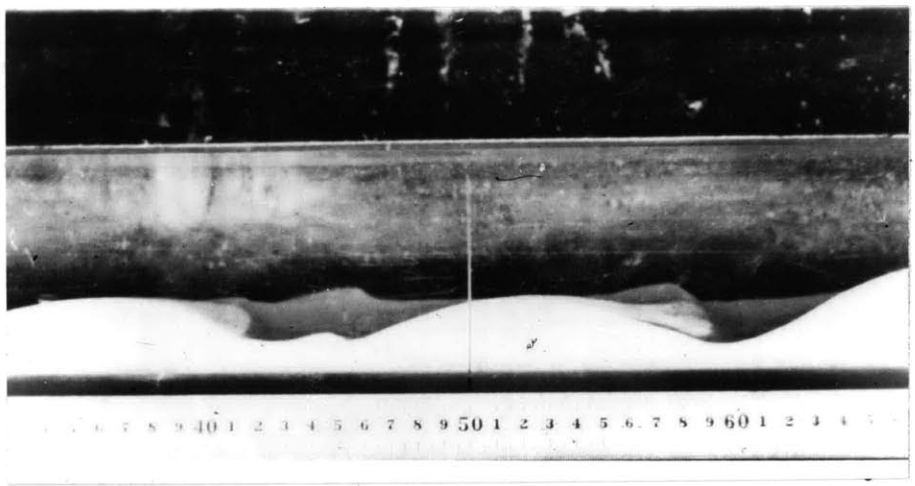

Fig. 2.3. Photograph of typical ripple configuration, model run; flow left to right.

In Figs. 2.4-2.6 the coincidence of scaled-up model and unscaled prototype curves is excellent. The gap separating the two curves in each figure is far less than the interval between unscaled model and prototype curves. That there is any separation between scaled-up model and unscaled prototype curves is probably a result of the small samples used. Adding or subtracting even 10 to 20 sequential measurements (sequentially at the beginning or end of a set of data) to the sample for a curve was sufficient to shift that curve a significant fraction of the gap. It is likely that a sample of 1000 or so measurements for each dependent variable of both runs would practically eliminate this gap in Figs. 2.4-2.6. Such a monumental effort is not required, however, since the accompanying results are acceptable.

As noted before, measurements for each curve were sequential; that is, intervals of film were not randomly skipped. However, there were extremely slow-moving forms resembling sand waves observed in the hot-water run which biased the sample of migration times to the low side. Elimination of these measurements brought the two curves into agreement. It is believed that these features were either an artifact of not scaling the return system from prototype to model or merely randomly occurring sand waves, occurring so infrequently that, for a sample of 100 measurements per run, their occurrence could not be meaningfully compared from one run to the other.

An additional means of comparing the data from the two

TABLE 2.1: Experimental conditions for flume runs, adjusted for dynamic similitude at a scale ratio of 1.66

Variable	Cold-water run (large-scale)	Hot-water run (small-scale)
Water temperature T (°C)	13.5	49.9
Fluid viscosity μ (poise)	1.19×10^{-2}	0.55×10^{-2}
Fluid density ρ (g/cm^3)	0.999	0.988
Channel width w (cm)	15.6	9.4
Mean flow depth d (cm)	9.3	5.6
Mean flow velocity U (cm/sec)	29.2	22.7
Sediment size D (mm)	0.38	0.23
Sediment density ρ_s (g/cm^3)	2.65	2.65
Time-lapse filming rate (min)	15.0	11.6

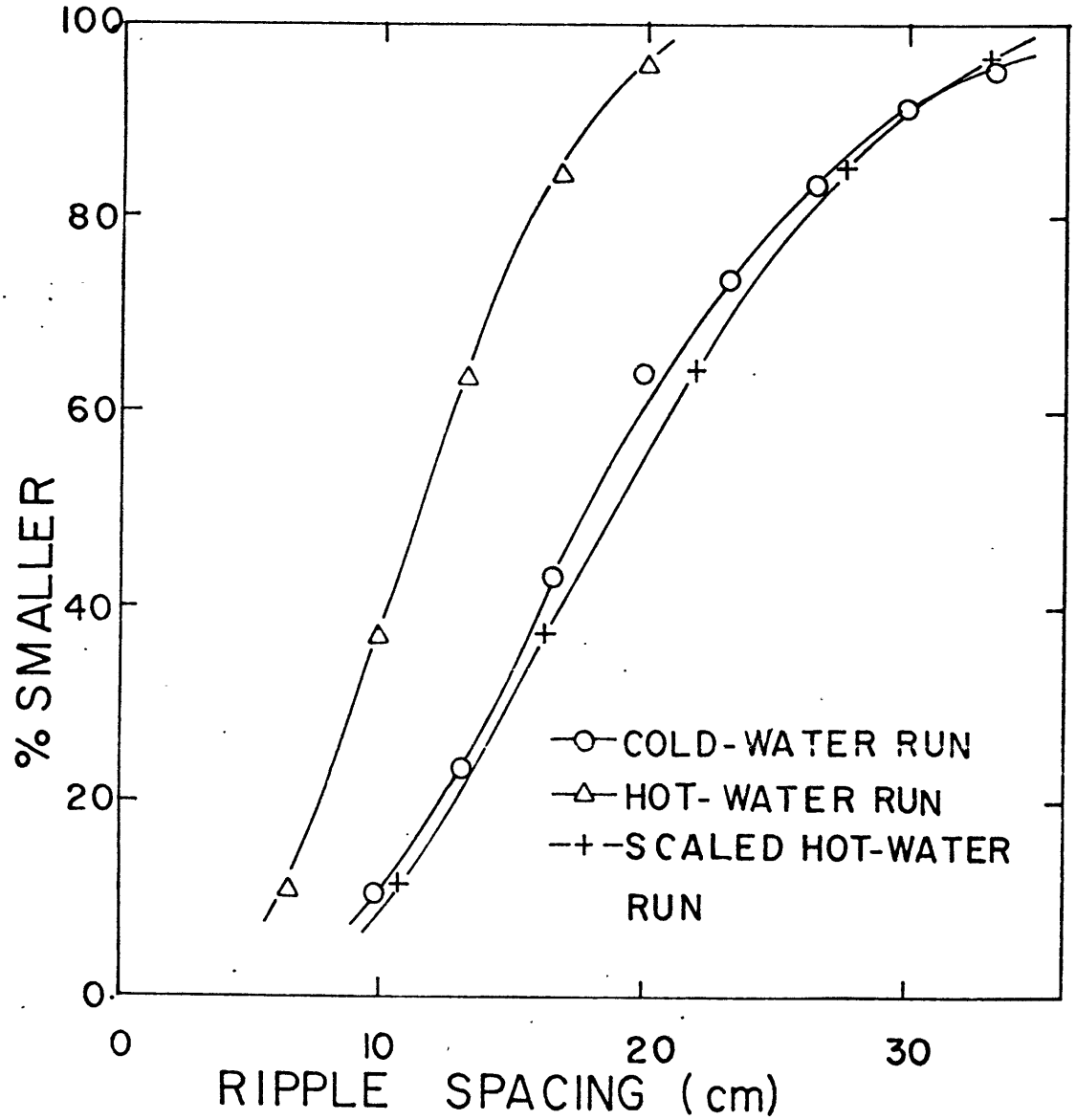

Fig. 2.4. Cumulative frequency curves for ripple spacing.

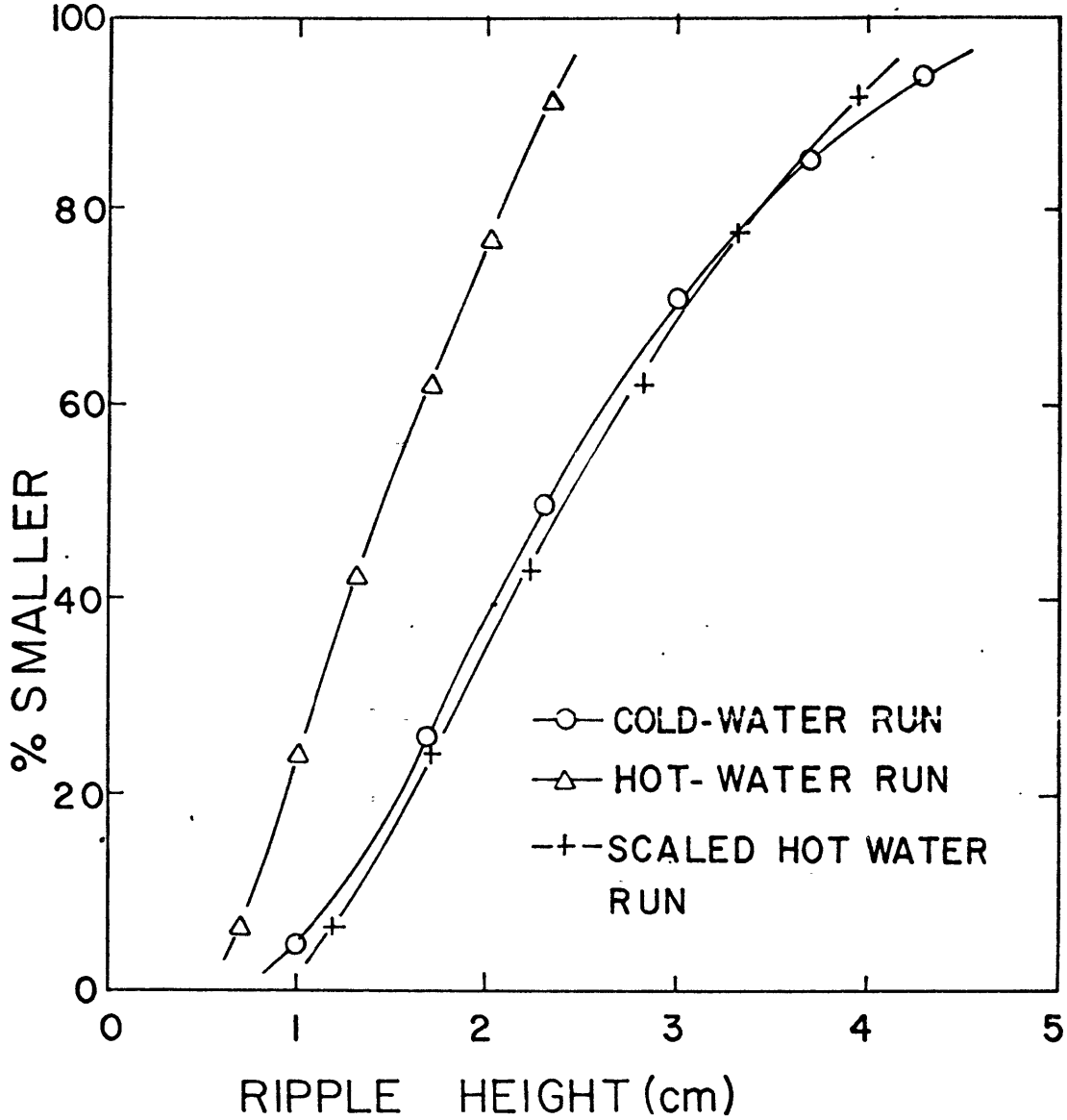

Fig. 2.5. Cumulative frequency curves for ripple height.

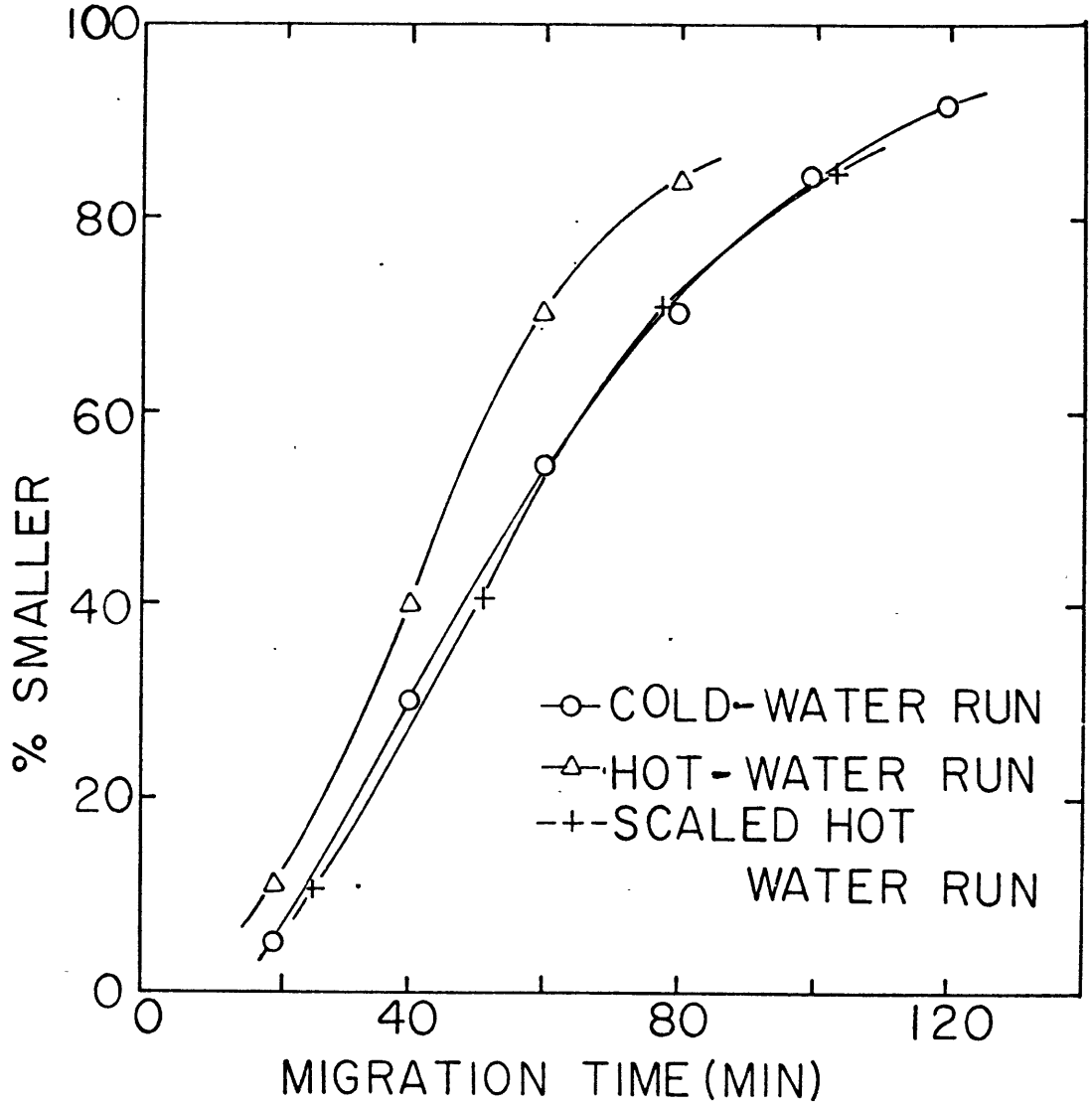

Fig. 2.6. Cumulative frequency curves for ripple migration times.

runs was the correspondence between the mean and standard deviation of model and prototype curves for each dependent variable. These results, shown in Table 2.2, showed remarkably good agreement, considering the small samples involved.

An additional hot-water run was made at a velocity slightly higher than the first in order to see whether a change in the independent conditions made any difference in how curves for each dependent variable plotted. The velocity of the second run was higher by 0.5 cm/sec, or about twice the experimental error in the velocity measurement. Frequency curves for ripple spacing and ripple height did not plot appreciably differently for the additional run than they did for the first run. Yet, the curve for migration time of the second run was shifted considerably to the right relative to the curve for the first. This indicates that ripple geometry was not so sensitive to a change in the independent conditions that geometric measures alone would be sufficient criteria for the scale modeling test. However, the shift of the curve for migration time, being a significant percentage of the interval between the first hot-water curve and the prototype curve, showed that dependent variable to be highly sensitive to a change in the conditions. Therefore, a variance in the independent conditions of the model on the order of the experimental error would have been sufficient to invalidate the correspondence of model and prototype curves. Hence, a fortuitous correspondence of data can be

TABLE 2.2: Means (M) and standard deviations (σ) of frequency distributions of experimental characteristics.

		Ripple height (cm)	Ripple spacing (cm)	Ripple migration Time (min)
Cold-water run	M	2.3	18.4	65.5
	σ	1.0	7.6	38.2
Hot-water run	M	1.3	11.6	53.2
	σ	0.6	4.5	31.0
Scaled hot-water run	M	2.2	19.2	68.6
	σ	1.0	7.5	40.0

ruled out.

The results of the modeling test clearly substantiate that Eqs (1.8) and (1.9) determine the requirements for dynamic similitude of sediment transport:

$$l_r = \nu_r^{2/3} \tag{1.8}$$

$$\left(\frac{\rho_s}{\rho}\right)_r = 1 \tag{1.9}$$

Each of the fundamental variables on which these equations are based specifies some aspect of the system--the force field, the fluid, the sediment, or the flow--over the entire range of variability of that variable. Therefore, the conclusions of this modeling test can be extended over the entire range of these variables since no new variables need be introduced at some range of conditions in order to "respecify" dynamic similitude. Thus, the results of this test have established two conclusions that imply one another:

1) dynamic scale modeling of bed configurations is possible, and

2) the fundamental set of seven variables fully characterizes all dependent aspects of any bed configuration.

These conclusions set the themes for the balance of this study. Because the set of fundamental variables is complete, it is appropriate that that set be correlated with different classes of bed configurations as a step toward understanding sediment transport processes; this is done in Part III. Also, principles of dynamic scale modeling are used in that section

in order that data measured at different temperatures can be compared. In Part IV a pilot study is reported in which techniques were developed for hot-water scale modeling at higher scale ratios and in larger flumes than were used for the test study. During the pilot study configurations in fine sands were observed in order to experimentally confirm features of the correlative plots constructed in Part III; these results are also reported in Part IV.

PART III: SYNTHESIS OF EXISTING DATA

INTRODUCTION

Correlation of fundamental variables with bed phases.

Correlation of variables of the fundamental set with dependent measures of a bed configuration is one of the first steps toward understanding the effects of each variable on sediment transport. Within a correlative framework, data from one system can be compared with data from another and trends in the configuration can be followed with changes in the fundamental variables.

If any variable was eliminated from the fundamental set of variables, some significant aspect of the bed configuration would be unspecified; consequently, that aspect would correlate with none of the remaining variables. Therefore, it is important that correlations be based on that set of variables that together fully characterizes a bed configuration. For example, the scatter of Yalin's (1977) plot of bed-form height versus flow depth can probably be attributed to his use of only one fundamental variable in the correlation. When possible, then, the prevailing depth, velocity, sediment size, and water temperature (quartz sand assumed) should be documented along with those observations of bed configurations made during field and laboratory studies.

Correlation of the fundamental variables with characterizations of the bed configuration (defined and later de-

scribed below) should be based on the full set of fundamental variables for the same reasons given for correlations involving individual dependent measures of the configuration. A bed state characterizes the average of many possible geometries through which the configuration varies at one set of conditions. A bed phase represents an aggregate of similar equilibrium bed states, each observed at different conditions. These bed phases are the characterizations correlated with the set of fundamental variables.

Bed phases are generally thought of in terms of the typical bed form described by a bed state. Thus, there are bed phases for ripples, dunes, bars or sand waves, antidunes, flat bed, and no movement. The first three phases refer to bed forms that are asymmetrically triangular in longitudinal cross-section. Using observations on the Wabash River (Jackson, 1975) as examples, heights and spacings of ripples are much smaller than those measures for dunes, on the order of 1-5 cm x 10-30 cm versus 5-120 cm x 1-30 m; also, bars or sand waves, measuring on the order of 30-200 cm x 20-500 m, tend to have low spacing-to-height ratios and have troughs relatively flatter than those of either ripples or dunes. In flume studies (e.g., Costello, 1974), dunes are observed to be larger than ripples but only as large as about 5-12 cm x 50-150 cm. Antidunes are generally symmetrical bed forms that are in phase with waves on the water surface. Flat bed and no movement bed phases are self-explanatory.

If one thinks of bed-form geometry as an effect of sedi-

ment transport processes, then bed phases distinguished by geometry must also be implicitly distinguishable by those processes. In fact, the above bed phases can be distinguished by processes as well as by geometry. Ripples (Raudkivi, 1963) are associated with a process of flow separation over a mound, where grains are intermittently entrained downstream of the crest at the point of reattachment of the separated boundary layer. Dunes are also associated with flow separation over a mound (Costello, 1974), but grain entrainment downstream of the crest is over a region where the relatively high shear stress of the just-reattached boundary layer re-equilibrates to the lower value of the wall boundary layer. Migration of bars can be approximated by a simple kinematic shock-wave model (Costello, 1974). This model is applicable only for conditions of general sediment transport over the bed, distinguishing bars genetically from ripples, which are associated with only intermittent transport over the bed. The genetic distinction between bars and dunes is that flow separation does not seem to be the outstanding process for bars as it is for dunes; this is suggested by the flat bar trough, associated with scour by a weak reverse-flow vortex and indicative of relatively low levels of shear stress in the separated boundary layer. Only the antidune bed phase is associated with a process for interaction between in-phase bottom and water-surface waves (Kennedy, 1963). Flat bed can be further divided into two bed phases: upper flat bed with high levels of continuous

sediment transport and lower flat bed with low levels of intermittent sediment transport. A state of no movement can occur over either a flat or rippled bed configuration, depending on the conditions. In certain velocity intervals (Chabert and Chauvin, 1967), lower flat bed or no movement can be thought of as metastable, appearing in lieu of ripples if the original configuration is flat. (Over these same intervals, ripples cannot be initiated but must be formed at other conditions or artificially imposed on the bed at these conditions.) Thus, two metastable bed phases can be added to the above group of bed phases.

Depth-velocity-size diagram.

The correlation between the set of fundamental variables and bed phases can be portrayed graphically. There is only one dimensional analysis of the set of fundamental variables that both permits the explicit expression of the environmental determinants in a correlative plot as well as reduces the number of dimensionless parameters characterizing bed configurations to three rather than four. That analysis, first proposed by Southard (1971), yields the following dimensionless parameters:

$$d\left(\frac{g}{\nu^2}\right)^{1/3},\ D\left(\frac{g}{\nu^2}\right)^{1/3},\ U\left(\frac{1}{\nu g}\right)^{1/3},\ \frac{\rho_s}{\rho} \qquad (3.1)$$

Specifying quartz-density sand and constant-temperature water makes the fourth parameter a constant. Reduction to

three parameters permits visualization of the complete one-to-one correlation of the specifying parameters with bed phase or a dependent variable in a three-dimensional diagram essentially contoured for the fourth variable. Specifying constant water temperature (gravitational acceleration is constant) makes all the nondimensionalizing coefficients constant, so that the independent parameters associated with the axes of the diagram are mean flow depth, mean flow velocity, and median sediment size. These explicit environmental determinants are easier to interpret sedimentologically than dimensionless parameters.

In this diagram, each data point is uniquely associated with a bed phase. Points of like bed phase are grouped into bed-phase stability fields, which define the range of conditions over which a bed phase is stable. Bed-phase stability fields are separated by boundaries, which seem to be narrow regions of gradational rather than sharp change.

The depth-velocity-size diagram has been used as a guide to investigation and as a framework for organizing data for laboratory studies (Southard and Boguchwal, 1973; Costello, 1974) and for field studies (Jackson, 1975; Dalrymple, 1976). However, in Southard's original presentation (1971) and in these above studies, data were plotted without regard to temperature. Recognition that data were actually imprecisely plotted forms the basis of discussion for the remainder of Part III.

Objectives.

Establishment of dynamic scale modeling for bed configurations is germane to the depth-velocity-size diagram in two ways. The first, underlying the discussion above, is verification that the fundamental variables on which the diagram is based comprise the entire fundamental set of variables. The second is that in order to meet the criterion of a constant-temperature plot, the dynamic equivalent of a system to one at a standard temperature can be determined using Eq (1.8) for dynamic similitude. (Eq (1.9) is unnecessary for this purpose since, for quartz-density sand, ρ_s/ρ is essentially constant over the whole range of water temperatures.)

Eq (1.8) can be used to illustrate the effect of disregarding temperature in a plot of data within an explicitly dimensional depth-velocity-size diagram. For example, taking two data points, one measured at 5°C and the other measured at 27°C, the length scale relative to one another is 1.5. By not plotting the dynamic equivalent of one of the points (to the temperature of the other), the sediment size and depth for that point are off by a factor of 1.5 and the velocity by a factor of about 1.22, a significant disparity. The plot of a point relative to a standard temperature is therefore shifted considerably as compared to a plot of that point relative to its observed temperature. Hence, for plots in two of the three dimensions of the depth-velocity-size

diagram, the net result of adhering to the criterion of a standard temperature would be a wholly different combination of data points per plot than would appear using nonrigorous plotting techniques.

The primary objective of Part III was to construct a three-dimensional depth-velocity-size diagram from existing flume data, taken from other studies, in such a way that data measured at different temperatures could be compared. If the data are plotted dimensionlessly, the effect of temperature is accounted for by the kinematic viscosity, which appears in each of the first three parameters in Eq (3.1). However, it is worth preserving the dimensional property of the diagram, which makes the diagram much easier to comprehend, interpret, and apply than as if it were dimensionless.

At the same time that data were normalized for temperature, observations of bed configurations were re-evaluated, since in the new synthesis of the data, new and different comparisons of observations would likely be made. Observations were re-evaluated according to the hierarchy of bed forms observed at a particular set of conditions; hierarchy here denotes that bed forms are elements of which the configuration as a whole is composed. This approach was taken for increased resolution in the conception of bed phase.

CONSTRUCTION OF DIAGRAMS

Temperature normalization of data.

Data for the depth-velocity-size diagram were taken from those sources that documented temperature as well as mean flow depth, mean flow velocity, and median grain size for each run; an adequate description of the bed configuration was an additional requirement of a source, so that observations could be meaningfully re-evaluated. Sources used and the approximate range of normalized sediment sizes for each appear in Table 3.1.

There are two equivalent ways of preserving the dimensionality of the data: plot data in dimensionless form and relabel the axes in accordance with a standard temperature, or plot data already normalized to a standard temperature. The first approach was used to plot the data; however, data were normalized before being plotted in order to determine at what constant intervals two-dimensional plots of the three-dimensional diagram could be made, a procedure described in the next section.

Normalization of the data or of the coordinates of the axes for temperature is determined by Eq (3.2) below. P is the value of a dimensionless parameter, either as calculated from the data or as read from one of the axes, C is the value of the non-dimensionalizing coefficient of that parameter at the standard temperature, and L is the unknown temperature equivalent and multiplicand of that particular coefficient:

TABLE 3.1: Sources used for diagram and the range of normalized sediment sizes for each.

SOURCE	APPROXIMATE RANGE OF SEDIMENT SIZES (MM)
Barton and Lin, 1955	0.22
Costello, 1974	0.72-1.05 and 1.60
Davies, 1971	0.17-0.19
Guy, Simons, and Richardson, 1966	0.22-0.68 and 1.1
Hill, Srinivason, and Unny, 1969	0.12, 0.2 and 0.4-0.5
Nordin, 1976	0.30 and 1.14
Pratt and Smith, 1972	0.55-0.65
Southard and Boguchwal, 1973	0.55-0.75
Vanoni and Brooks, 1957	0.13 and 0.17-0.2
Williams, 1967 and 1970	1.65
Willis, Coleman, and Ellis, 1972	0.12

$$P = CL \tag{3.2}$$

Eq (3.2) is an expression of the requirement for dynamic similitude, that corresponding dimensionless parameters of the measured system and the equivalent system at the standard temperature be numerically equal. One solves for L, the normalized dimensional value, where C is already determined by the standard temperature and P is simply calculated from the data or read from one of the axes.

The standard temperature selected was 10°C. That temperature seemed representative of many natural environments: deep ocean bottom water is typically no warmer than a few degrees Celsius, nearshore marine currents range from near-freezing temperatures to about 30°C, and a typical mid-continental river ranges from near-freezing temperatures in winter up to about 25°C in late summer and averages about 10°C through the whole year.

Plotting the data.

Two-dimensional "projections" of the three-dimensional depth-velocity-size diagram were produced by first plotting the natural logarithm of dimensionless parameters for each data point on arithmetic paper and then relabeling the axes dimensionally. (A projection is defined for this study as the intersection of a plane with the depth-velocity-size diagram, where that plane is parallel to two of the axes of the diagram.) Logarithmic axes were used for the plot of

the depth-velocity-size diagram to focus more sharply on the large changes in the bed configuration occurring with small variations in the controlling conditions, especially sediment size, and to bring the proportions of the axes in line to one another, since dimensionless values of depth were two orders of magnitude greater than dimensionless values for the other two parameters. The depth-velocity-size diagram is implicitly dimensionless, since the dimensionlessness or dimensionality of the diagram is essentially determined by the labeling of the axes, as indicated by Eq (3.2). In order to maintain the true dimensionless proportions of the axes to one another, data were plotted dimensionlessly.

To maximize the potential number of data points per projection, an interval about some value rather than a precise value for the constant third parameter was used for each projection. One advantage of using dimensional numbers instead of dimensionless values was that physically meaningful quantities could be discriminated to make the width of these intervals as wide as possible, yet narrow enough that their identity with the constant variable was maintained. The intervals settled upon were ±0.01 mm of median grain diameter for depth-velocity diagrams and ±7% of mean flow depth for velocity-size diagrams. About thirty points falling in an interval were considered the minimum number necessary to make a particular projection worth plotting. As a result of these stipulations, four velocity-size diagrams and seven depth-velocity diagrams were plotted (Figs. 3.1-3.11; for data

plotted according to source rather than bed phase, see Appendix). Intervals are listed in Table 3.2; data falling outside these intervals could not be used.

After the data had been plotted, points were grouped according to bed phase. The bed phase of each point was characterized by the hierarchy of bed forms, as defined earlier, and where relevant, by the distribution of minor (smaller) bed forms over the bed and by the configuration of the bed previous to the run. Five bed phases in addition to those described in the first section of Part III were identified: bar plus ripple, bar plus dune, dune plus ripple, flat backed dune plus ripple, and flattened dune bed phases. All bed phases are listed in Fig. 3.14, the legend to Figs. 3.1-3.13 (fold out for reference).

Certain data were interpreted as follows. Descriptions of dune-like ripples or ripple-like dunes (Guy et al., 1966) were considered to refer to bars. Sand waves described by Vanoni and Brooks (1957) and Barton and Lin (1955) seemed not to be bars but elongate, flat-topped dunes with ripples forming in their wakes. Also, the flattened dunes of Pratt and Smith (1972) and the transition configurations of Guy et al. (1966), similar in geometry and conditions for stability, were classified together in one bed phase. Experimental confirmation of these interpretations and of the five newly distinguished bed phases is reported in Part IV.

TABLE 3.2: Interval of control variable for each projection.

FIG.#	PROJECTION	CONTROL VARIABLE	INTERVAL
3.1	Velocity-size	flow depth	8.5 ± 1 cm
3.2	Velocity-size	flow depth	20 ± 1.5 cm
3.3	Velocity-size	flow depth	30 ± 2 cm
3.4	Velocity-size	flow depth	40 ± 3 cm
4.5	Velocity-size	flow depth	50 ± 3.5 cm
3.5	Depth-velocity	sand size	0.13 ± .01 mm
3.6	Depth-velocity	sand size	0.22 ± .01 mm
3.7	Depth-velocity	sand size	0.31 ± .01 mm
3.8	Depth-velocity	sand size	0.55 ± .01 mm
3.9	Depth-velocity	sand size	0.62 ± .01 mm
3.10	Depth-velocity	sand size	1.07 ± .01 mm
3.11	Depth-velocity	sand size	1.60 ± .01 mm

Three-dimensional interpolation of boundaries.

Each projection was subdivided into bed-phase stability fields by boundaries separating groups of data points. However, after the most apparent boundaries or portions of boundaries were delineated, much of the area of most projections still remained undefined. Boundaries were better defined and fully delineated by a process of three-dimensional interpolation, involving locating the lines of intersection of a given projection with orthogonal projections, plotting on those lines the intersection of those already-delineated boundaries contained in each orthogonal projection, and interpolating best-fit boundaries through these points of intersection, consistent with the identity of nearby data points. (Extrapolation of certain boundaries is described below.) Thus, analogous boundaries in orthogonal planes intersected, as they should. With this technique, any projection of the depth-velocity-size diagram intermediate or extrinsic to those projections presented here can be constructed, as long as dimensionless, logarithmic axes are used, dimensional relabeling being done later.

Boundaries between the ripple stability fields of the two velocity-size diagrams at the shallowest depths (Figs. 3.1 and 3.2) were delineated largely by extrapolation. Existing portions of these boundaries were extrapolated in a linear fashion so that they remained parallel to one another. This was based on the assumption that the increase in velocity

necessary to span either the metastable no-movement or metastable lower-flat-bed fields was constant, regardless of grain size, thereby defining the parallelism of the three boundaries about these two adjacent stability fields. Intersections of these boundaries were plotted onto the intersecting orthogonal depth-velocity diagrams. In each depth-velocity diagram, boundaries were extrapolated to deeper depths through those points just plotted at 8.5 cm and 20 cm flow depths, in such a way that boundaries about the metastable no-movement and metastable lower-flat-bed stability fields were parallel. This was based on an assumption similar to the one above, but in reference to depth instead of grain size. Intersections of these boundaries with the two orthogonal velocity-size diagrams at 30 cm and 40 cm flow depth, in each of five depth-velocity diagrams (Figs. 3.5-3.9), were then plotted. Finally, boundaries in these two velocity-size diagrams were interpolated through these points of intersection.

The various dune phases had to be grouped into one general bed-phase stability field for dunes because there were insufficient data points for delineation of each subfield. The boundary between the dune and upper-flat-bed stability field was delineated in the following way. That boundary in each of the depth-velocity diagrams for fine and medium sand was first fully delineated by extrapolating up through clusters of data points at depths of 8.5 cm and 20 cm. Intersections of this boundary with the four ortho-

gonal velocity-size diagrams, in each of these five depth-velocity diagrams, were then plotted. Boundaries in the velocity-size diagrams were then fitted between these points of intersection, consistent with nearby data points.

It is evident from the above descriptions that often many cycles of delineation/intersection/interpolation were necessary to minimize overlap of fields caused by data of the same bed phase plotting on either side of a boundary. Iterations were feasible because, instead of fixing a line by a best fit through a series of data points, best fit was through a series of data points and a series of small rectangles, each defining the error in plotting the intersections of a boundary in orthogonal projections. (In the absence of other constraints, only straight lines or straight-line segments, as opposed to curves, were ever interpolated or extrapolated.) Thus, the final positioning of boundaries was legitimately more variable. These rectangles are a result of the "thickness" in each of two intersecting projections (see Table 3.2). There was a small uncertainty in every velocity reading of a boundary where it intersected the "plane" of the orthogonal projection, due to the width of the interval over which the orthogonal plane was plotted. That uncertainty would plot as an error bar for velocity in the orthogonal projection, its length dependent upon the steepness of the intersecting boundary. Also plotted onto this plane would be a second error bar, parallel to the depth or size axis. The length of that error bar equalled the width

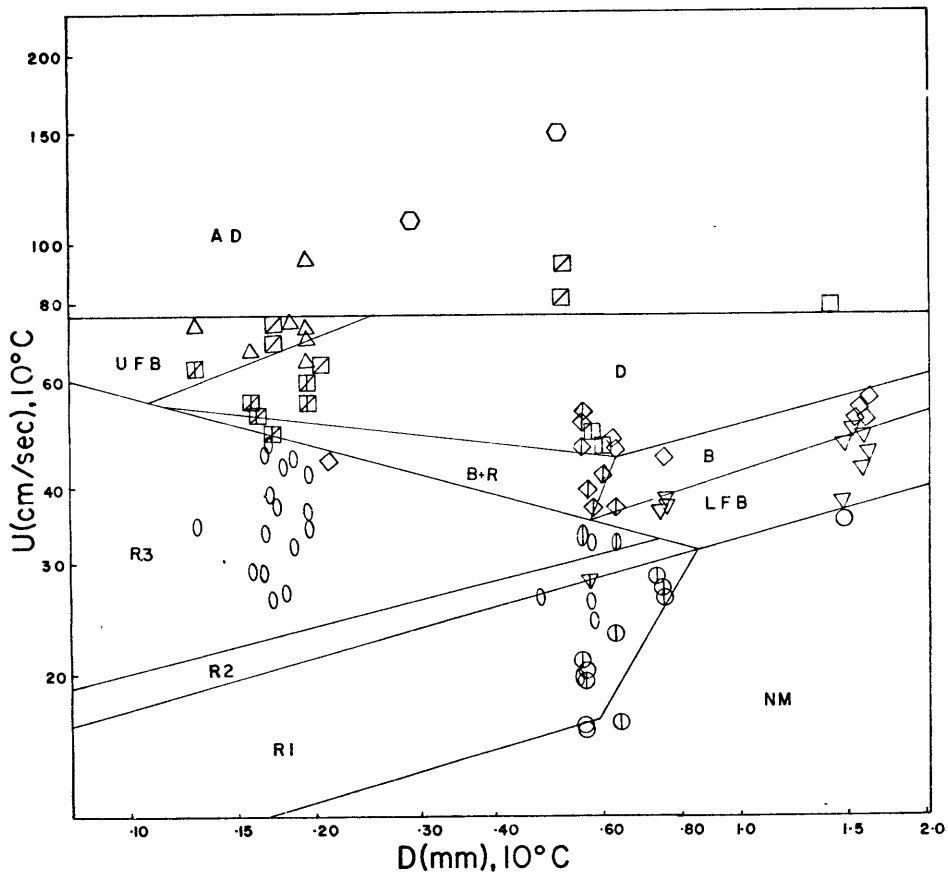

Fig. 3.1. Velocity-size diagram for 8.5 cm flow depth.

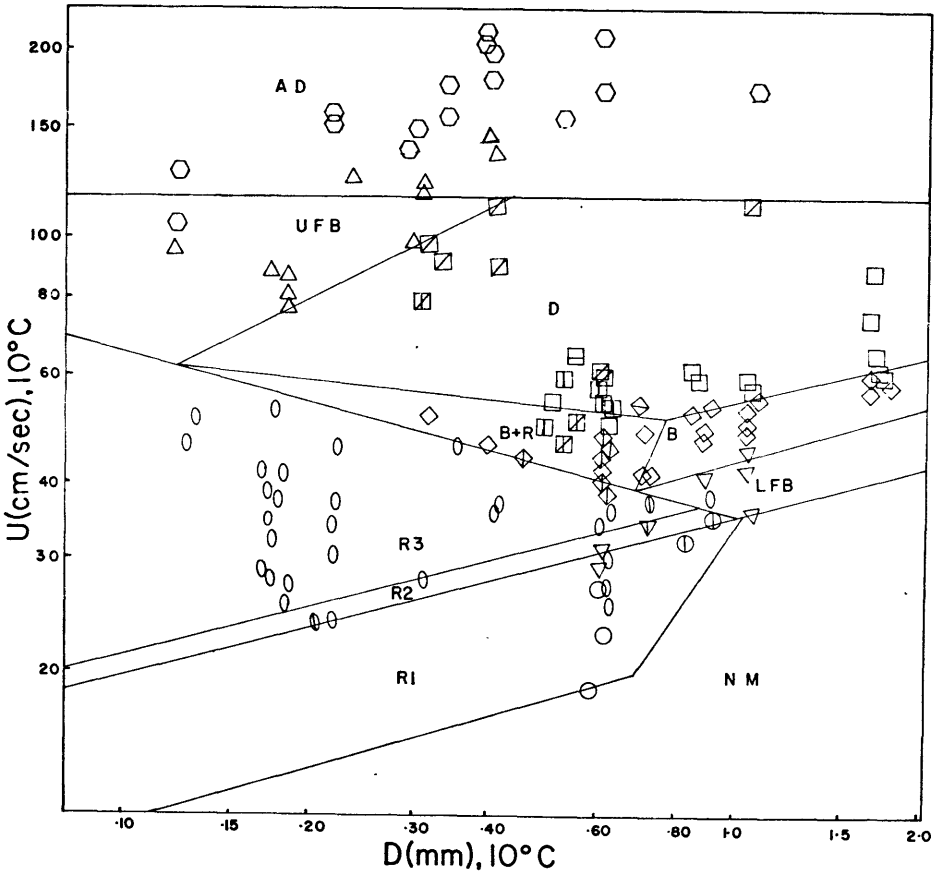

Fig. 3.2. Velocity-size diagram for 20 cm flow depth.

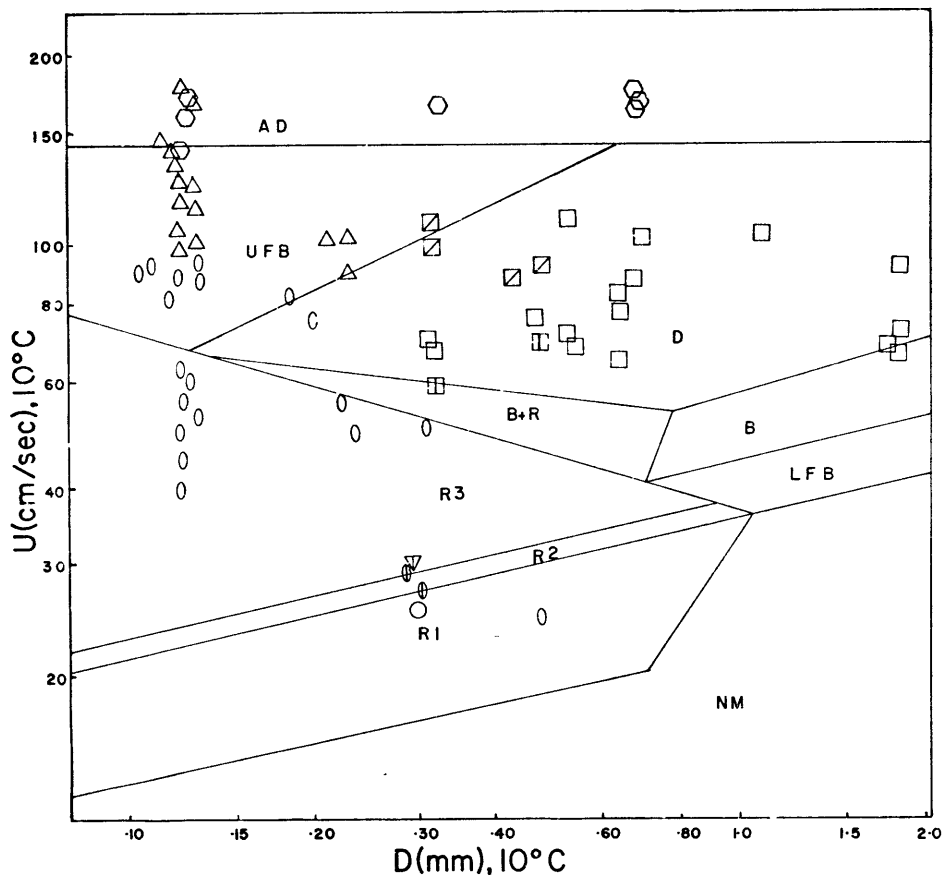

Fig. 3.3. Velocity-size diagram for 30 cm flow depth.

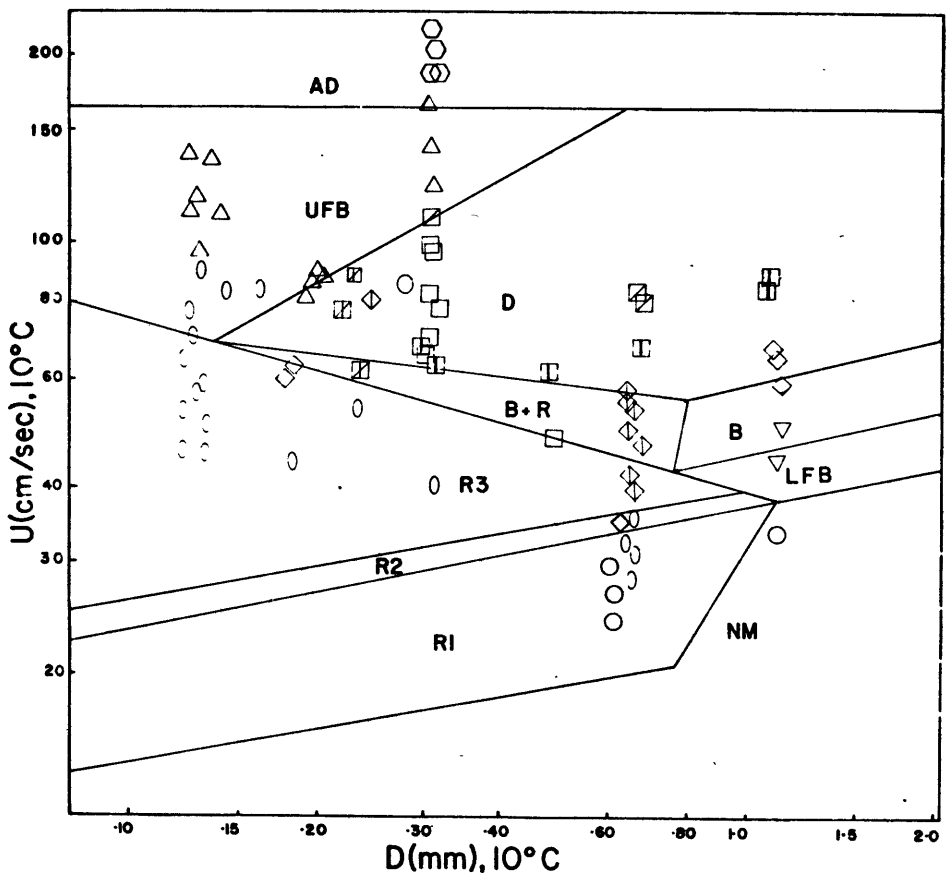

Fig. 3.4. Velocity-size diagram for 40 cm flow depth.

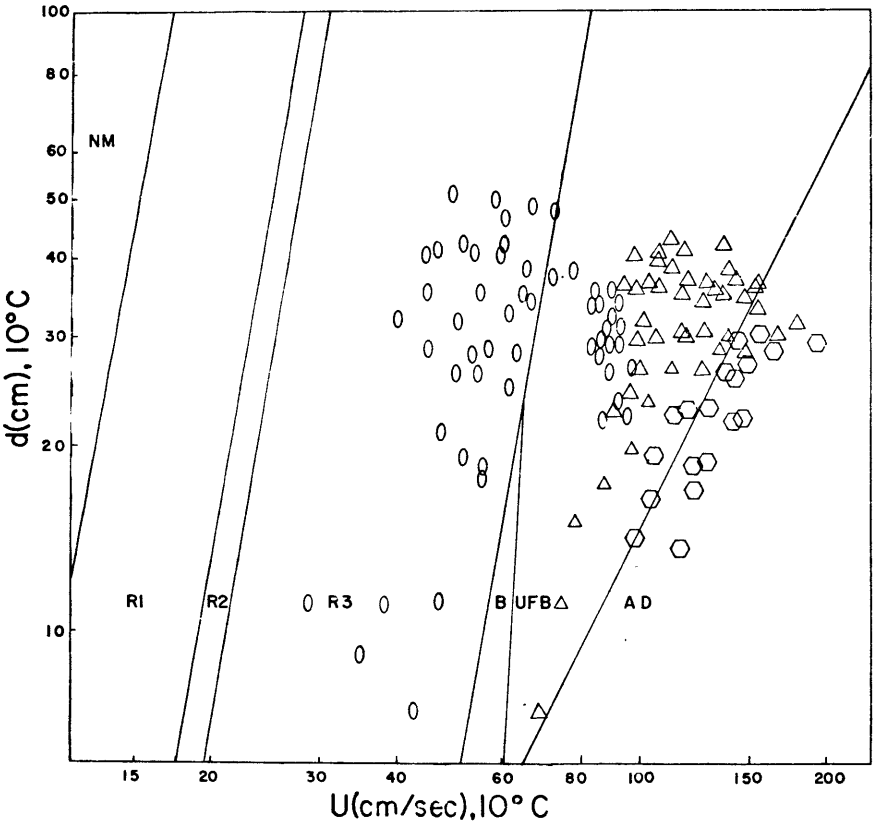

Fig. 3.5. Depth-velocity diagram for 0.13 mm sand size.

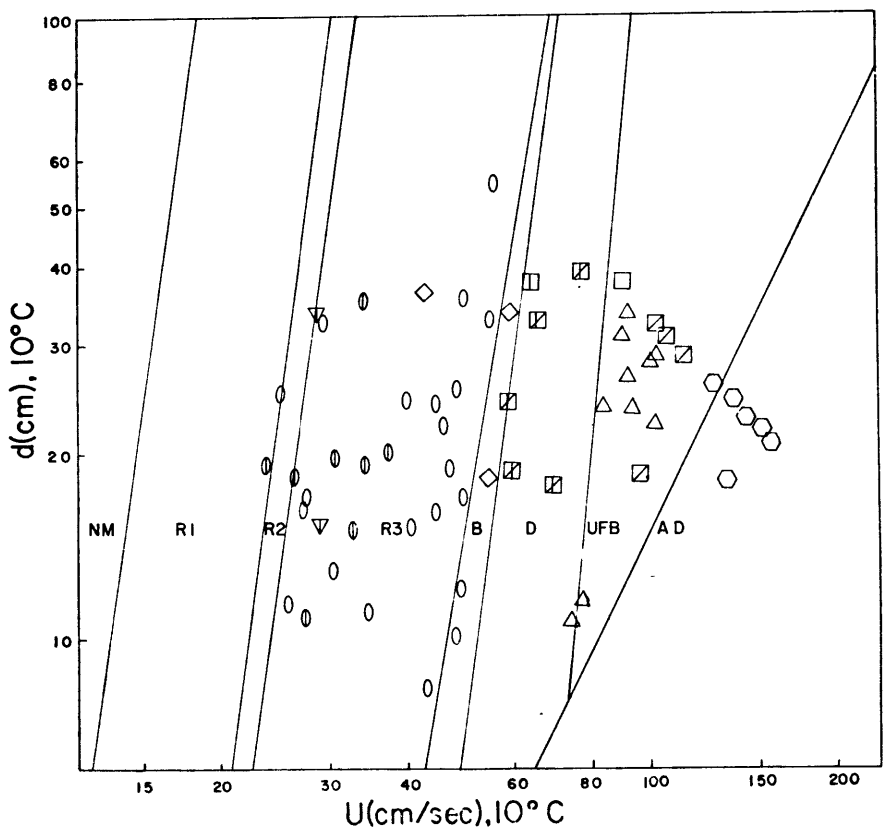

Fig. 3.6. Depth-velocity diagram for 0.22 mm sand size.

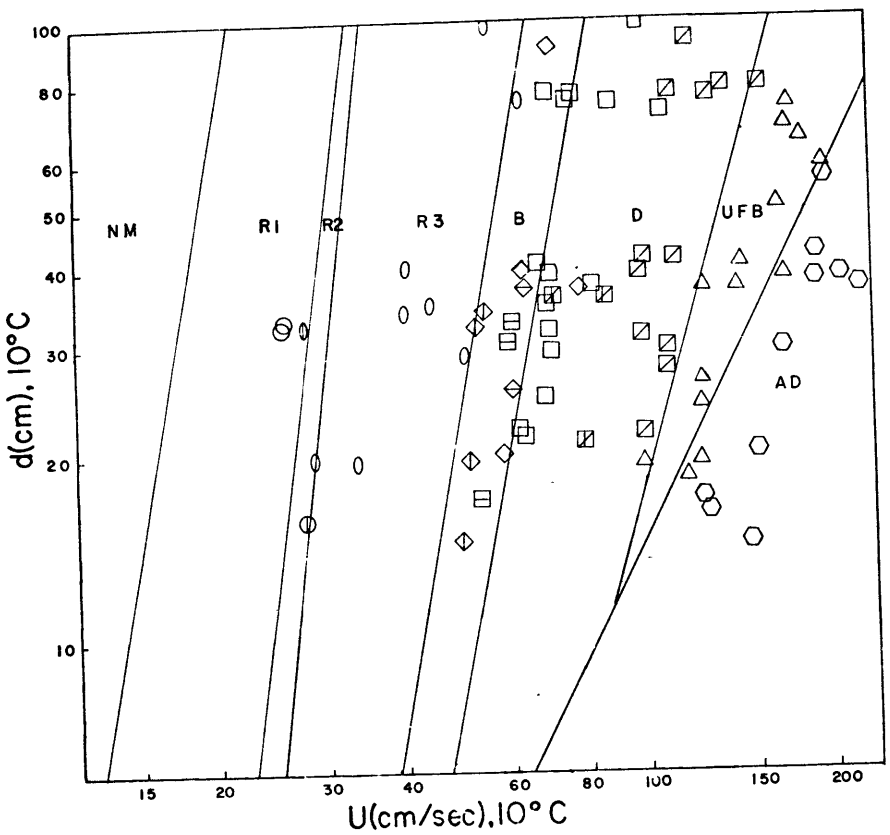

Fig. 3.7. Depth-velocity diagram for 0.31 mm sand size.

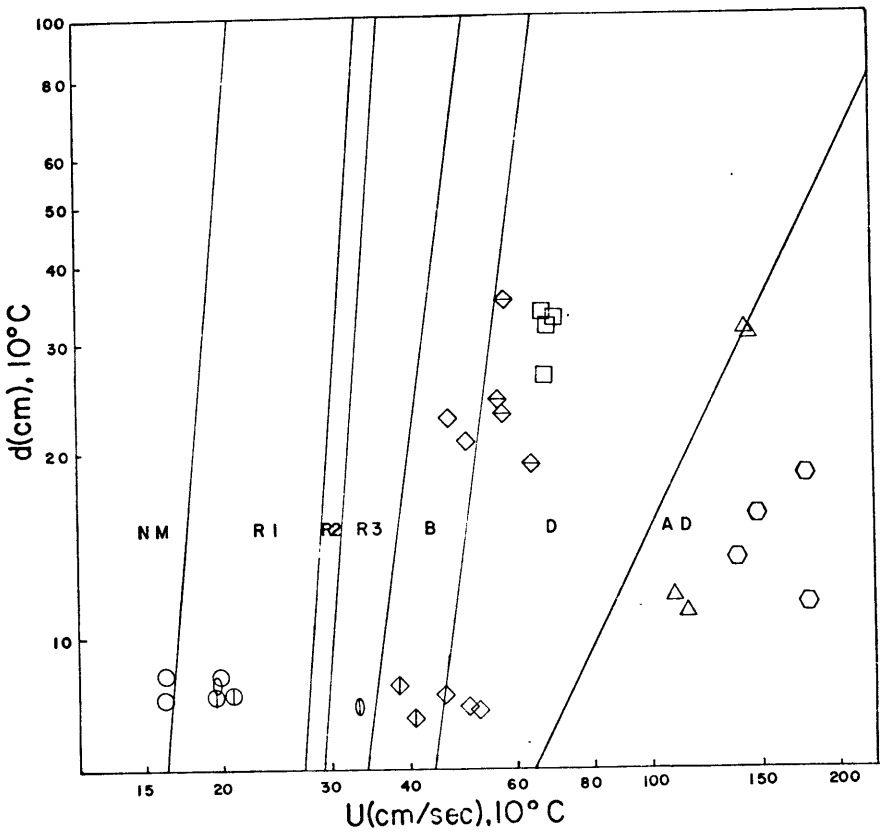

Fig. 3.8. Depth-velocity diagram for 0.55 mm sand size.

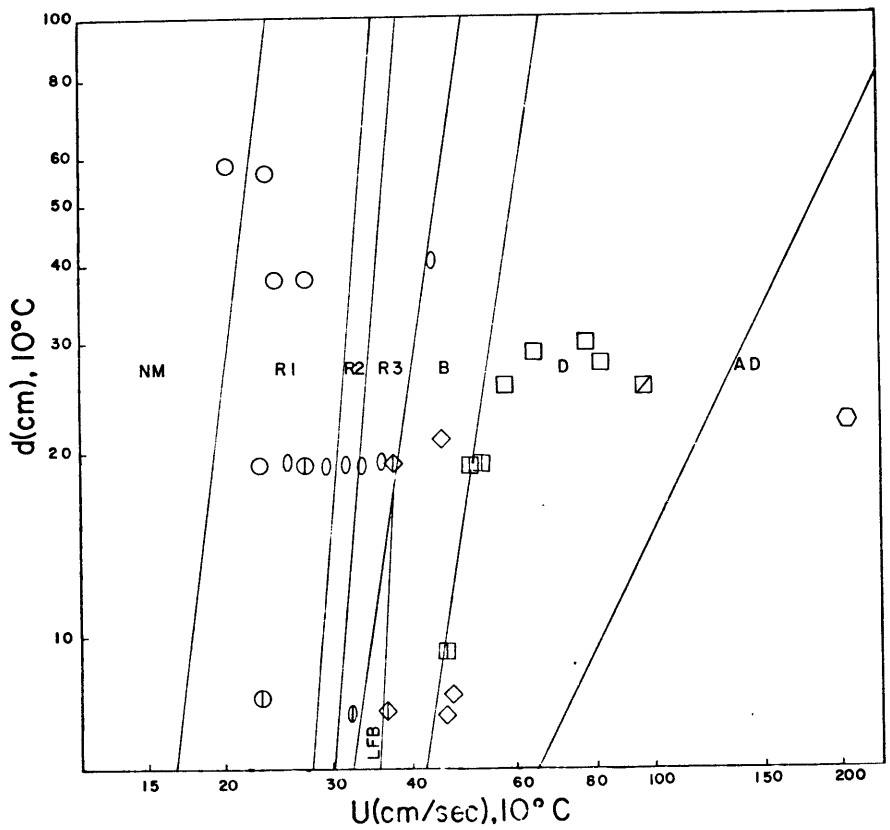

Fig. 3.9. Depth-velocity diagram for 0.62 mm sand size.

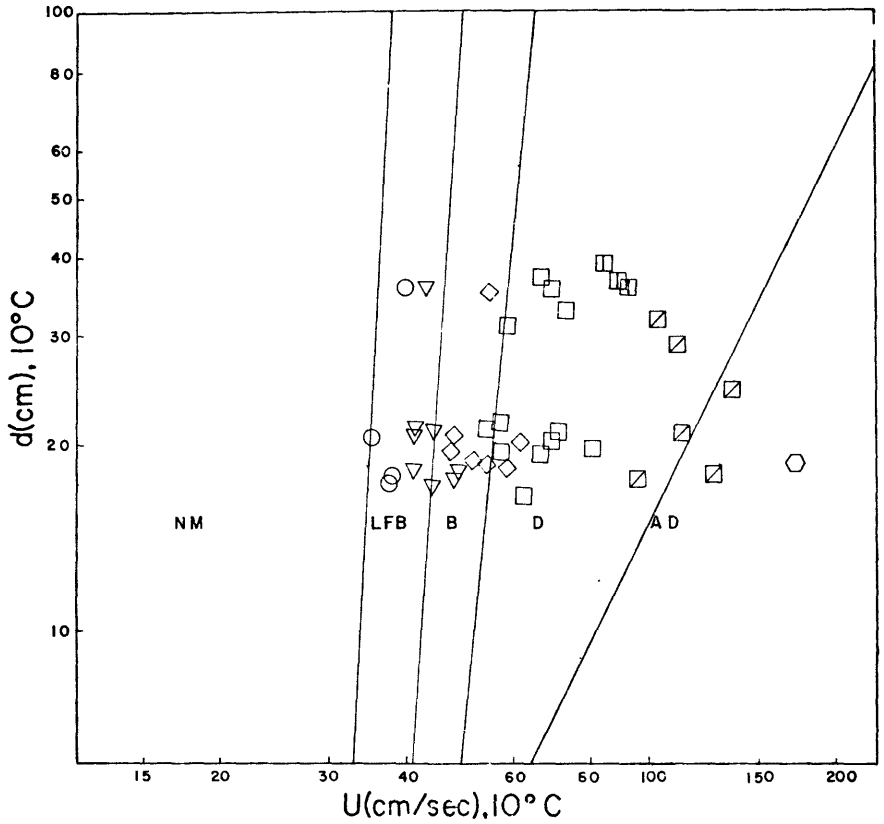

Fig. 3.10. Depth-velocity diagram for 1.07 mm sand size.

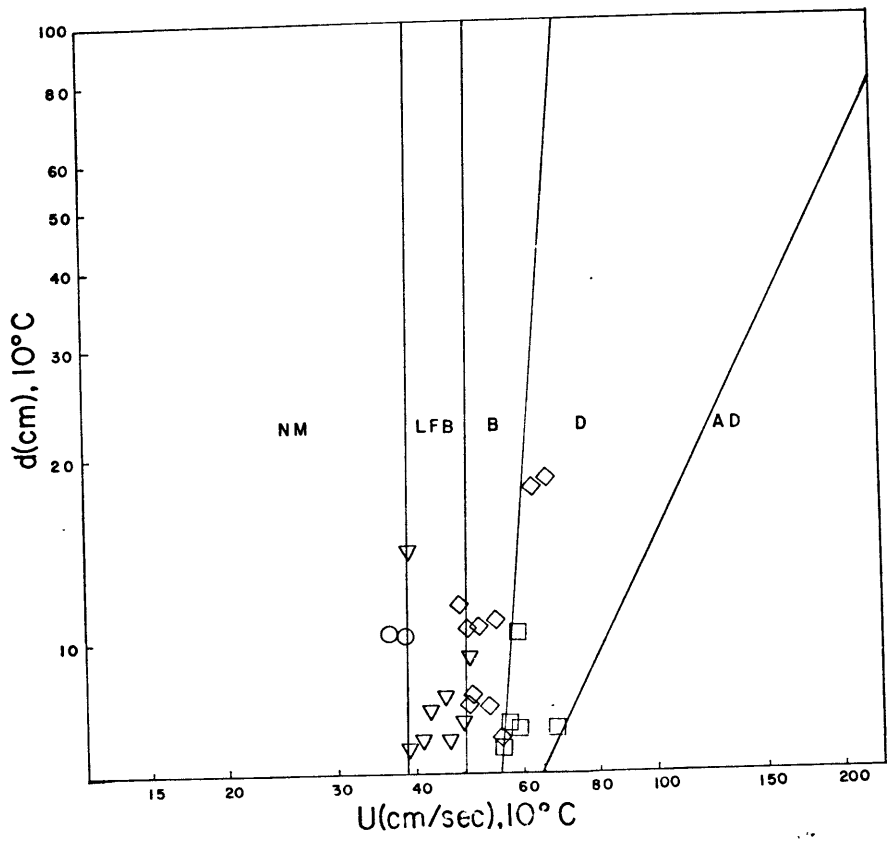

Fig. 3.11. Depth-velocity diagram for 1.60 mm sand size.

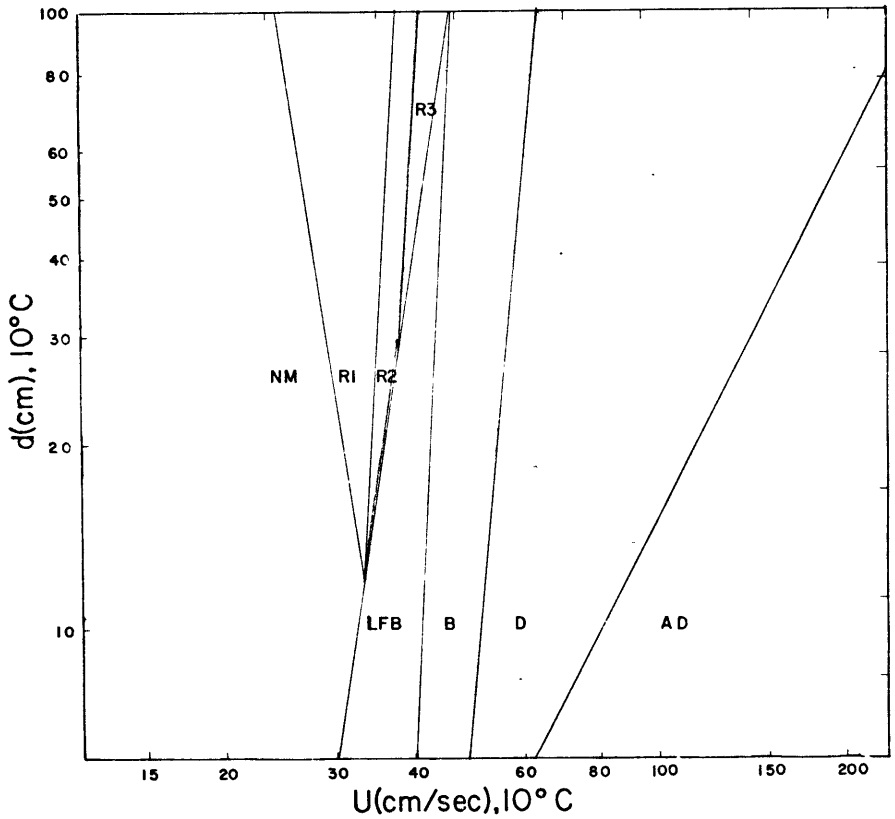

Fig. 3.12. Depth-velocity diagram for 0.90 mm sand size.

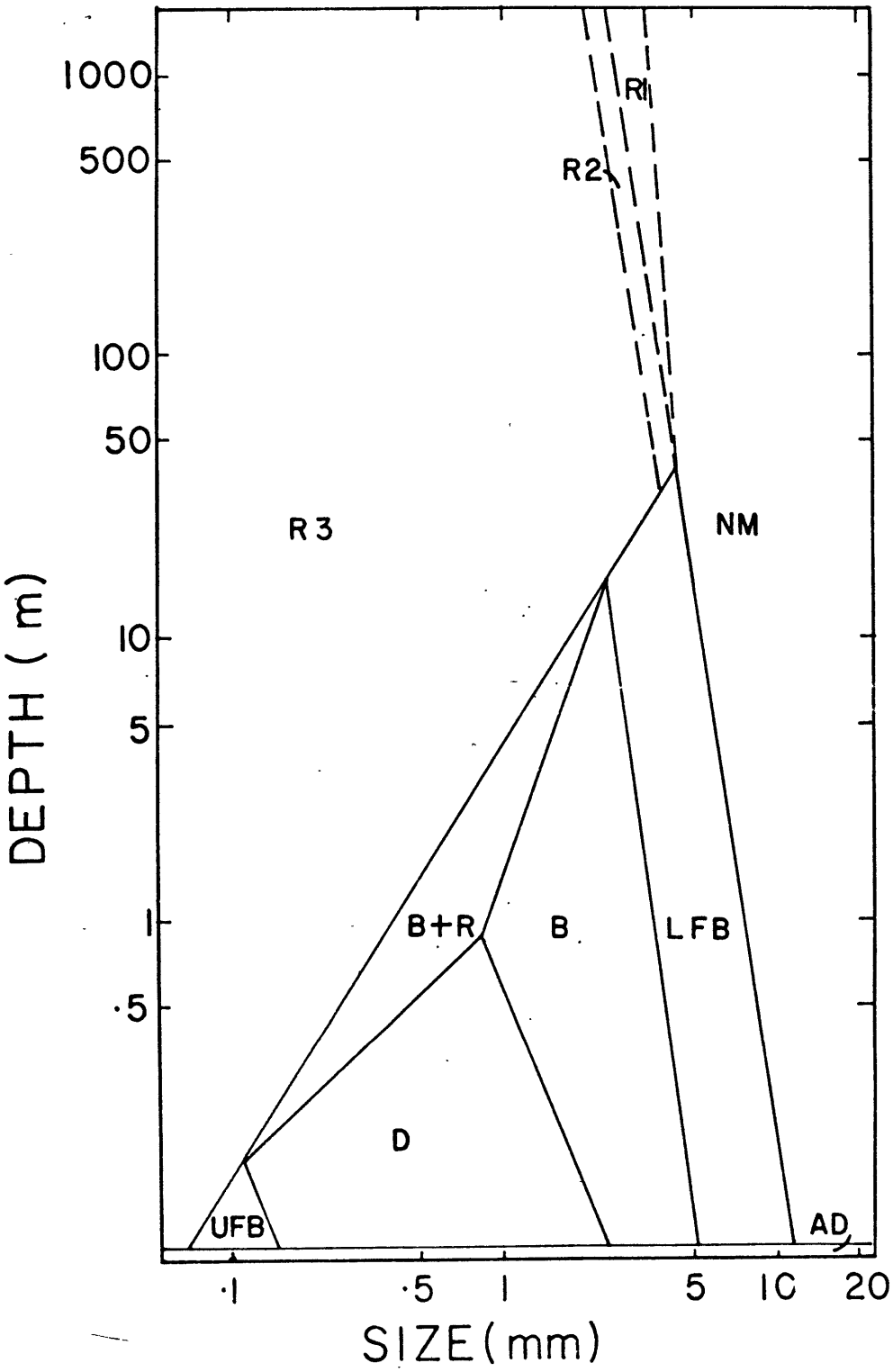

Fig. 3.13. Depth-size diagram for 60 cm/sec flow velocity (not to same scale as other projections).

LEGEND

Bed State	Symbol, data point	Symbol, stability field
No movement	○	NM
Ripples (in combination with other bed forms)	|	—
No movement (metastable) /ripples	◐	R1
Lower flat bed	▽	LFB
Lower flat bed (meta-stable)/ripples	▽	R2
Ripples (no other bed form designated)	⬯	R1, 2 or 3
Ripples initiated	⬮	R3
Bars	◇	B
Bars + ripples	◇	B or B+R
Bars + dunes	◇	B
Dunes (no other bed form designated)	□	D
Dunes + ripples	▥	D
Dunes (flat-backed) + ripples	▨	D
Flattened dunes	⧄	D
Upper flat bed	△	UFB
Antidunes	⬡	AD

Fig. 3.14. Legend for Figs. 3.1-3.12 and 4.5 (fold out for reference).

of the interval over which the first projection was plotted, the same for every boundary-intersection of that projection.

Ideally, boundaries in a three-dimensional array of points could be fitted by computer, but there was too much in-process subjectivity and interpretation of the data during this initial round of boundary delineation for this to be practical. Now that these diagrams have been constructed, however, computerization of boundary positions and of all data (regardless of interval) would permit rapid plotting of various projections and visualization of any orientation of the depth-velocity-size diagram. Since Figs. 3.1-3.12 are drawn to the same scale (all projections in this study are to the same scale, except for Fig. 3.13), an easier and equally effective way to visualize the depth-velocity-size diagram in three dimensions is to manually stack these projections, reproduced onto clear acetate, into a three-dimensional grid.

DISCUSSION

Relations of bed-phase stability fields.

From the normalization of data and three-dimensional interpolation of boundaries emerges a synthesis of data from which relations among various bed-phase stability fields can be described. These relations are described in order to establish a quantitative, empirical basis on which to build an understanding of the forces acting within a sediment transport system and of the effects of varying the fundamental conditions on that system. Experimental confirmation of

certain of these relations is discussed in Part IV.

The following field relations can be observed in any of the velocity-size projections, Figs. 3.1-3.4. As already described, boundaries about the metastable no-movement and metastable lower-flat-bed fields were drawn parallel to one another (also parallel in depth-velocity diagrams, Figs. 3.5-3.9 and 3.12). Following the interpretation of Southard and Boguchwal (1973), these fields pinch out at the same "point" (e.g., center of Fig. 3.1), so that ripples are not stable at sand sizes coarser than that size. With decreasing sand size, the lower-flat-bed stability field pinches out against the ripple stability fields so that there is a size interval in which both ripples or lower flat bed could be stable, depending on the velocity (Southard and Boguchwal, 1973). The upper bound of the highest-velocity ripple field, for which ripples can be initiated from a flat bed, is a linear boundary (e.g., middle of Fig. 3.1). The boundary separating this field from the stability field for bars was extended linearly in both directions: to the lower right, separating ripples from lower flat bed (after Costello, 1974) and to the upper left, through data points for which ripples were poorly distinguished from bars, separating ripples from upper flat bed in fine sand sizes. Where the boundary separating the lower-flat-bed and bar fields intersects this boundary is a "triple point," near which the configuration is probably modified by properties of all three conjoining fields.

Bed forms in fine sands homologous to and occurring at conditions similar to bars observed by Costello (1974) in coarse sands were identified as bars. The V-shaped bar stability field was subdivided by a boundary extending upward from the "triple point" to the concave apex of the bar field (e.g., center of Fig. 3.1), separating a field for bars and ripples on the left from a field for bars only on the right. It was considered that the two fields sloped in opposite senses due somehow to the effects of the presence or absence of ripples on the bed; this boundary drawn in any way but the one stated above would be inconsistent with this observation.

Different subfields for the dune phase could not be delineated in the diagrams due to insufficient data; but from the general distribution of points, it seems that the percentage of the bed covered by ripples decreases with increasing velocity. Also, points for the transition bed phase of Guy et al. (1966) and the flattened dunes of Pratt did plot in proximity to each other, at the uppermost velocities of the dune field (e.g., the upper center of Fig. 3.2). The boundary separating the dune and upper-flat-bed stability fields is linear, terminating against the boundary for antidunes (e.g., upper left of Fig. 3.1). The pinch-out of the dune and bar fields with decreasing sand size was depicted by the positively sloping dune/upper flat bed boundary terminating against the negatively-sloping ripple/bar boundary (e.g., left center of Fig. 3.1), the bar/dune boundary also

terminating at the same "point." This "quadruple point," which actually represents the junction of ripple, bar, dune, and upper flat bed stability fields, is a narrow zone as opposed to at a well-defined point. In this zone, the geometry of bars and dunes probably becomes similar, hence the "sand waves" of Vanoni and Brooks (1957) and Barton and Lin (1955).

The boundary separating the antidune stability field from other bed-phase stability fields was drawn in projections only according to Kennedy's (1963) proposal that antidunes occur for Froude numbers greater than 0.83, except for Fig. 3.2, whose antidune boundary was drawn only according to the distribution of data points. This criterion was in only fair agreement with the plotted data. Thus, it is likely that some effect of grain size on the placement of these boundaries will become evident with the acquisition of new data.

With increasing mean flow depth, boundaries in velocity-size diagrams tend to move collectively upward and to the right. The configuration of boundaries with varying depth remains similar but not exactly constant (cf. Fig. 3.1 to 3.2 and 3.3). This trend can be inferred from the positively sloping boundaries in depth-velocity diagrams.

The above trend can be used to infer pinch-outs of stability fields in depth-velocity and depth-size diagrams, perhaps the most interesting features in these latter two projections. Features of the depth-velocity diagrams, Figs. 3.5-3.12, are discussed below.

In projections for 0.55 mm and 0.62 mm (center of Figs.

3.8 and 3.9), the lower-flat-bed stability field is seen to pinch out with increasing depth against the boundary between the ripple and bar fields; that boundary is collinear with the boundary between the ripple and lower-flat-bed fields, as it is for the velocity-size diagrams. No ripple fields are evident for the relatively shallow depths plotted in either the 1.07 mm or 1.59 mm depth-velocity diagrams (Figs. 3.10 and 3.11). Figure 3.12, a depth-velocity diagram for 0.90 mm, was constructed to show the pinch-out of ripple and lower-flat-bed stability fields in one diagram. In this diagram, the ripple field pinches out with decreasing depth, while the lower-flat-bed field pinches out with increasing flow depth (center of figure). Both pinch-outs are against a linear extension of the ripple/bar boundary. These relationships can be conceived by focusing at a medium grain size in a velocity-size diagram and shifting that diagram upward to the right to simulate increasing flow depth.

The boundary between the dune and upper-flat-bed stability fields in Figs. 3.5-3.7 is linear and terminates against the antidune boundary (lower right of figures). No field for upper flat bed is observed in the depth-velocity diagrams for the coarser sand sizes (Figs. 3.8-3.12), but it could pinch out against the antidune boundary with decreasing flow depth at depths deeper than those plotted (e.g., Fig. 3.7).

A depth-size diagram was constructed (Fig. 3.13) by three-dimensional interpolation of boundaries, in order to visualize the relationships of stability fields in the depth-

size plane. This diagram is not drawn to the same scale as others because of the broad range of depths and sand sizes plotted. A constant velocity U = 60 cm/sec was chosen so that the sequence bars/dunes/bars with increasing sand size could be documented.

The dune field (Fig. 3.13) pinches out with increasing depth and is bounded on two sides by a bar field: by the ripple plus bar field on the left and by the bar (only) field on the right. The boundary separating the bar fields from one another (center of figure) was drawn from the vertex of the dune field to the vertex of the bar fields, as was done in velocity-size diagrams, where the latter vertex is actually the "triple point" referred to above. The boundary separating the ripple and bar fields (left of figure) is extended linearly in both directions as the ripple/upper flat bed boundary to the lower left and the ripple/lower flat bed boundary to the upper right. With increasing flow depth, the bar fields pinch out (at the "triple point"); with decreasing flow depth the ripple plus bar stability field pinches out against the ripple/bar boundary. Since the point of the latter pinch-out represents the "quadruple point" in velocity-size diagrams, the dune and upper flat bed fields must also pinch out at the same point, giving the dune field a diamond shape in the center of the figure and restricting the upper-flat-bed stability field to the lower left corner of the figure. This point represents those conditions of depth and sand size for which the "quadruple point" occurs for U = 60

cm/sec.

The extent and position of the fields for metastable ripples and metastable lower flat bed were drawn schematically (upper center of figure) due to insufficient information for such great flow depths. Boundaries about these fields were drawn parallel, as they were in other projections. The slope of these boundaries was drawn according to the general observation that boundaries in velocity-size diagrams sloped oppositely to their analogues in the depth-size diagram.

At the shallowest depths, only antidunes are stable (base of figure), while at very deep depths, only ripples, no movement, or metastable lower flat bed are stable. The greatest complexity in this diagram is concentrated in an intermediate range of depths attainable in scale-model studies. Finally, the depth-size diagram tends to shift upward and somewhat to the right with increasing velocity.

Temperature effects.

Because the depth-velocity-size diagram constructed for this study is implicitly dimensionless, it depicts changes in the bed configuration for variations not only in mean flow depth, mean flow velocity, and median sediment size, but also in fluid density, fluid viscosity, and gravitational acceleration (and, to a limited extent, sediment density), which are variables contained in the nondimensionalizing coefficients of the parameters of the diagram. This discussion

emphasizes the effects of a change in water temperature, where fluctuations in water temperature characterize variations in both fluid density and fluid viscosity.

Temperature effects on sediment transport have been studied by Straub et al. (1958), Franco (1968), Hill et al. (1969), Taylor and Vanoni (1972, 1972), and Taylor (1974). Generally, their procedure was, for different sets of constant conditions, to measure sediment discharge on a flat bed while varying water temperature, in order to document the variation of sediment discharge with temperature. One can infer from the results of the present study a correlation more complex than a simple plot of temperature versus sediment discharge.

As discussed earlier, the only plot of trends of a dependent variable for which a correlation between all the determinants of a configuration and the bed phase or dependent variable can be visualized and, further, for which that correlation can be expressed dimensionally is one within the framework of the depth-velocity-size diagram. However, because data plotted in the depth-velocity-size diagram must be at a standard temperature, the change in sediment discharge, or any other dependent variable, with a fluctuation in temperature must be determined in the following way. First, convert the depth, velocity, and size of the initial bed state to their dynamic equivalents at the standard temperature 10°C and the same observed depth, velocity, and size for the bed state at the final temperature to their dynamic equivalents at 10°C; next, plot those equivalents in a depth-

velocity-size diagram contoured for the dependent variable in question. The effects of a temperature change on the effects of the independent variables are depicted in the constant-temperature diagram by the change from the first to the second point in the dependent variable and/or bed phase. After that change has been specified, independent and dependent variables can be scaled to their dynamic equivalents at the final temperature. Thus, the effect of a temperature change on the observed configuration is determined analytically by the net effect of a change at constant temperature in the dependent variables and the scaling of those variables to their values observed at the final temperature.

In the depth-velocity-size diagram, the change characterized by the relative positions of points for the initial and final bed state depends not only on the sense and magnitude of the temperature change, but also on the initial conditions. A vector from the point for the initial state to the point for the final state could cross boundaries separating stability fields, describing a qualitatively distinct change in the observed configuration (cf. U.S. Army Corps of Engineers, 1969; Hill et al., 1969; Taylor, 1974) as well as a possible abrupt change in the variation of the dependent variable (cf. contoured diagrams in Part IV). Furthermore, depending on the position of the vector in the diagram, the values of the contours crossing the vector could either increase or decrease, or both, and the relative values of the contours on the end points of that vector could show a net increase or net decrease. The observed

net effect, therefore, could be an increase or decrease in the dependent variable, depending jointly on the relative change noted in the depth-velocity-size diagram and the relative magnitude and sense of the subsequent scaling, relative to that change (illustrated below). This explains why, in the studies cited above, some cases of an increase in sediment discharge and some cases of a decrease in sediment discharge were documented for a change in temperature.

Looking back, the essential difference in approach taken by those earlier temperature studies and this study seems to have been the recognition that temperature does not act independently but acts in conjunction with other independent variables to effect a change in the configuration. Furthermore, this approach is broader in scope and more comprehensive in its analysis, since it is not restricted to a particular configuration or temperature change. The quantitative procedure for which the effect of temperature on the observed configuration is determined, including the relative change, the actual difference, and the actual final state, is described below.

For a temperature change from T_A to T_B, if a_{10} and b_{10} are, respectively, contours of the depth-velocity-size diagram for the initial and final states, a and b the respective values of the dependent variable at T_A and T_B, and R_A and R_B the appropriate scale ratios relative to a prototype of 10°C for the dependent variable of each end state, then the actual values of the dependent variable for the initial and final

state are:

$$a = \frac{a_{10}}{R_A} \tag{3.3}$$

$$b = \frac{b_{10}}{R_B} \tag{3.4}$$

The absolute change in the dependent variable for a temperature change from T_A to T_B is:

$$b - a = \left(\frac{b_{10}}{R_B}\right) - \left(\frac{a_{10}}{R_A}\right) \tag{3.5}$$

Finally, the relative change in the dependent variable can be expressed as:

$$\frac{b}{a} = \left(\frac{b_{10}}{a_{10}}\right) \cdot \left(\frac{R_A}{R_B}\right) \tag{3.6}$$

In Eq (3.6) the second factor on the right can be simplified since each R is relative to the same prototype and so possesses the same numerator. That quantity can be replaced by $R_{B \text{ to } A}$, the appropriate scale ratio between B and A, where B represents the prototype in the numerator; thus, the relative change is:

$$\frac{b}{a} = \left(\frac{b_{10}}{a_{10}}\right) R_{B \text{ to } A} \tag{3.7}$$

Eq (3.7) illustrates the generally competitive nature of the two effects constituting the net effect of a temperature change, the change in the dependent variable versus the scaling of the dependent variable.

The determination of a and b in Eqs (3.3) and (3.4) expresses the same principle of dynamic similitude as Eq (3.2),

that corresponding parameters are identical in dynamically similar systems. The effect of a change in gravitational acceleration with other independent variables constant can be determined, based on that same principle, by a procedure similar to the one outlined above for temperature changes. By converting independent conditions to the dimensionless parameters stated in Eq (3.1) (for quartz-density sand), the appropriate point in the depth-velocity-size diagram can be located and the contour associated with that point can be identified. The dimensionless value of that contour can then be converted to the dimensional value observed in the final state.

The effects of a change in sediment density can be only indirectly inferred from a procedure similar to the one above. A significant change in sediment density would have to be accompanied by some change in the water temperature or fluid to maintain the ratio ρ_s/ρ at 2.65, if the depth-velocity-size diagram as constructed for this study is to be used.

Finally, the same procedure outlined in this section can be used to determine the relative effects of a change in one fundamental variable versus a change in another and the effects of joint changes in the fundamental variables (excluding sediment density). All that is required is a properly contoured depth-velocity-size diagram and specification of the final conditions or the initial conditions plus the change in conditions.

PART IV: PILOT STUDY OF HOT-WATER MODELING

OBJECTIVES

Hot-water modeling extends the capabilities of a flume. For example, for the highest scale ratio of 2.3 (based on 80°C water in the model, re tive to 10°C water in the prototype), flume length, channel width, and flow depth are effectively increased by a factor of about two and one-third, flow discharge by a factor of about eight, since

$$Q_r = U_r A_r^2 = l_r^{2.5} \tag{4.1}$$

and flow power by a factor of about three and one-half since

$$\tau_{o_r} U_r \approx U_r^2 \, (U_r) = l_r^{1.5} \tag{4.2}$$

while actual equilibrium and observation times are decreased by a factor of about one and one-half, since

$$t_r = l_r^{0.5} \tag{4.3}$$

Hot-water modeling using a very large flume 1-2 m deep thus can simulate bed configurations in natural environments (cf. Fig. 1.1). Hot-water modeling using a small flume cannot simulate naturally deep depths, but can simulate a larger flume. Therefore, space, water, power, sand, flume-construction materials and time can be used more efficiently and existing flumes can become more flexible tools for research by using hot-water dynamic scale modeling. In order to determine the practicality of hot-water modeling with a flume and a scale

ratio larger than were used for the modeling test, a pilot study was carried out.

Since a very large flume was to be constructed at the Laboratory for Experimental Sedimentology at M.I.T. upon the success of this pilot study, the scope of experiments made during the pilot study was restricted to problems not requiring deep depths. Within this scope are experiments confirming the relative positions of certain bed-phase stability fields in the depth-velocity-size diagram constructed in Part III. Such experiments anticipate the next generation of deep-water flume experiments by consolidating knowledge of bed configurations produced in shallow flows.

Observations of bed configurations made during these experiments were aimed at: 1) determining whether descriptions of equilibrium bed configurations, particularly of bars and dunes, were interpreted in Part III accurately and validly according to bed phase; 2) delineating, generally, the range of conditions for which these bed phases are stable, particularly bar and dune bed phases at fine sand sizes; and 3) verifying the placement of boundaries in the depth-velocity-size diagram by noting the agreement between a velocity-size diagram for 50 cm flow depth constructed by three-dimensional interpolation and a velocity-size plot of data observed at 50 cm flow depth. These points 1 through 3 were incorporated into a survey of bed configurations at fine sand sizes, during which a procedure for hot-water modeling was developed.

PROCEDURE

Flume.

A tilting, closed-circuit, 91.4 cm wide and 11.5 m long, flume was used for the pilot study (Figs. 4.1 and 4.2) which recirculates water and sediment with no free overfall downstream. Scale ratios up to about 2.3 yielded scaled flow depths up to 50 cm, a scaled width up to 2.7 m, a scaled flume length up to 27 m, and width-to-depth ratios up to 5:1. Scaled dimensions of width and depth were roughly equivalent to those of larger flumes, like the one at Colorado State University used by Guy et al. (1966) and Nordin (1976).

The headbox, tailbox, and twin 6" return pipes are made of galvanized steel, while the channel itself is constructed of transparent acrylic plastic. A 30 hp electric motor drives a vertical propeller pump by means of a positive drive gearbelt and sheave coupling, which permitted adjustment of the maximum attainable discharge by varying the size ratio between sheaves of the pump and motor. For this study that ratio was 1.25, for a discharge of about 6 cfs (633 cm^3/sec) and maximum scaled velocities equivalent to those in the upper-flat-bed stability field. Pump horsepower (18 hp) was kept down to levels at which wear on the bearings of the pump shaft, due to hot water, would not be excessive.

Discharge during a run was adjusted by means of gate valves, one to each return line, and a by-pass valve with outlet into the tailbox. The by-pass valve acted both as a

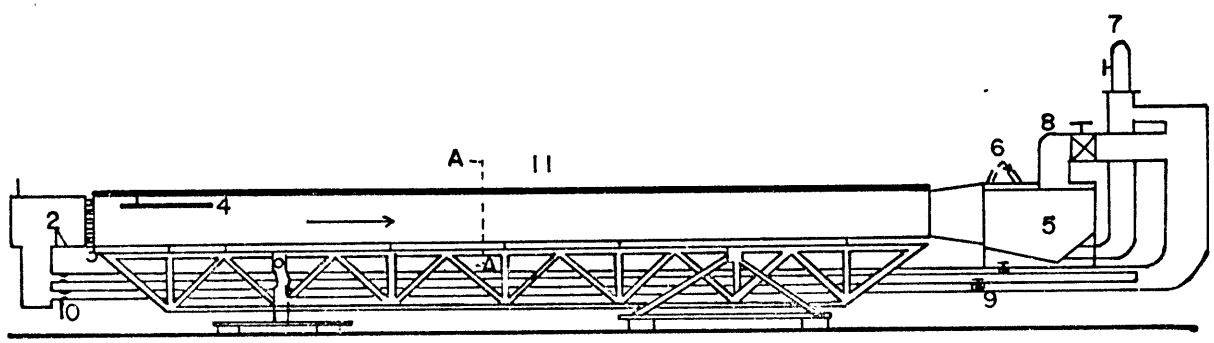

1 HEADBOX
2 WEIR
3 BAFFLE
4 WAVE DAMPER
5 TAILBOX
6 FILTRATION SYSTEM
7 PUMP
8 BYPASS LINE & VALVE
9 RETURN LINES & VALVES
10 VENTURI METERS
11 FLUME COVERS
12 PLEXIGLASS CHANNEL
13 POLYSTYRENE INSULATION
14 STEEL LINER
15 C-CLAMP

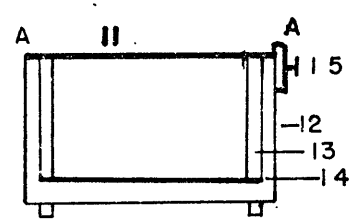

Fig. 4.1. Schematic diagram of 11.5 m flume.

Fig. 4.2. Photograph of 11.5 m flume. Flow from left to right.

control and pressure release valve and was located just upstream of the two other valves. Discharge in each return line was measured by an in-line Venturi meter (D_1 = 15.6 cm, D_2 = 10.2 cm) and monitored from an attached mercury-filled U-tube manometer.

Return pipes entered a chamber below and open to the headbox. Ambient inlet turbulence was adequately damped by a weir 20 cm high wedged into the enclosed headbox and by a Plexiglas baffle with 1.6 cm holes spaced 2.5 cm apart, located just downstream of the weir at the headbox/channel junction. A grid of stacked straws was not used to further smooth out the flow since, for the high velocities used, a weight sufficient to stabilize the grid of stacked straws could not be contained beneath the flume covers. A 90 cm x 1.3 m board, placed downstream of the grid, was positioned to rest on the water surface in order to damp surface waves.

Industrial-strength algicide and rust inhibitor were added to the water to prevent turbidity due to accumulating algae and rust. Acceptable visibility was maintained by a two-step filtration process. Water tapped off the tailbox was run through a conical centrifugal sediment separator, returning to the tailbox all sediment coarser than very fine silt. Water with residual fine silt was then passed by gravity through a 36 cm x 36 cm bat of fiberglass insulation into a settling barrel to remove very fine particles that were likely dead algae, rust, and quartz dust. Part of the filtered water was returned to the system through an overflow

hose from the barrel to the tailbox and part was pumped to the bearings of the main pump shaft as a lubricant. A safety system, consisting of a pressure monitor in the line between the settling barrel and the pump bearings and a solenoid relay to the main control box of the flume, cut off the power if the pump ran dry.

Temperature control.

Four series of runs were made at three scale ratios, approximately 2.3, 1.7, and 1.1, relative to a prototype at 10°C. Turbulence generated by the pump provided sufficient energy input to heat the water. By insulating and covering the system, hot water temperatures up to 80°C, giving a 2.33 scale factor, could be maintained. By running 8°C tap water through three 50 ft coils of 1/2" copper tubing immersed in the tailbox, the system could be cooled down to about 14°C, giving a 1.1 scale factor. Without cooling, insulating, or covering the system, an intermediate temperature of 45°C was attained, accounting for the middle scale ratio above of about 1.7. Other intermediate temperatures and scale factors could have been attained by adjusting the extent of cooling, insulating, and covering of the system. Water temperature was monitored with a thermometer.

In order to protect the channel from high temperatures during the highest-temperature series of runs, sheets of polystyrene bead foam were placed on the inside of the flume. (Sheets of polyurethane were first tested and found to be

unsatisfactory because they were polymerized by heat and warped extensively.) Sheets 2 cm thick were used on the channel sides and sheets 1.25 cm thick on the channel bottom, where the sand bed itself was an additional layer of insulation. Temperature at the outside surface of the sidewall was 36°C when the water temperature inside was 80°C.

The primary expense incurred for flume modification was for sheets of galvanized steel used to prevent the sheets of polystyrene from floating or buckling. The steel sheets had a thickness such that the total weight of each sheet just exceeded the weight of water displaced by the sheets of polystyrene underneath. Bottom sheets of polystyrene and steel were emplaced before the vertical sheets. A series of 1/2" brass screws placed every 20 cm and oriented upward through the bottom sheet of steel acted as rigid posts to keep each pair of vertical sheets from shifting inward. Clips, actually 7 cm sections of aluminum channel, were snapped over tops of the steel and polystyrene sheets and the Plexiglas of the sidewall to hold the tops of the vertical sheets in place.

A Plexiglas viewing window 1.2 m long was built into the downstream quarter of the channel in such a way that its sides were flush with the adjacent vertical steel sheets; seams were sealed to prevent leakage of sand between the window and the sidewall. Cleaning the window was somewhat of a problem, since the channel could be uncovered only momentarily without significant heat loss.

The entire flume, including the tailbox, was covered to keep the temperature of the system constant and to contain the warm, humid air that overlay the 80°C water. As a result, humidity in the laboratory during 80°C runs was actually less than humidity from an uncovered flume operating at 25°C. Covers were constructed by attaching a frame to a 4 ft x 8 ft piece of plywood and laying bats of R-3 fiberglass insulation over the top of each cover. The bottom of each cover was wrapped with polyethylene film. A watertight seal between the covers and the sidewalls upon which they rested was formed by stapling strips of closed-cell polyurethane foam to the bottom of each cover and compressing the covers onto the sidewalls using a C-clamp assembly. Foam strips were also placed across the width of each cover where it would abut the adjacent cover.

A horizontal viewing window 1.2 m long was placed over the flow at the same station as the vertical viewing window. It was set onto the water surface in order that condensation on its undersurface would not obscure observation. Vertical sections of Plexiglas sealed the gap between the flume covers and the horizontal viewing window below.

Both return pipes were individually wrapped with fiberglass insulation. Fiberglass insulation was also carefully fitted and draped over all surfaces of the headbox, tailbox, pump, and settling barrell to eliminate exposed surfaces where heat transfer by convection could occur.

Measurement and error of depth and velocity.

Since the arrangement of temperature controls was constant among runs of a series, the heat balance and so the scale ratio varied somewhat among runs of each series as the velocity varied. The scaled mean flow depth, about 50 cm for most runs of the pilot study, was set by adjusting the actual mean flow depth as the bed came to equilibrium according to the scale ratio of each run. However, in the series of runs made at the highest water temperatures, the actual flow depth was restricted by the height of the fixed horizonatal window; the scaled flow depth, then, was approximately set by fixing the window at a height according to the anticipated average scale ratio of all runs of that series.

Actual mean flow depth was calculated from the average of depths measured about halfway up the stoss slope of those bed forms occurring in the downstream third of the channel or, for runs of the high-temperature series, in the field of view of the vertical viewing window. For all runs, depth changes due to evaporation were monitored with a ruler fixed to the sidewall; appropriate volumes of water were added at intervals of about three hours.

In a previous experiment (Boguchwal, 1972), it was found that the difference between measuring depth by the above method at the sidewall and by a center-line longitudinal profile with a point gage amounted to a standard deviation of ±7%, or 7.0 cm ± 0.5 cm, for 24 configurations,

including ripples, lower flat bed, and bars. That error in the depth measurement is acceptable because it is approximately equal to the interval of depth allowed for points plotted in one velocity-size diagram (50.0 cm ± 3.5 cm for the pilot study). However, because the mean flow velocity was calculated from measurements of discharge and mean flow depth, the error in the mean flow velocity was also ±7%. That error cannot be overlooked, since placement of boundaries tends to be most sensitive to mean flow velocity and since distinction of runs in one series was made according to velocity. For the latter reason, in a later section error bars for velocity are plotted and compared for runs in each series.

Selection of sand.

Bed configurations for four fine-sand sizes were investigated; instead of changing sand for each series of runs, the sediment size was varied by adjusting the water temperature. An actual sand size was selected such that, when its median sediment size was multiplied by scale ratios from 1.0 to 2.33, the range of scaled sand sizes spanned sizes of interest. Also, for a scaled flow depth of 50 cm, the scaled width-to-depth ratio and maximum attainable scaled velocity associated with each scaled sand size of interest had to fulfill the following criteria, respectively: width-to-depth ratios had to be greater than about 7:2 to minimize wall effects and maximize scaled width, and the velocities had to be

sufficient to produce upper flat bed in order to cover the entire range of conditions for dunes. If a particular sand size was of greater interest than other sizes over some range, that sand size was set at or near the top of the range of scaled sand sizes, since the maximum of the two limiting factors above could be attained for a given scaled sand size by using the highest possible scale ratio of 2.33.

A glacial outwash sand from Holliston Sand Company (foundry sand #135) was selected, having an actual median size of 0.11 mm (Fig. 4.3). It was hoped (and later confirmed) that the range of scaled sand sizes 0.11 mm-0.25 mm would span the pinch-out with decreasing sand size of the dune and bar stability fields, as depicted in Figs. 3.1-3.4.

The sand was 95% subrounded, subangular quartz; of the remaining 5%, more than half consisted of biotite and muscovite, the rest being heavy-mineral fraction. Clay and clay-sized particles had been washed out.

A sand of similar source and composition but different median sediment size, 0.15 mm (Fig. 4.3), was used for the first series of runs at the "no-temperature-control" scale ratio of 1.7, during which the mechanical integrity of the flume was tested.

General operating procedure.

Small increments of velocity separated runs of the same series, starting with configurations stable in the middle to upper ripple stability field and ending with upper flat bed,

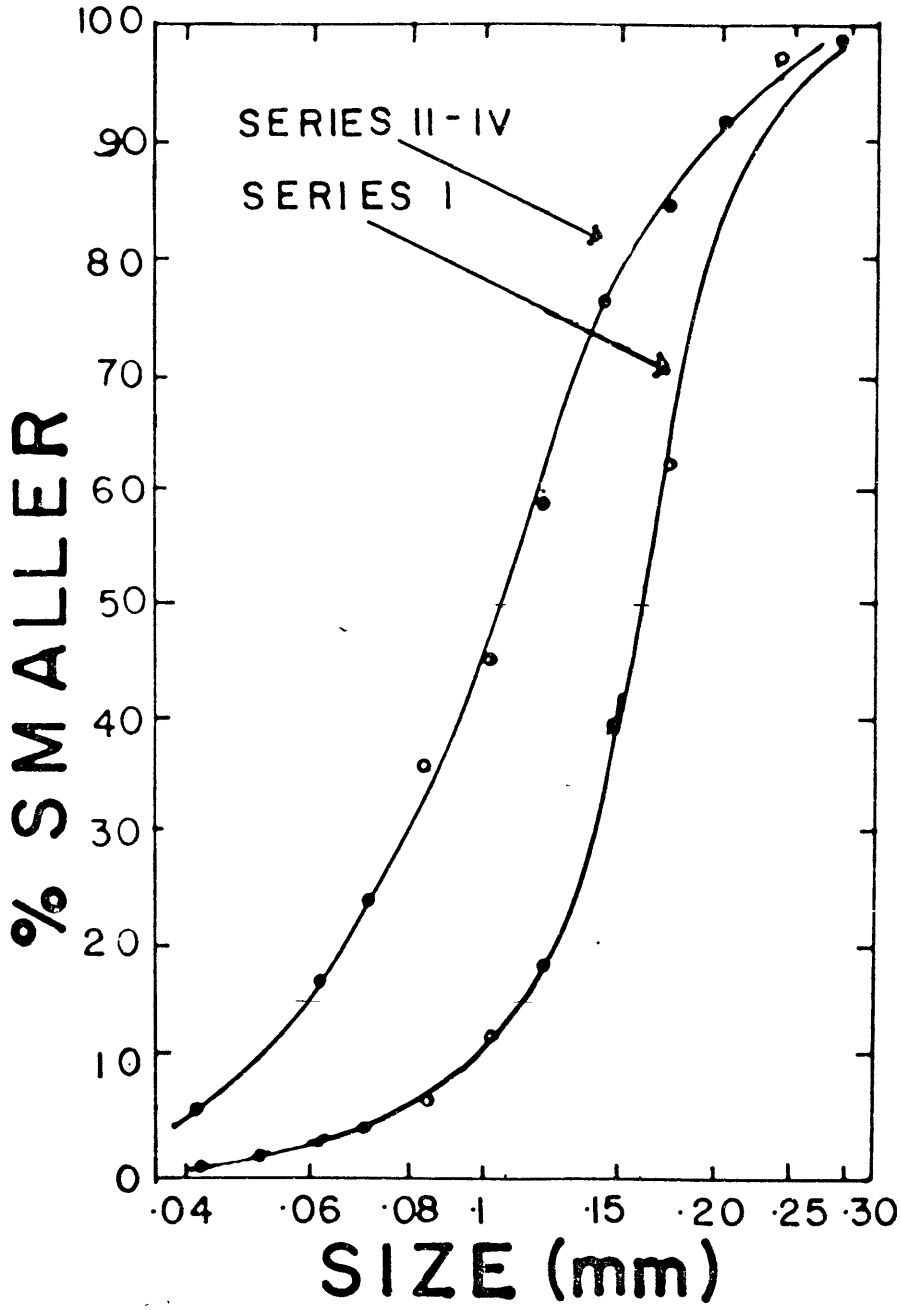

Fig. 4.3. Cumulative frequency curves of sands used for pilot study.

so that the interval of velocity at which bars and dunes are stable was covered. A velocity-size diagram for a flow depth of 50 cm (see Fig. 4.4) was used as a rough guide for determining approximate intervals of velocity for a given sand size.

A flume run was initiated by setting up the appropriate temperature controls and approximately setting the discharge and depth. If the flume had been refilled, one to three days were necessary for the water temperature to equilibrate and for the water turbidity to diminish. The configuration was visually monitored as it reached equilibrium, over a period of about 24 scaled hours for the highest velocity runs and in excess of 36 scaled hours for lower velocity runs; final adjustments to discharge and mean flow depth were made during this time. Observations of the equilibrium configuration were documented over a period of about a day. During that time, the flume was shut off many times in such a way that the bed configuration was not altered, so that, once suspended sediment had settled, the bed could be observed clearly. For runs made at the highest water temperatures, photographs of the bed were taken while the flume was shut off (see next section).

Observations were based on the same properties of the configuration used in Part III to characterize bed phase: the hierarchy of bed forms and the distribution of minor bed forms over the bed. Also documented were the average spacing and height of the dominant and minor bed forms, the average

shape of the mound and trough of the dominant bed form, and the continuity of the crest-line of that bed form.

Longitudinal profiles of the bed configuration were not made during the pilot study chiefly because the temperature drop resulting from shutting off and uncovering the flume would have put a mechanical strain on the seams of the flume where sections of the channel are joined, causing leaks. Two methods are suggested for observing and measuring the bed for future studies using an enclosed hot-water system. One is to use a sonic depth recorder, the more useful of the methods when suspended sediment obscures observation. The other method involves time-lapse cinematography of the bed, necessitating strong lighting and clean viewing windows. With this method, one can record plan and side views of the bed, thereby characterizing the bed in three dimensions, by using an array of three mirrors: one over the channel to pick up the plan view and two at the side of the channel to transmit the side view to the camera.

RESULTS

Presentation and description of data.

A summary of observations for most of the runs appears in Table 4.1. Runs not reported in the summary were for non-equilibrium ripple configurations, made to get an idea of the extent of the ripple stability field. All measurements have been scaled to their equivalent values for 10°C water.

The uncertainty in velocity measurements is plotted for each run in Fig. 4.4. Runs made at the same depth and sand size with significantly overlapping error bars were grouped together if configurations were similar; runs made at the same depth and sand size with significantly overlapping error bars but dissimilar configurations were considered to represent different velocities. In a plot of data onto a velocity-size diagram for 50 cm depth (Fig. 4.5) these error bars approximately span the height of the symbol used for each data point.

Points for Series II (Fig. 4.5) plotted as a group at much lower velocities than were required to fit in with the rest of the data. The reason for this is thought not to be inherent in the data, but an artifact of measurement; namely, a malfunction of the manometer. Flakes of rust were observed in the channel during this series of runs, before rust inhibitor was used to protect exposed steel surfaces. If a flake became lodged in a pressure tap of the Venturi meter, a lower discharge would be registered on the manometer. Because the flume was never drained during Series II and because the same single return line was used for all runs of that series, the error in discharge measurement would be consistent among all runs of Series II. The sequence of configurations and the narrow width of the velocity interval over which bars and dunes were stable were unaffected by the malfunction and were the results central to this study.

Data for Series III were measured at less than 50 cm

TABLE 4.1: Summary of Observations

(Measurements Scaled to 10°C)

Like runs	Run #	T °C	U cm/sec	d cm	D mm	Bed state/ Bed form hierarchy	Dominant Bed Form, Axλ, cm	Remarks
	III-1	14	46	39	0.12	Ripples	1-4x16-19	Linguoid; wavy crests
	III-2	14	53	39	0.12	Ripples	2x15	Broad scoured troughs (27 cm)
	III-3	13	66	29	0.12	Ripples	2x12-20	Cont., wavy crests
	III-7	14	61	19	0.12	Ripples	2-4x14-20	Cont., wavy crests
	III-8	14	63	19	0.12	Ripples	1-2x14-27	Non-continuous crests; broad fan-shaped troughs
{	III-6	14	66	19	0.12	Upper flat bed	--	--
{	III-5	13	66	19	0.12	Upper flat bed	--	--
	III-4	14	68	19	0.12	Upper flat bed	--	--
	II-5	46	40	52	0.19	Ripples	2-4x17	Continuous, wavy crests
	II-4	46	51	52	0.19	Ripples	3-4x26	--
	II-8	45	55	50	0.19	Bars + Dunes	3-4x103	Irregular distribution of forms; some ripples
	II-3	46	60	50	0.19	Dunes	17x200-260	Finned; few ripples at troughs' edge
{	II-10	46	64	52	0.19	Dunes	13-22x150-360	
{	II-9	46	65	51	0.19	Flattened Dunes	13x413	Single crest observed
	II-2	42	68	49	0.18	Upper flat bed	--	--
	II-1	40	77	48	0.17	Upper flat bed	--	--
	IV-27	77	54	48	0.25	Ripples	2-3x17-23	Linguoid; non-continuous crests
	IV-26	77	58	48	0.25	Bars + Ripples	3-4x20	Linguoid ripples, low bars with flat troughs
	IV-25	76	60	47	0.25	Bars + Ripples	6-9x70-100	Intervening, irregular ripples: 2-3x17-30
	IV-24	76	64	47	0.25	Bars + Ripples	4-6x35-70	Non-continuous crests; *en echelon* ripples: 2x12
{	IV-22	73	67	48	0.24	Bars + Dunes	8-11x134	Irregular distribution of forms
{	IV-23	76	68	46	0.25	Bars + Dunes	6-9x100-140	Ill-defined hierarchy
{	IV-8	73	72	47	0.24	Dunes (+ Ripples)	17-22x200-270	Ripples only in trough
{	IV-7	75	73	48	0.25	Dunes (+ Ripples)	11-23x140-200	Ripples at troughs' edge
	IV-9	73	74	47	0.24	Dunes	22-28x270	Straight, regularly-spaced crests
	IV-12	72	79	45	0.24	Dunes	--	Oblique to slightly lobate crests
{	IV-10	74	81	45	0.25	Dunes	23-29x340	Deep troughs
{	IV-11	74	81	46	0.25	Dunes	20-23x275-400	--

TABLE 4.1: Summary of Observations (Continued)

Like runs	Run #	T °C	U cm/sec	d cm	D mm	Bed state/ Bed form hierarchy	Dominant Bed Form, Axλ, cm	Remarks
	IV-13	74	84	46	0.25	Dunes	34-37x410	--
{	IV-15	71	84	47	0.24	Dunes	17x460-520	Cuspate, "horns" rounded into trough
{	IV-14	71	85	45	0.24	Dunes	19-28x400-460	(Few ripples at trough's edge)
	IV-16	71	86	47	0.24	Dunes	13-19x260-460	--
	IV-17	71	88	47	0.24	Flattened Dunes	11-14x660	Observed in pairs, alternating with flat bed
	IV-18	70	92	45	0.24	Flattened Dunes	11-17x>600	Cuspate; long stretches of flat bed
	IV-19	71	95	45	0.24	Flattened Dunes	14-19x>600	Single crest; long trough
	IV-20	70	96	45	0.24	Upper flat bed	--	--
	IV-21	71	99	45	0.24	Upper flat bed	--	--
	I-16	44	50	51	0.28	Ripples	2-3x13-17	Somewhat linguoid
	I-11	47	56	51	0.29	Ripples	1-3x18-26	Crests wavy and ∿ continuous
	I-10	44	59	51	0.28	Bars + Ripples	4-6x100-230	Ripples 1-2x17-25
	I-5	37	64	47	0.26	Bars + Ripples	3x94	Bars irregularly spaced
	I-17	44	64	50	0.28	Bars + Dunes	13x150	Shallow troughs (Ripples: 2x13)
{	I-18	45	66	51	0.29	Dunes (+ Ripples)	13-17x150-200	--
{	I-6	46	68	48	0.29	Dunes	10x150	Straight, continuous crests
	I-2	42	69	49	0.28	Dunes	25x75-100	Continuous crests
	I-7	44	72	50	0.28	Dunes	4-13x150-275	Deep troughs
	I-8	42	74	49	0.28	Flattened Dunes	4x>400	Single crest observed
	I-9	42	78	49	0.28	Flattened Dunes	4x>400	Single crest observed

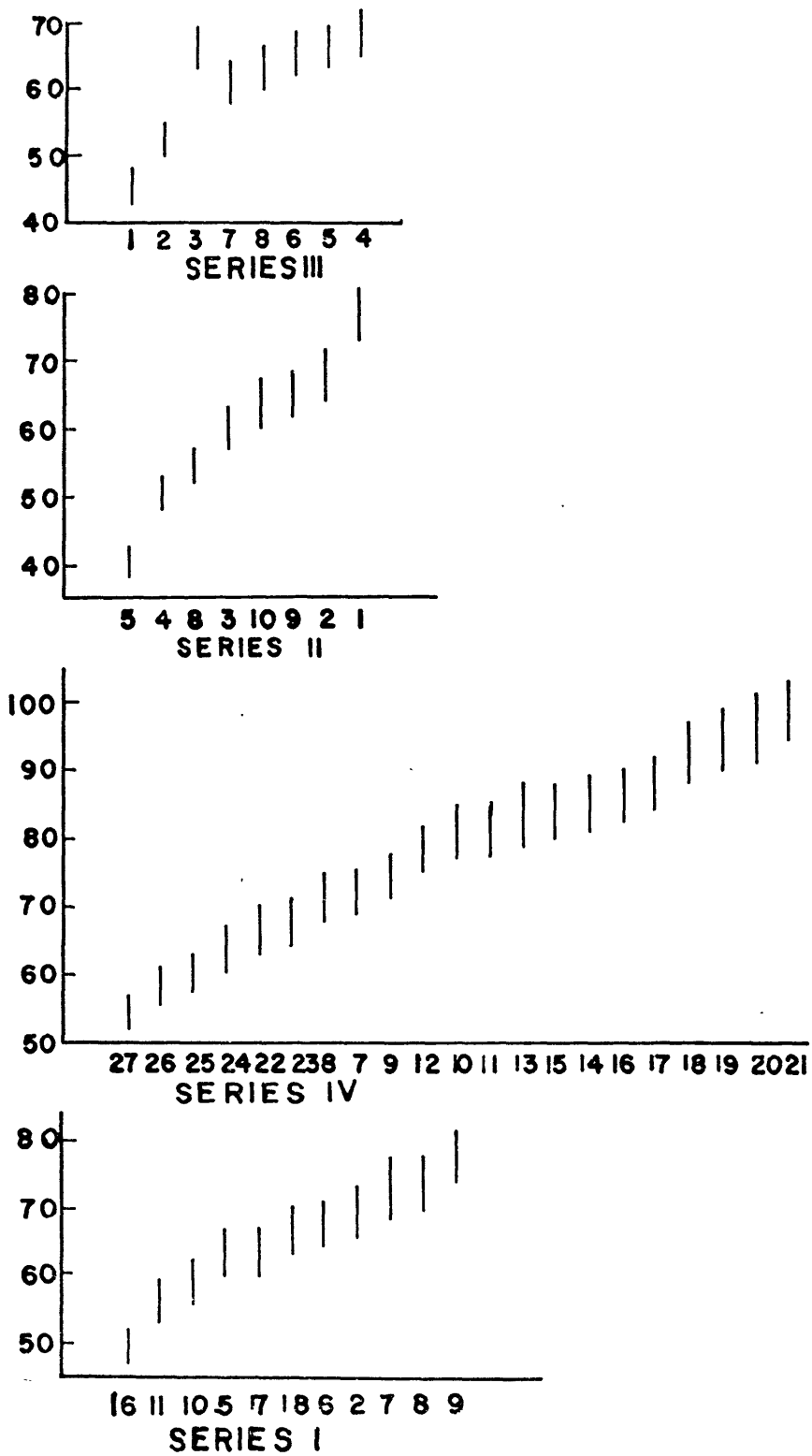

Fig. 4.4. Velocity error bars for flume runs of the pilot study. Vertical axes give velocity in cm/sec; horizontal axes give run number.

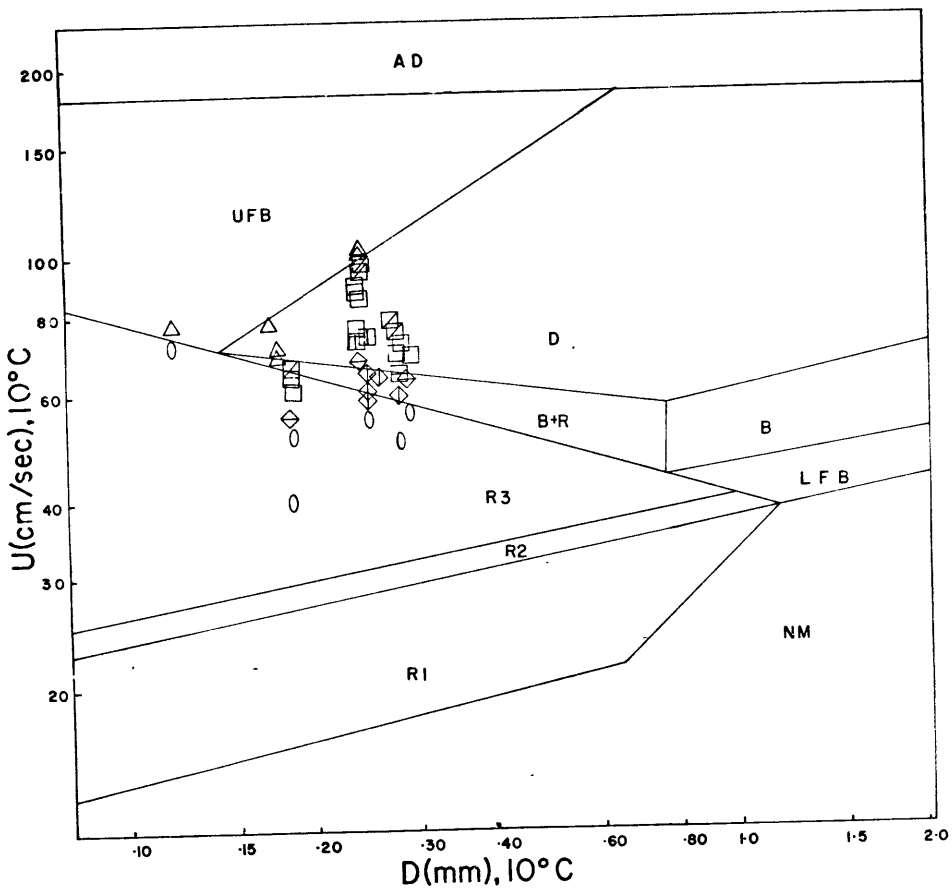

Fig. 4.5. Plot of data onto velocity-size diagram for 50 cm flow depth.

flow depth because of the low maximum attainable velocity at a scale ratio of 1.1, but those data could still be used to approximately fix the location of the upper flat bed/ripple boundary at 50 cm flow depth. That boundary was plotted onto a velocity-size diagram for 50 cm flow depth (Fig. 4.5) from a depth-size diagram at 0.13 mm sand size (Fig. 3.5) by a three-dimensional interpolation. Then, data points (from the pilot study) on either side of that boundary in the depth-velocity diagram were projected from 20 cm to 50 cm flow, depth along lines parallel to that boundary, so that each is the same perpendicular distance from (i.e., relative position to) the boundary at 50 cm as it is at 20 cm flow depth.

Observations of the bed configuration can be considered together in order to describe the changes in the configuration with increasing mean flow velocity and decreasing sand size. Descriptions of the configurations observed while velocity was increased are based on runs of Series IV, for which the most detailed observations were made and greatest width-to-depth ratios used.

High-velocity ripples (Fig. 4.6) tended to be lower in height, less regular in spacing and distribution, and more linguoid than lower-velocity ripples.

With increasing velocity, the bed configuration changed gradationally through two phases for bars until dunes were clearly distinguishable. The first was a hierarchy of bars and ripples (Figs. 4.7, 4.8, and 4.9). Ripples were the

smaller, linguoid features with well-defined scour pits. Bars, the larger feature, were higher, though only slightly higher, and had much greater spacings than ripples; also, bars were consistently associated with flat troughs, unscoured for a distance of 2-3 crest heights downstream. Only in some cases could a mound be identified as the "body" of a bar; distinction was more often made on the basis of trough characteristics and spacing and height. In the low-velocity range of this phase, crests of the bars tended to be irregular but continuous. The percentage of the bed covered with ripples decreased with increasing velocity through the bar plus ripple phase.

With a further increase in velocity, the second bar phase became evident (Figs. 4.10 and 4.11), interpreted as a hierarchy of bars and dunes. For this phase, crests of bed forms were discontinuous and highly irregular. No organization could be discerned from the distribution of bed forms except a kind of offset pattern of trough/mound alternation across the width of the channel. Small-scale ripples were rare. Although the general oval outline of troughs appeared dunelike, most bed forms were considered to be bars because of their low heights and because troughs of most of these bed forms were not highly scoured. (Certain troughs of similarly-sized forms were more scoured than others and might, then, be identified as dunes; see below.)

Dunes (Figs. 4.12 and 4.13), observed at higher velocities, had well-defined, scoured troughs and were generally

higher than bars, although bars and dunes had similar spacings. The scoured, concave portion of the trough tended to extend two to three crest heights downstream from the crest. With increasing velocity, the spacing of dunes tended to increase steadily from about 1.5 m to greater than 4 m, while height increased from about 10 cm to a maximum of about 35 cm and then decreased to 10 cm.

As dune heights increased, the extent of low, *en echelon* ripples over the stoss slopes of dunes diminished, from full coverage to just the lower portion of the dune back, downstream of the "inflection point" where trough concavity ends. Uncovered areas of the dune back were flat and micro-lineated, with lineations oriented roughly perpendicular to the slip face of the dune. At velocities producing maximum dune heights and subsequently lower heights, dune backs were partially or completely flat, although at those velocities, ripples commonly were present in troughs of dunes (Fig. 4.14).

Dune crests, which were continuous across the width of the channel, changed from straight or somewhat wavy in the low-velocity range of the dune stability field to straight or distinctly cuspate (Fig. 4.15) at velocities past which the maximum dune height had been reached. Cuspate crests rimmed troughs in a bowl-like manner. Portions of the dune front, the "horns," tended to be rounded or crestless and rippled; the central portion of the dune front, however, had a distinct crest and was angular.

At the highest velocities for which dunes were stable,

the spacing-to-height ratio of dunes increased greatly as spacings increased while heights decreased (Figs. 4.16 and 4.17). Troughs were not as concave as at lower velocities, but were much longer, extending downstream nearly to the crest of the next dune. The flume was turned off more frequently than usual to observe the bed because the sidewall expression of crests was extremely poor, cuspate dunes tending to have horns at generally the same level as the surrounding bed. For long periods of time, up to two hours, only flat bed was observed. Either spacings between bed forms was very long or, more likely, dunes formed from and attenuated to a flat bed while out of view. When crests were observed, they were observed in pairs (Fig. 4.18), with the downstream form being generally lower than the upstream form. For a further increase of velocity, the configuration changed rather abruptly to stable upper flat bed.

At the coarser sand size for Series I (0.28 mm) the sequence of bed phases was essentially the same as for Series IV (0.24 mm), except that the bars observed in the bar-plus-ripple bed phase were somewhat higher and better defined. For Series II (0.19 mm) the sequence of bed phases was similar to that observed for Series IV; however, the interval of velocity over which bars and dunes were stable was narrower for Series II, so that the sequence of bed configurations with increasing velocity appeared compressed. Also, rounded dune fronts with crests and slip faces occurring only down the centerline of the channel were often observed during dune

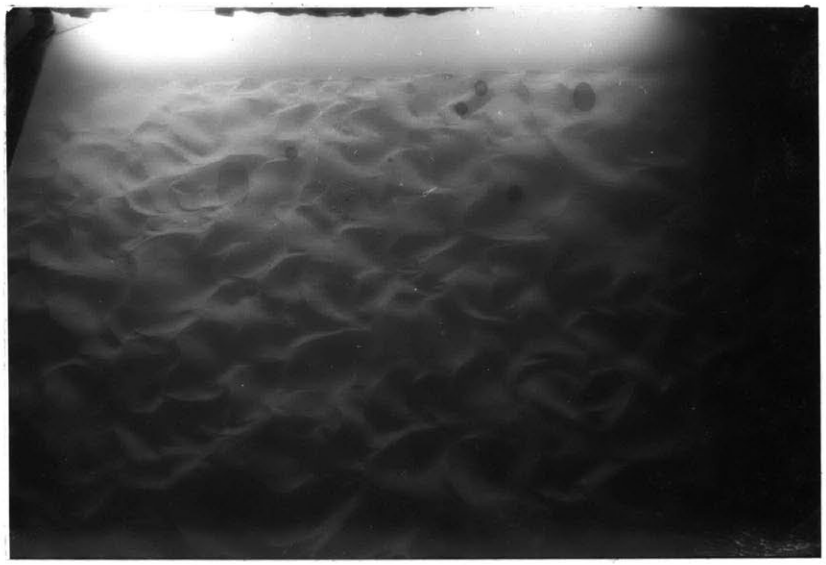

Fig. 4.6. Run IV-27, U = 54 cm/sec. Linguoid ripples. (Flow right to left for Fig. 4.6-4.17 unless otherwise noted.) Channel width is 90 cm across.

Fig. 4.7. Run IV-26, U = 58 cm/sec. Bars plus ripples. Outline of bar to far left; side of bar shaded in foreground. Note flat trough.

Fig. 4.8. Run IV-25, U = 60 cm/sec. Bars plus ripples. Bar to right, with continuous crest and flat relatively long trough.

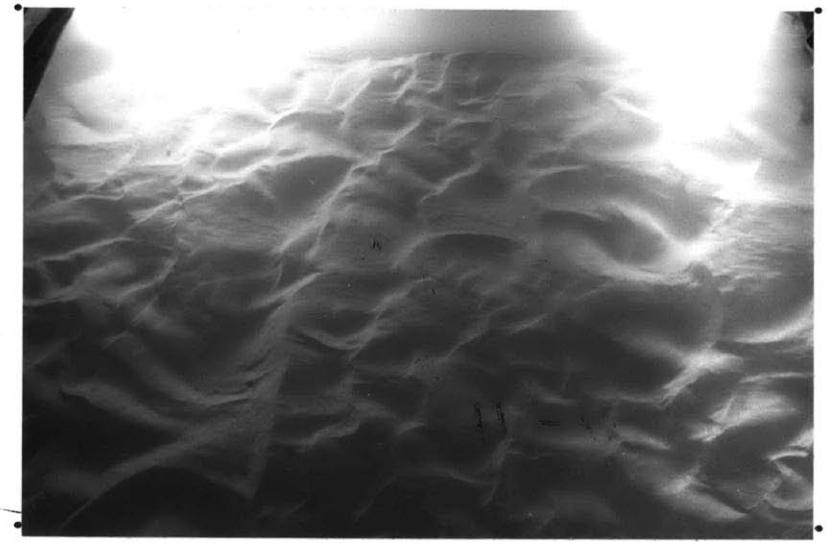

Fig. 4.9. Run IV-24, U = 64 cm/sec. Bars plus ripples. Bar with continuous crest, higher than ripples.

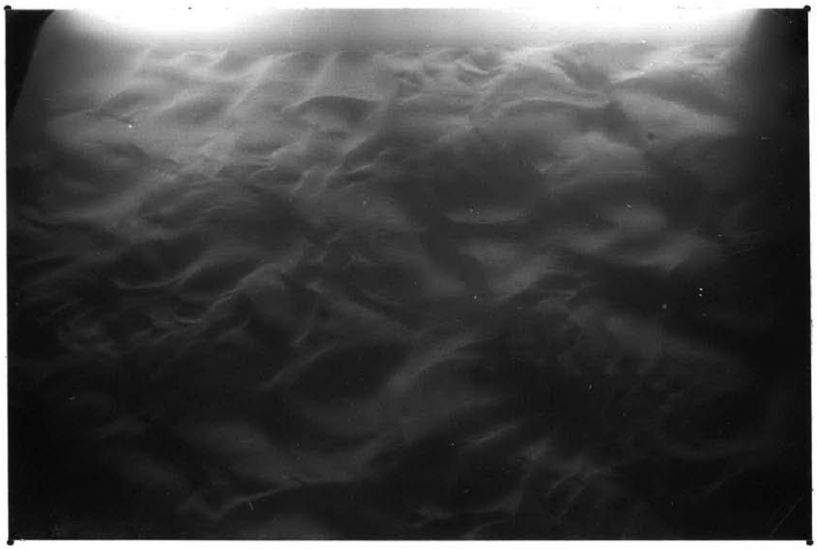

Fig. 4.10. Run IV-23, U = 68 cm/sec. Bars plus dunes. Non-continuous crests; irregular distribution of forms. Oval troughs, some deeper than others.

Fig. 4.11. Run IV-22, U = 67 cm/sec. Bars plus dunes. Semi-continuous crests. Flattish bar trough to right; scoured dune trough to left.

Fig. 4.12. Run IV-8, U = 72 cm/sec. Dunes plus ripples. Scoured, unrippled trough and rippled dune-back. Flow from bottom to top.

Fig. 4.13. Run IV-7, U = 73 cm/sec. Dunes plus ripples. Scoured, lobed trough. *En echelon* ripples forming at end of trough and covering duneback on left.

Fig. 4.14. Run IV-13, U = 84 cm/sec. Dunes. High, straight-crested, flat-backed dune. Well-defined trough with *en echelon* ripples. Note streaks normal to crest. Lineations at base of slip face indicative of cross-currents in trough.

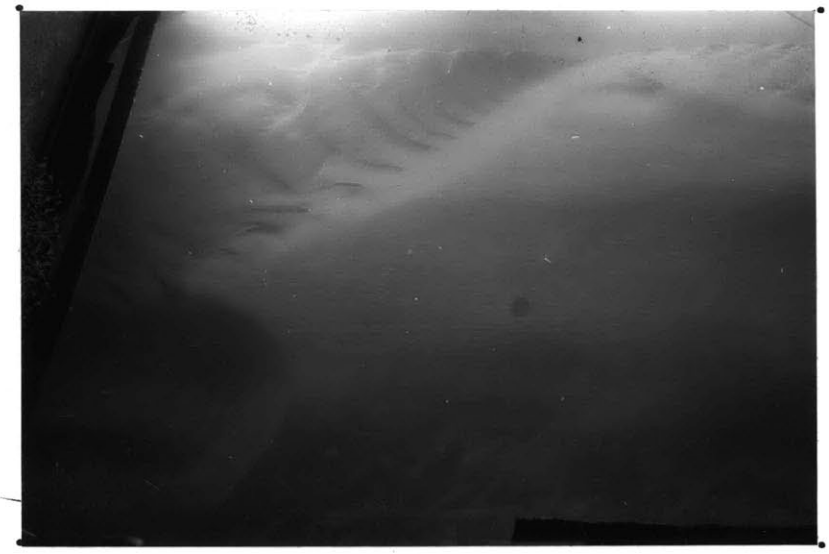

Fig. 4.15. Run IV-15, U = 84 cm/sec. Dunes. Cuspate, rippled dune front (upper left). Streaks normal to slip face (lower left). Transitional between dunes and flattened dunes.

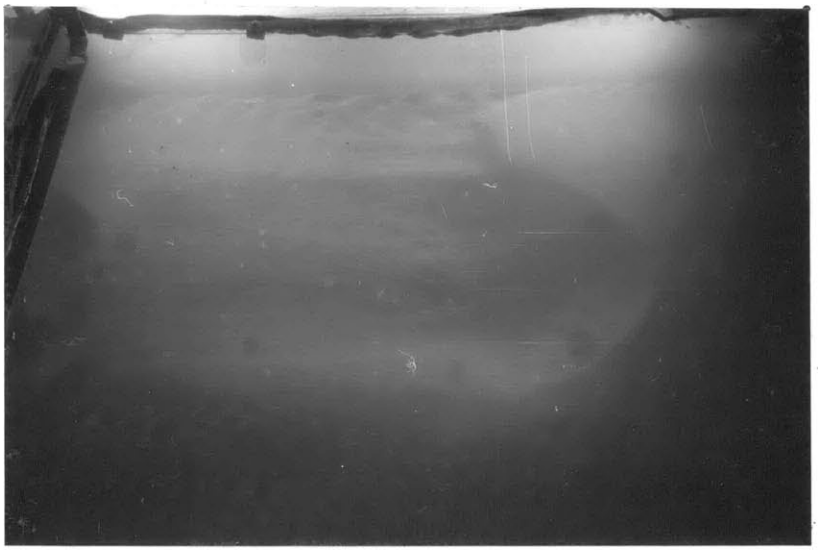

Fig. 4.16. Run IV-17, U = 88 cm/sec. Flattened dunes. Dunes occur in pairs. No ripples on bed. Cuspate crests.

Fig. 4.17. Run IV-19, U = 95 cm/sec. Flattened dunes. Low wavy to cuspate crest on right. Long, relatively featureless scoured trough.

runs of Series II.

For Series III, having the finest sand size (0.12 mm) of the pilot study, the sequence of bed phases differed from the sequence cited above for the other series. With increasing velocity, the sequence was ripples, modified ripples, and upper flat bed. No dunes or bars were observed. The modified linguoid ripples were dunelike in that their troughs were unusually broad and fan-shaped, up to 25 cm across. The plan pattern of these ripples was similar to the offset pattern of bars and dunes in the bars-plus-dunes bed phase (Fig. 4.11), but heights, spacings, and particularly the scoured troughs marked these forms as ripples.

Contouring the depth-velocity-size diagram.

Trends observed for mean bed-form height from this and other studies are summarized in two qualitatively contoured diagrams, a velocity-size diagram and a depth-velocity diagram (Figs. 4.18 and 4.19).

Simplifying the three-dimensional surface plotted over these projections to a plane, there are four general kinds of orientations for that plane: a) sloping upward from lower right to upper left, b) sloping downward from lower right to upper left, c) sloping upward from lower left to upper right, d) sloping downward from lower left to upper right. For an ordinate and abscissa symbolically referrred to as y and x, the dependent variable increases for each of the above orientations with a) $-\Delta x$ and $+\Delta y$, b) $+\Delta x$ and $-\Delta y$, c) $+\Delta x$ and

$+\Delta y$, d) $-\Delta x$ and $-\Delta y$. In Table 4.2, each general planar orientation a-d is associated with its change with x and y and a contour pattern.

The trends observed in bed-form height for the following bed phases were:

1) ripple height, for all three ripple fields, decreasing with increasing velocity and increasing with decreasing sand size (from results of Part II and Part IV);

2) bar height increasing with increasing velocity (Part IV) and increasing with increasing sand size [the sand waves and transverse bars observed by Jackson (1975) should plot in the same stability field, the former being higher and occurring in sand sizes coarser and velocities and depths somewhat higher than the latter];

3) dune height increasing and then decreasing with increasing flow velocity and decreasing with decreasing sand size (Guy et al., 1966, and Part IV);

4) height for all bed phases increasing with increasing depth, but ripples less so (Coleman, 1967, and Part IV).

These trends were qualitatively contoured in a velocity-size diagram (Fig. 4.18) in the following manner: 1) ripple fields were contoured by "type d" contours (see Table 4.2), 2) bar fields by "type c" contours (tangency to bar/lower flat bed boundary not illustrated), 3) dune field by "type c" and "type a" contours, producing a herringbone pattern (tangency to dune/upper flat bed boundary not illustrated).

Trends were contoured in a depth-velocity diagram (Fig.

TABLE 4.2: Generalized contour patterns.

CONTOUR TYPE	SLOPE OF PLANE	+ΔA FOR ΔX AND ΔY	CONTOUR PATTERN *
a	upward from lower right to upper left	-Δx and +Δy	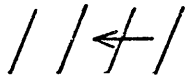
b	downward from lower right to upper left	+Δx and -Δy	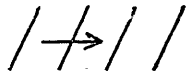
c	upward from lower left to upper right	+Δx and +Δy	
d	downward from lower left to upper right	-Δx and -Δy	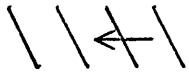

*Arrows in direction of +ΔA.

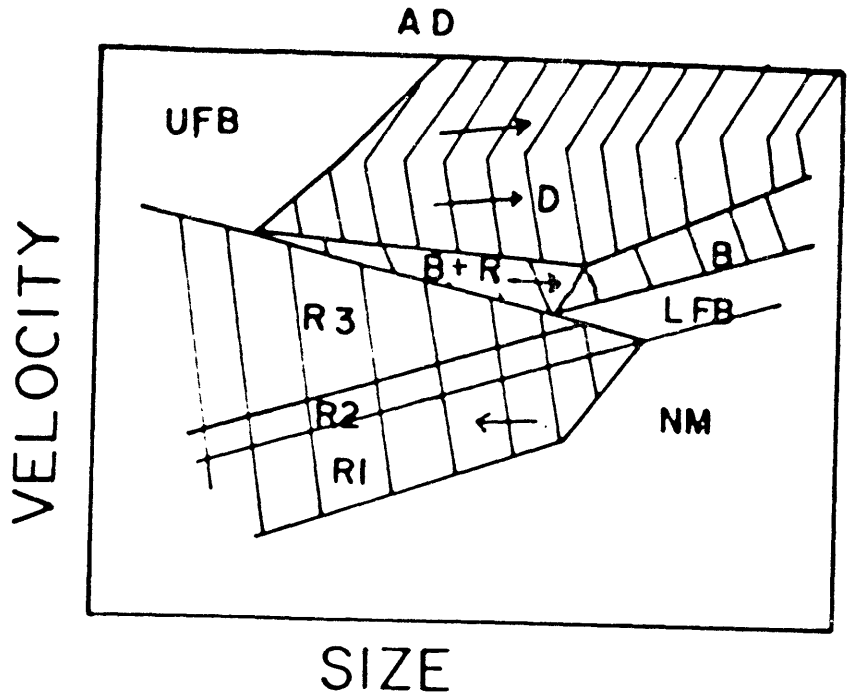

Fig. 4.18. Velocity-size diagram (50 cm flow depth) qualitatively contoured for bed-form height; arrows in direction of +ΔA.

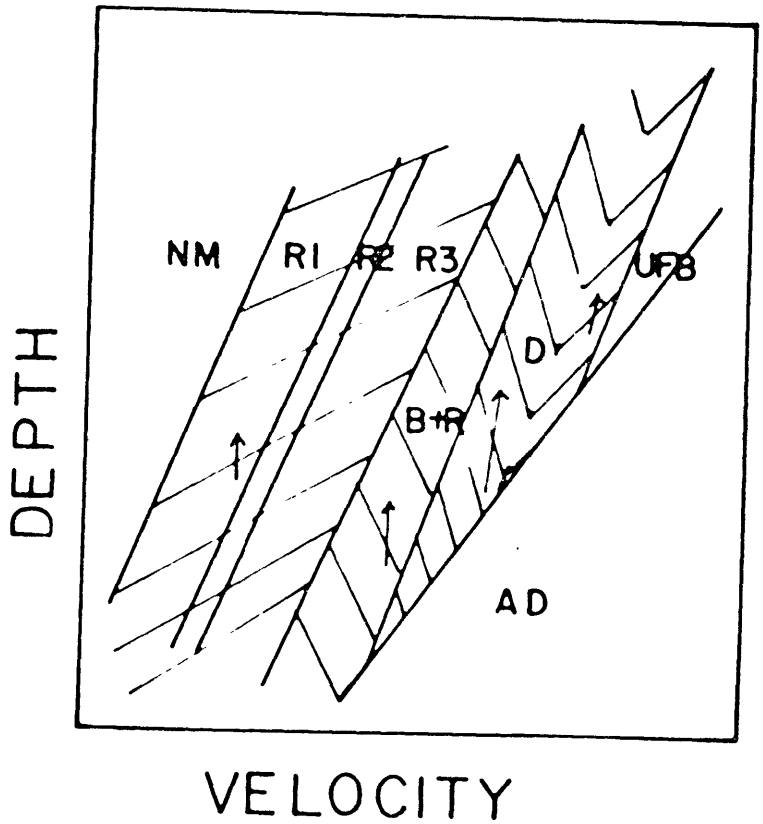

Fig. 4.19. Depth-velocity diagram (0.30 mm sand size) qualitatively contoured for bed-form height; arrows in direction of +ΔA.

4.19) for a sand size like 0.30 mm as follows: 1) ripple fields were contoured by "type a" contours, 2) bar fields by "type c" contours, 3) dune field by "type c" and "type a" contours, producing a herringbone pattern. Tangency of contours to certain boundaries was not illustrated in this figure.

Covariation of several dependent variables, such as bed form spacing, bed form height, and sediment discharge, could be visualized by overlaying contours for each dependent variable onto the same diagram; no such figure is presented here because of insufficient data. No correlations with bed phase or any dependent measure of the bed configuration could be visualized within the framework of the depth-velocity-size diagram for contours for the independent parameters depth Reynolds number, sediment-size Reynolds number, or Froude number, except for the correspondence of Froude number with the boundary for antidunes.

DISCUSSION

Existence of the bar bed phase was confirmed for fine sand sizes at velocities intermediate between those producing ripples and dunes. Like the bars observed by Costello (1974), bed forms of this bed phase had continuous wavy crests, flat featureless troughs, and fairly large spacing-to-height ratios. Because their height was comparable to that of ripples, effectively "masking" their occurrence, it is not surprising that bars as a distinct bed phase often escaped detection in

studies like those of Willis et al. (1972) and Hill et al. (1969).

At fine sand sizes bars first appear with increasing velocity in a hierarchy with ripples, as observed in this study; for coarse sand sizes Costello (1974) observed bars with no ripples present. Thus, in the depth-velocity-size diagram constructed in Part III, the subdivision of the bar stability field according to bed-form hierarchy is valid. Bed states for bars plus dunes, plotting in the upper-velocity range of the bar stability field in diagrams constructed in Part III, were identified in this study with configurations gradational between bars and dunes; the distinction between bars and dunes might be better defined at deeper flow depths.

Based on the results of the pilot study, the dune field could be subdivided into a field for dunes and flattened dunes, dune field A and dune field B, respectively. With increasing mean flow velocity, dunes of dune field A increase in height and spacing while ripples cover increasingly less of the dune back, disappearing from the higher areas first, and more of the trough. The change in ripple distribution is thought to represent: a) the intensity of cross-currents and reverse flow in the trough increasing with increasing mean flow velocity to levels at which grain movement in the trough results in the formation of ripples instead of a locally flat bed, and b) the gradient of bed shear stress up the stoss slope of the dune back increasing with increasing

mean flow velocity so that ripples, which are initiated in the region of boundary-layer reattachment and migrate upslope into regions of increasing shear stress while becoming steadily lower (just as ripples at lower velocities decrease in height with increasing mean flow velocity/mean bed shear stress), virtually disappear from regions of high shear stress, from the top of the dune back downward with increasing velocity.

For velocities higher than those for dune field A, the flattened dunes of dune field B decrease in height but increase in spacing with increasing mean flow velocity; and ripples, if observed at all, are present only in troughs. Bed-form hierarchy further distinguishes dune field B from dune field A: the frequency with which flat bed instead of flattened dunes was observed for bed states of dune field B denotes a hierarchy of flattened dunes and upper flat bed.

The pinching out of the bar and dune stability fields with decreasing sand size in velocity-size diagrams was evident from the decrease of the velocity interval over which bars and dunes were stable from Series I to Series IV and especially from Series IV to Series II. In addition, no dunes or bars were observed for Series I (0.12 mm). Near the "point" at which the bar and dune fields pinch out, the characterization of bed phases becomes blurred as each possesses attributes of more than one bed phase. For example, at a sand size coarser than that "point," sand waves (cf. Run II-8) like those observed by Vanoni and Brooks (1957) and Barton and Lin

(1955) resemble elongated bars but had scoured troughs and ripple-free stoss slopes, so that they more closely resembled long dunes with flat backs and rippled troughs. For sand sizes finer than that "point" (near the tip of the bar field in the depth-velocity diagram for 0.13 mm, Fig. 3.5), ripples in the upper-velocity range of the ripple field (cf. Run III-7) resemble dunes in the broad fan-like span of their troughs. Further investigation at deeper flow depths and sand sizes from about 0.08 mm to 0.2 mm could better define these characterizations.

Except for data for Series II, which at least plots in the proper velocity intervals for each bed phase, a plot of data from this pilot study onto a velocity-size plane is consistent with boundaries of a velocity-size diagram for 50 cm flow depth (Fig. 4.5), constructed by three-dimensional interpolation from the depth-velocity-size diagram from Part III. Also, data from Series III would plot consistently with boundaries of the depth-velocity diagram for 0.13 mm sand size (Fig. 3.5), the diagram whose boundary placement is most open to interpretation. Thus, placement of boundaries in the depth-velocity-size diagram must be generally correct.

Placement of boundaries relative to the axes--and so the relative positions of bed-phase stability fields--is the same whether the depth-velocity-size diagram is considered dimensionally or dimensionlessly. Thus, the essential criteria distinguishing bed phases are processes because dimensional measures of the con-

figuration are merely effects of processes and vary according to water temperature.

The next step after this pilot study involves deep-water flume experiments. As a rough guide for those experiments, a velocity-size diagram for a 2.5 m flow depth was constructed by three-dimensional interpolation (Fig. 4.20). Agreement of data from such experiments with boundaries of this diagram will determine whether, with increasing mean flow depth, boundaries in depth-velocity diagrams are straight, so that they can be extrapolated linearly, as assumed for construction of this velocity-size diagram, or whether boundaries curve. Also, it will be determined whether there are stability fields in depth-velocity diagrams that pinch out with decreasing depth--as the upper-flat-bed field at medium and coarse sand sizes must (see Fig. 3.7)--at depths deeper than about a half meter, the deepest depth documented in the depth-velocity-size diagram to date.

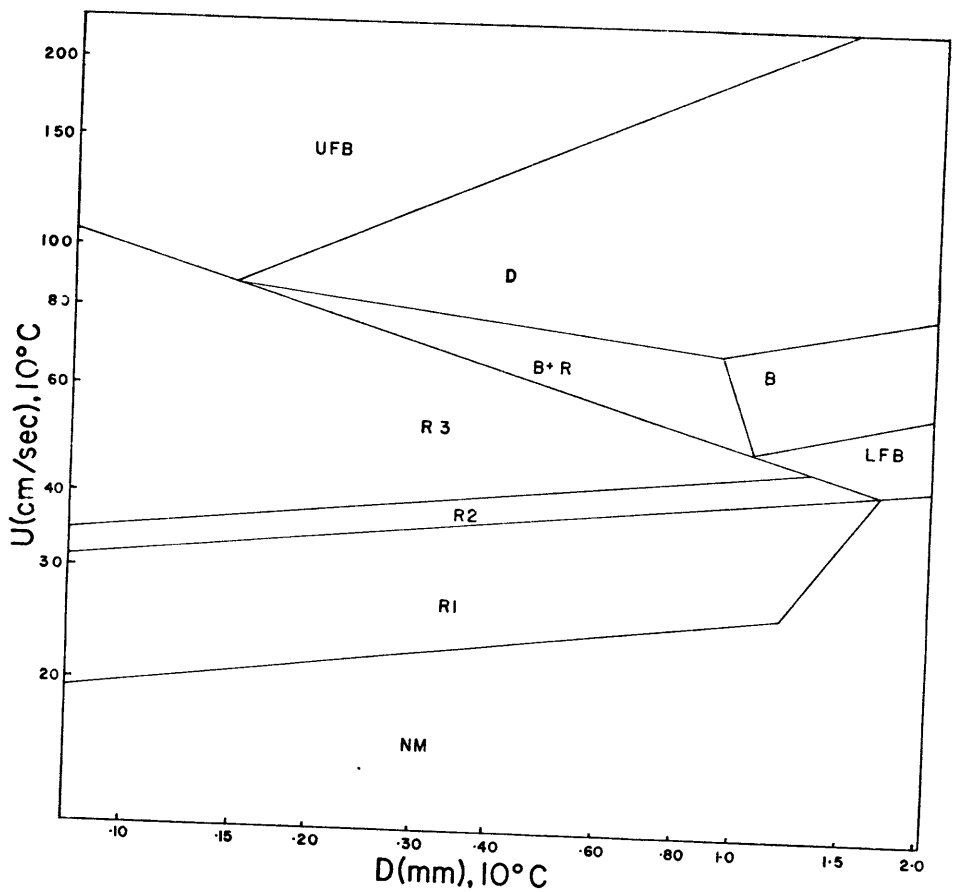

Fig. 4.20. Velocity-size diagram for 2.5 m flow depth.

PART V: SUMMARY OF CONCLUSIONS

The chief conclusions of this study are summarized and evaluated together in this section.

The initial motivation for this study came from the need to study sediment transport on the scale of bed configurations under controlled conditions at natural depths. Such studies would be made possible by developing a method for dynamic scale modeling of bed configurations. Any model is dynamically similar to its prototype if and only if all significant forces are properly modeled, as determined by the identity of values of corresponding force ratios for model and prototype. It was proposed that seven independent variables, as a set, were necessary and sufficient to fully characterize all aspects of a flow system and the associated bed configuration. These fundamental variables are gravitational acceleration, mean flow depth and mean flow velocity, fluid density and viscosity, and sediment density and median sediment size, characterizing, respectively, the force field on the system, the flow, the fluid, and the sediment. A set of dimensionless parameters derived from that set of fundamental variables should also fully characterize the same system; if corresponding dimensionless parameters of a model and its prototype are identical, then the two systems are dynamically similar. From these correspondences come the following equations determining dynamic similitude for bed configurations:

$$l_r = \left(\frac{\nu_r^2}{g_r}\right)^{1/3} \tag{1.6}$$

$$\left(\frac{\rho_s}{\rho}\right)_r = 1 \tag{1.7}$$

The validity of these equations was tested by comparing cumulative frequency curves for dependent measure of two very carefully controlled flume runs, one a cold-water prototype and the other a hot-water model. For each of three dependent variables (bed-form spacing, bed-form height, and bed-form migration time), coincidence between cumulative frequency curves for the prototype and scaled-up model was excellent. A third run showed that coincidence of curves was not fortuitous. This test therefore verified that the set of seven variables was a complete fundamental set and proved that dynamic scale modeling of bed configuration is possible. These conclusions formed the basis for the remainder of this study.

A graphic correlation of independent variables and bed phase could plot with overlap of fields, indicative of an underspecified system, or with field boundaries parallel to axes of the plot, indicative of an overspecified system, unless a set of necessary and sufficient independent variables is used. The modeling test established that set of variables. Thus, a plot proposed by Southard (1971) is valid because it is based on this same set of variables. The dimensionless parameters used for that plot are derived by the only dimensional analysis of the set of fundamental variables that

leads to both correlation of bed phase with explicit environmental determinants and visualization of that correlation in three dimensions. For quartz-density sand, correlation is reduced to a three-dimensional diagram with bed phase plotted within the diagram as the fourth variable; for quartz-density sand and a standard temperature, the three dimensionless parameters are reduced to explicitly dimensional variables of sedimentological interest: mean flow depth, mean flow velocity, and median sediment size. A procedure was developed for normalizing data to a standard water temperature (of 10°C) based on principles of dynamic similitude, so that data measured at different temperatures could be compared. Existing flume data from other studies were then normalized and plotted according to bed-form hierarchy (a further refinement in the concept of bed phase) in projections of the depth-velocity-size diagram. Boundaries between bed-phase stability fields in each projection were fully delineated by three-dimensional interpolation among projections.

Some of the most interesting relations among stability fields are pinch-outs of fields, which reflect yet unknown dynamics, observed in the following projections: in velocity-size diagrams, the ripple field with increasing sediment size, and bar, dune, and lower-flat-bed fields with decreasing sediment size; in depth-velocity diagrams for medium to coarse sediment sizes, the lower-flat-bed field with increasing depth, and the ripple and upper-flat-bed fields with decreasing depth; in depth-size diagrams, the bar, dune, and upper-

flat-bed fields with increasing depth, giving way to ripples or no movement at great depths. (Boundaries and stability fields can be visualized in three dimensions through the volume of the depth-velocity-size diagram by stacking transparencies of projections into a three-dimensional grid.) Also, the depth-velocity-size diagram is the basis for a procedure predicting the observed change of bed phase and/or some dependent measure of the configuration with a change in water temperature as well as with a change in any six of the seven fundamental variables--excluding sediment density--given the initial conditions and the change in the independent variables. In general, the depth-velocity-size diagram is a framework for organizing data and structuring concepts of sediment transport dynamics.

A pilot study was carried out to determine the practicality of dynamic scale modeling using hot water with a flume and scale ratio larger than were used for the modeling test. Using hot-water modeling in a very large flume, natural depths can be simulated. Using hot-water modeling in a small flume, a larger flume can be simulated, representing many cost-effective savings and making existing flumes more flexible tools for research. (Rather than using hot water to simulate a larger system, one could use a fluid more viscous than water to simulate a smaller system, thus facilitating study of small-scale phenomena.) While a procedure for hot-water modeling with a covered, insulated flume was being developed, experiments were made in which certain of the relations ob-

served in the depth-velocity-size diagram constructed in Part III were confirmed. Results for runs made at about 50 cm flow depth for fine sand sizes, where sand size was changed merely by varying water temperature, were as follows. Bars, with heights similar to ripples and spacings similar to dunes, were stable at velocities intermediate to those producing ripples and dunes. With increasing flow velocity, the spacing of dunes increased, while the height of dunes increased and then decreased. With decreasing sand size the interval over which dunes and bars are stable decreased until both stability fields pinched out at a sand size slightly coarser than 0.12 mm; for sizes finer than that "point," the sequence of bed phases observed with increasing velocity is ripples, modified ripples, and upper flat bed. Near the "point" of pinch-out, distinction of bed forms is somewhat blurred because bed forms appear to possess attributes of adjacent stability fields. In addition to these results, data for bed-form height from this and other studies were summarized in qualitatively contoured depth-velocity and velocity-size diagrams.

These results confirm the extension of the bar stability field into fine sand sizes, the pinch-out of bar and dune stability fields with decreasing sand size, the subdivision of the bar field according to bed-form hierarchy, and the subdivision of the dune field into dunes and flattened dunes. A plot of data onto the velocity-size plane agreed with boundaries of a velocity-size diagram constructed by three-

dimensional interpolation of the depth-velocity-size diagram. Thus, placement of boundaries in the depth-velocity-size diagram was generally correct. Validating the construction of this diagram verified that the essential distinction among bed phases is process, not dimensional measures, which are effects of a process. Finally, given the practicality of hot-water modeling and the consolidation of existing flume data, a velocity-size diagram for a 2.5 m flow depth was constructed as a rough guide for the next generation of deep-water flume experiments.

In conclusion, based on having established the fundamental variables for bed configurations, this study has provided a framework and an experimental means for further understanding processes of sediment transport. These processes, acting in days and months, shape man's environment within his time frame. With his understanding of these processes, man can not only reconstruct past environments--and so better comprehend these and other systemic processes--he can intelligently adapt to and influence his environment.

BIBLIOGRAPHY

Barton, J.R. and Lin, R.N., 1955, A study of the sediment transport in streams, Report No. 55JRB2, Civil Eng. Dept., Colorado A&M College, Fort Collins, Colo.

Boguchwal, L.A., 1972, Transition from ripples to lower flat bed with increasing mean flow velocity and median sediment size, B.A. Thesis, Harvard University, Cambridge, Mass., 72 p.

Boothroyd, J.C. and Hubbard, D.K., 1975, Genesis of bed forms in meso-tidal estuaries: in Cronin, L.E., ed., Estuarine Research, 2, New York, Academic Press, p. 217-235.

Brooks, N.H., 1958, Mechanics of streams with movable beds of fine sand, Amer. Soc. Civil Eng. Trans., 123, p. 526-549.

Buckingham, E., 1914, On physically similar systems; illustrations of the use of dimensional equations, Physical Review, IV, no. 4, p. 345-376.

Chabert, J. and Chauvin, J.L., 1963, Formation des dunes et des rides dans les modèles fluviaux, Bull. Cent. Rech. Ess. Chatou, 4, p. 31-51.

Chepil, W.S., 1961, The use of spheres to measure lift and drag on wind-eroded soil grains, Soil Sci. Soc. Amer. Proc., 25, p. 343-345.

Coleman, N.L., 1967, A theoretical and experimental study of drag and lift forces acting on a sphere resting on a hypothetical stream bed, Proc. 12th Congress, Internatl. Assoc. Hydraulic Res., 3, p. 185-192.

Costello, W.R., 1974, Development of bed configurations in coarse sands, Report 74-1, Mass. Inst. Technol., Dept. of Earth and Planetary Sciences, Cambridge, Mass., 120 p.

Dalrymple, R.W., 1977, Sediment dynamics of macrotidal sand bars, Bay of Fundy, Ph.D. Thesis, McMaster University, Hamilton, Ont., 630 p.

Davies, T.R., 1971, Summary of experimental data for flume tests over fine sand, Report No. CE/3/71, Civil Eng. Dept., University of Southhampton, Southhampton, England.

Franco, J.J., 1968, Effects of water temperature on bed-load movement, Proc. Amer. Soc. Civil Eng., J. Waterways and Harbors Div., 94, WW 3, p. 343-352.

Friedkin, J.F., 1945, A laboratory study of the meandering of alluvial rivers, U.S. Army Corps of Engineers, U.S. Waterways Experiments Station, Vicksburg, Miss., 40 p.

Guy, H.P., Simons, D.B. and Richardson, E.V., 1966, Summary of alluvial channel data from flume experiments, 1956-61, U.S. Geol. Survey, Prof. Paper 462-I.

Handbook of Chemistry and Physics, 1976, R.C. Weast, ed., 57th edition, Chemical Rubber Co. Press.

Hill, H.M., Srinivasan, V.S., and Unny, T.E., 1969, Instability of flat bed in alluvial channels, Proc. Amer. Soc. Civil Eng., J. Hydraul. Div., 95, HY5, p. 1545-1556.

Jackson, R.G., II, 1975, Velocity--bed-form--texture patterns of meander bends in the lower Wabash River of Illinois and Indiana, Geo. Soc. Amer. Bull., 86, p. 1511-1522.

Kennedy, J.F., 1963, The mechanics of dunes and antidunes in erodible-bed channels, J. Fluid Mech., 16, p. 521-544.

Maddock, T., 1970, Indeterminate hydraulics of alluvial channels, Proc. Amer. Soc. Civil Eng., J. Hydraul. Div., 96, HY 11, p. 2309-2323.

Nordin, C.F., Jr., 1976, Flume studies with fine and coarse sands, U.S. Geol. Survey, Open File Report 76-762, Denver, Colo.

Pratt, C.J. and Smith, K.V.H., 1972, Ripple and dune phases in a narrowly graded sand, Proc. Amer. Soc. Civil Eng., J. Hydraul. Div., 98, HY 5, p. 859-874.

Raudkivi, A.J., 1963, Study of sediment ripple formation, Proc. Amer. Soc. Civil Eng., J. Hydraul. Div., 89, HY 6, p. 15-33.

Schumm, S.A. and Khan, H.R., 1972, Experimental study of channel patterns, Geol. Soc. Amer. Bull., 83, no. 6, p. 1755-1770.

Simons, D.B. and Richardson, E.V., 1963, Forms of bed roughness in alluvial channels, Amer. Soc. Civil Eng. Trans., 128, Part I, p. 284-302.

Southard, J.B., 1971, Representation of bed configurations in depth-velocity-size diagrams, J. Sed. Petrol., 41, p. 903-915.

Southard, J.B. and Boguchwal, L.A., 1973, Flume experiments on the transition from ripples to lower flat bed with increasing grain size, J. Sed. Petrol., 43, p. 1114-1121.

Southard, J.B. and Middleton, G.V., 1977, Mechanics of Sediment Movement, S.E.P.M. Short Course No. 3.

Straub, L.G., Anderson, A.G. and Flammer, G.H., 1958, Experiments on the influence of temperature on the suspended load, M.R.D. Sediment Series No. 10, University of Minnesota, St. Anthony Falls Hydraulic Lab., U.S. Army Corps of Engineers, Missouri River Div., Omaha, Neb.

Taylor, B.D., 1974, Temperature effects in flows over non-planar beds, Proc. Amer. Soc. Civil Eng., J. Hydraul. Div., 100, HY 12, p. 1785-1807.

Taylor, B.D. and Vanoni, V.A., 1972, Temperature effects in low-transport, flat-bed flows, Proc. Amer. Soc. Civil Eng., J. Hydraul. Div., 98, HY 8, p. 1427-1445.

Taylor, B.D. and Vanoni, V.A., 1972, Temperature effects in high-transport flat-bed flows, Proc. Amer. Soc. Civil Eng., J. Hydraul. Div., 98, HY 12, p. 2191-2206.

U.S. Army Corps of Engineers, 1969, Missouri River channel regime studies, M.R.D. Sediment Series No. 13B, Missouri River Division, Omaha, Neb.

Vanoni, V.A., 1974, Factors determining bed forms in alluvial channels, Proc. Amer. Soc. Civil Eng., 100, HY 3, p. 363-377.

Vanoni, V.A. and Brooks, N.H., 1957, Laboratory studies of the roughness and suspended load of alluvial streams, M.R.D. Sediment Series No. 11, Calif. Inst. Technol., Sedimentation Lab., U.S. Army Corps of Engineers, Missouri River Division, Omaha, Neb.

Williams, G.P., 1967, Flume experiments on the transport of a coarse sand, U.S. Geol. Survey, Prof. Paper 562-B.

Williams, G.P., 1970, Flume width and water depth effects in sediment-transport experiments, U.S. Geol. Survey, Prof. Paper 562-H.

Willis, J.C., Coleman, N.L., and Ellis, W.M., 1972, Laboratory study of transport of fine sand, Proc. Amer. Soc. Civil Eng., J. Hydraul. Div., 98, HY 3, 489-502.

Yalin, M.S., 1965, Similarity in sediment transport by currents, Hydraulics Research Paper No. 6, Hydraulics Research Station, Walingford, Berkshire, England, p. 1-25.

Yalin, M.S., 1977, On the determination of ripple length, Proc. Amer. Soc. Civil Eng., J. Hydraul. Div., 103, HY 4, p. 439-442.

APPENDIX

The source of each data point in Figs. 3.1-3.12 could not be clearly indicated because of the many symbols used for bed phases. Therefore, the data for four velocity-size diagrams (Figs. 3.1-3.4) are plotted according to source in Fig. A.1-A.4. These same diagrams give a fairly accurate idea of the source of data for the depth-velocity diagrams (Figs. 3.5-3.12), also. The legend for Figs. A.1-A.4 appears in Fig. A.5 (fold out for reference).

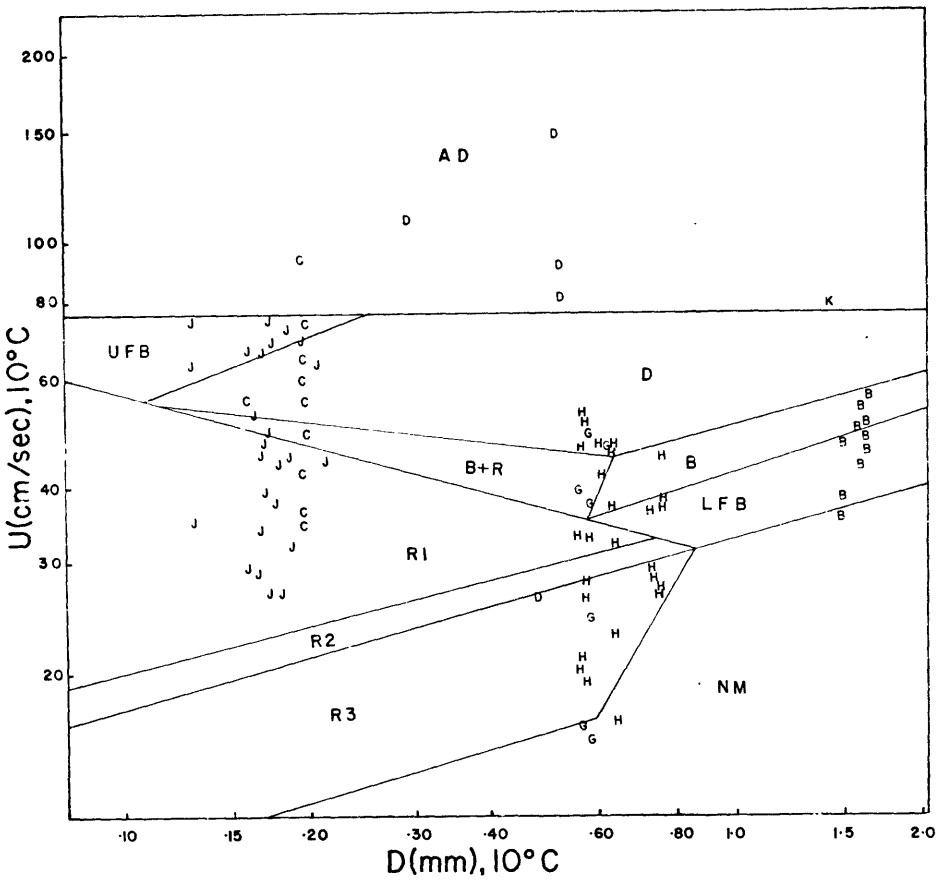

Fig. A.1. Plot by source of data for Fig. 3.1 (velocity-size diagram for 8.5 cm flow depth).

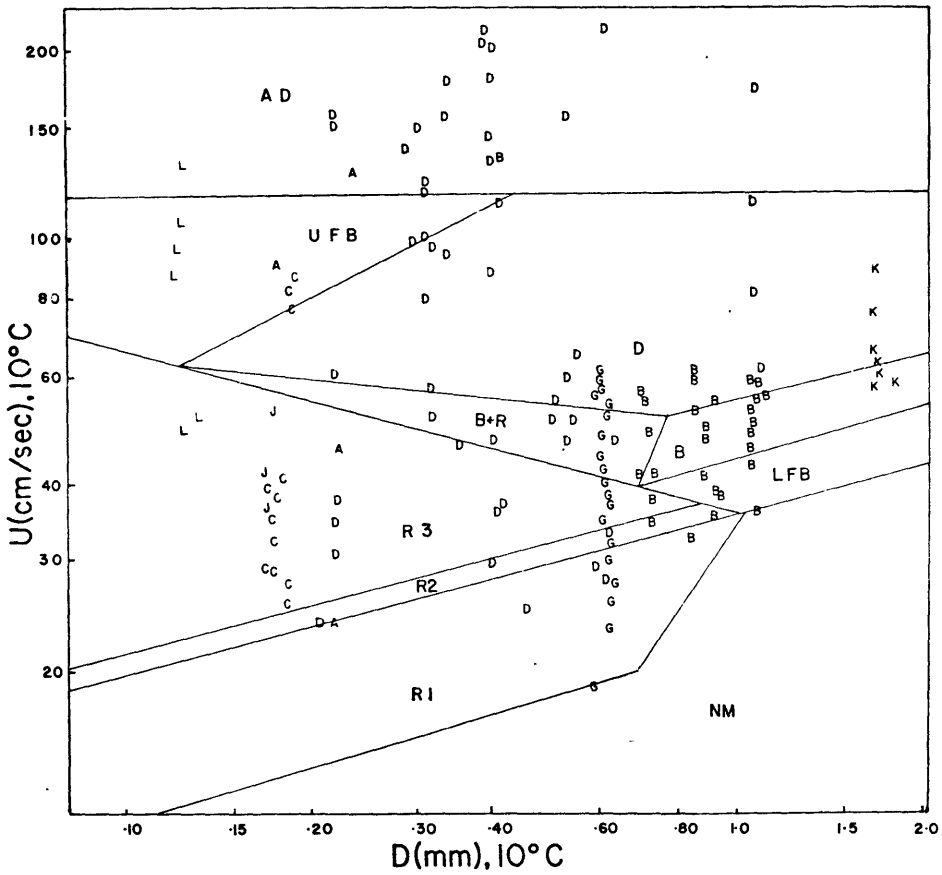

Fig. A.2. Plot by source of data for Fig. 3.2 (velocity-size diagram for 20 cm flow depth).

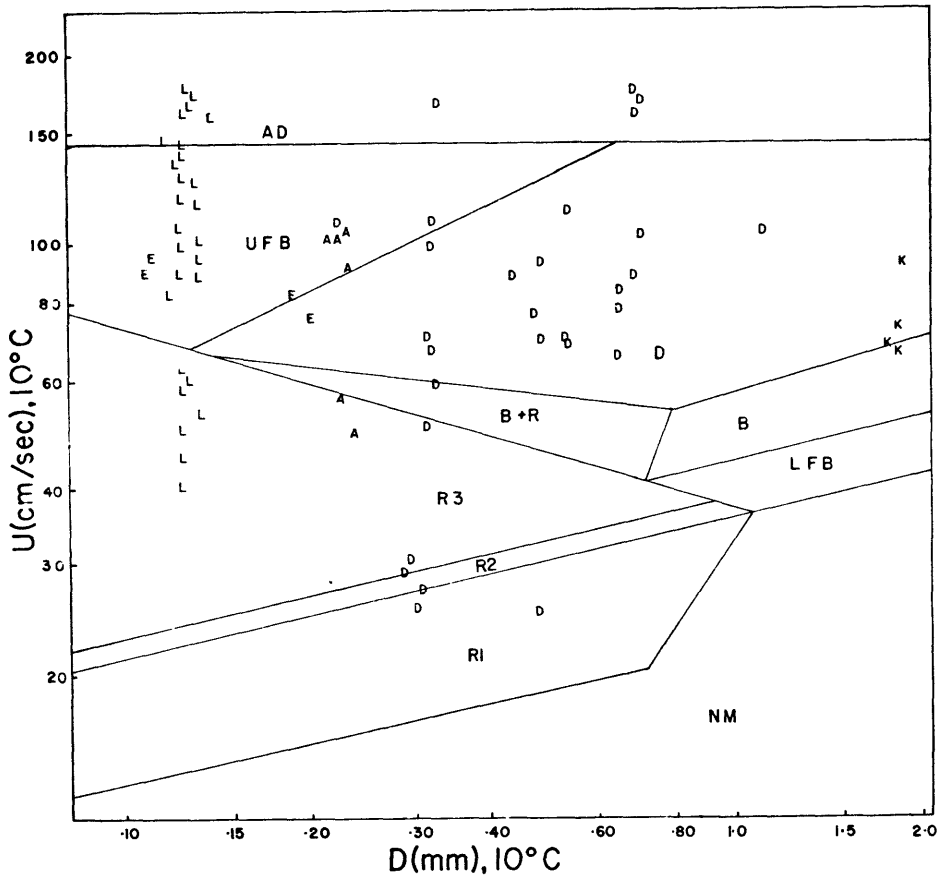

Fig. A.3. Plot by source of data for Fig. 3.3 (velocity-size diagram for 30 cm flow depth).

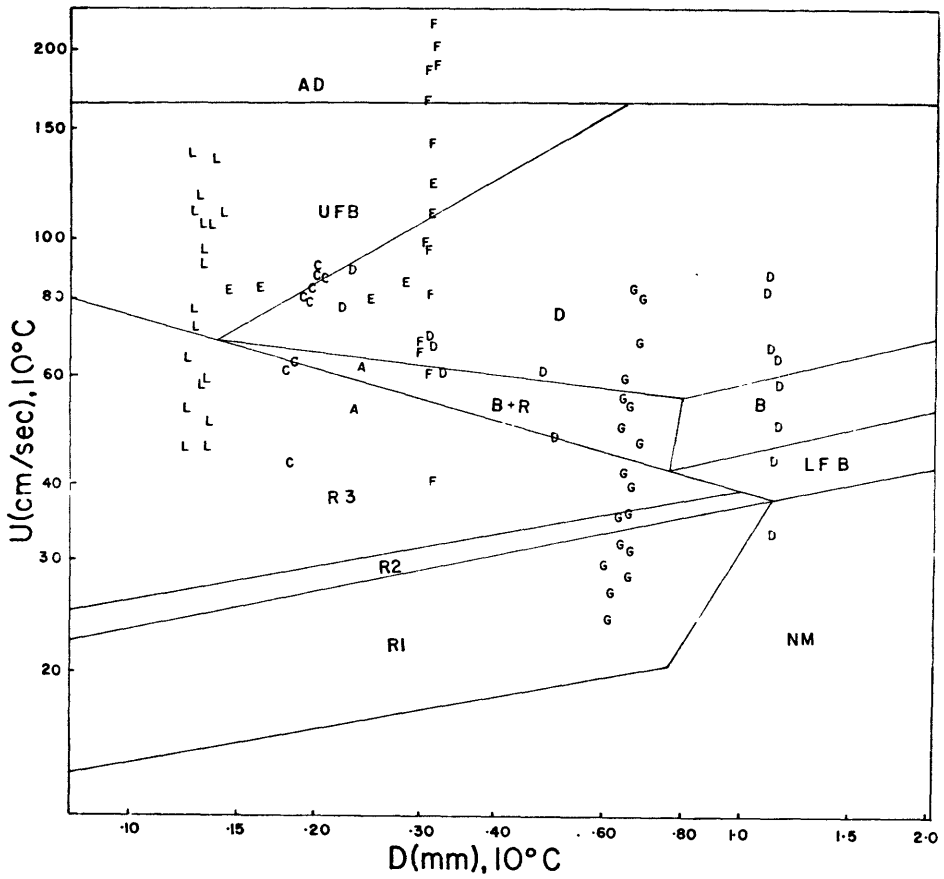

Fig. A.4. Plot by source of data for Fig. 4.4 (velocity-size diagram for 40 cm flow depth).

LEGEND

SOURCE	SYMBOL
Barton and Lin, 1955	A
Costello, 1974	B
Davies, 1971	C
Guy, Simons, and Richardson, 1966	D
Hill, Srinivason and Unny, 1969	E
Nordin, 1976	F
Pratt and Smith, 1972	G
Southard and Boguchwal, 1973	H
Vanoni and Brooks, 1957	J
Williams, 1967, 1970	K
Willis, Ellis, and Coleman, 1972	L

STABILITY FIELD	SYMBOL
No movement	NM
No movement, metastable	R1
Lower flat bed	LFB
Ripples initiated	R3
Bars plus ripples	B+R
Bars	B
Dunes	D
Upper flat bed	UFB
Antidunes	AD

Fig. A.5. Legend for Figs. A.1-A.4 (fold out for reference).

BIOGRAPHY

Lawrence Allen Boguchwal was born in Omaha, Nebraska on October 16, 1950. He received his B.A. from Harvard College in 1972 and entered M.I.T. that same year. On July 4, 1976 he married Freda Roberta Weiner.